

# **Investigation of the Feasibility of Fullerene Propellant for Ion Thrusters**

**John Steven Snyder**  
*Colorado State University*  
*Fort Collins, Colorado*

**November 1998**

**Prepared for**  
**California Institute of Technology**  
**Jet Propulsion Laboratory**  
**Contract 960197**



**National Aeronautics and  
Space Administration**



# REPORT DOCUMENTATION PAGE

Form Approved  
OMB No. 0704-0188

Public reporting burden for this collection of information is estimated to average 1 hour per response, including the time for reviewing instructions, searching existing data sources, gathering and maintaining the data needed, and completing and reviewing the collection of information. Send comments regarding this burden estimate or any other aspect of this collection of information, including suggestions for reducing this burden, to Washington Headquarters Services, Directorate for Information Operations and Reports, 1215 Jefferson Davis Highway, Suite 1204, Arlington, VA 22202-4302, and to the Office of Management and Budget, Paperwork Reduction Project (0704-0188), Washington, DC 20503.

<b>1. AGENCY USE ONLY (Leave blank)</b>	<b>2. REPORT DATE</b> November 1998	<b>3. REPORT TYPE AND DATES COVERED</b> Final Contractor Report	
<b>4. TITLE AND SUBTITLE</b> Investigation of the Feasibility of Fullerene Propellant for Ion Thrusters		<b>5. FUNDING NUMBERS</b>  Contract 960197	
<b>6. AUTHOR(S)</b> John Steven Snyder (edited and approved by Paul J. Wilbur)			
<b>7. PERFORMING ORGANIZATION NAME(S) AND ADDRESS(ES)</b> Colorado State University Fort Collins, Colorado 80523		<b>8. PERFORMING ORGANIZATION REPORT NUMBER</b>	
<b>9. SPONSORING/MONITORING AGENCY NAME(S) AND ADDRESS(ES)</b> California Institute of Technology Jet Propulsion Laboratory 4800 Oak Grove Dr. Pasadena, California 91109		<b>10. SPONSORING/MONITORING AGENCY REPORT NUMBER</b>  Contract 960197	
<b>11. SUPPLEMENTARY NOTES</b> Work Done under Contract with the California Institute of Technology, Jet Propulsion Laboratory. John R. Anderson - Contractor Monitor.			
<b>12a. DISTRIBUTION/AVAILABILITY STATEMENT</b>		<b>12b. DISTRIBUTION CODE</b>	
<b>13. ABSTRACT (Maximum 200 words)</b>  Ion thrusters operating on Buckminsterfullerene (C <sub>60</sub> ) propellant have the potential for significant efficiency improvements over current-day xenon ion thrusters. The operation of radio-frequency and direct-current thrusters on C <sub>60</sub> propellant is examined. It is demonstrated that both types of thruster give very poor performance with C <sub>60</sub> propellant. The results of discharge plasma diagnostics reveal that there are relatively large densities of negative ions in the C <sub>60</sub> plasmas caused by the large electron affinity of the C <sub>60</sub> molecule. It is shown that this relatively large negative ion density significantly limits the rate at which positive ions can be extracted from the thruster to produce thrust, thereby limiting performance. Evidence which indicates that fragmentation of the C <sub>60</sub> molecule occurs during ion thruster operation is also presented. It is shown that molecular fragmentation is caused by the impact of C <sub>60</sub> on high-temperature surfaces inside the ion thruster as well as by collisions with energetic electrons in the discharge plasma. A simple kinetic model of the fragmentation process in the discharge plasma is developed and compared to experimental data. The results indicate that fragmentation is caused by a single energetic electron impact on C <sub>60</sub> , and that fragmentation can be reduced by decreasing electron densities and energies. It is concluded that, as a result of negative ion formation and fragmentation, conventional ion thrusters operating on C <sub>60</sub> propellant will not be competitive with current-day xenon thrusters. Other types of plasma sources are evaluated for ion thrusters based on the results of this study, and the properties of an ideal plasma source for a C <sub>60</sub> ion thruster are suggested.			
<b>14. SUBJECT TERMS</b> C <sub>60</sub> , Fullerene, Ion Thruster		<b>15. NUMBER OF PAGES</b> 112	
		<b>16. PRICE CODE</b>	
<b>17. SECURITY CLASSIFICATION OF REPORT</b> Unclassified	<b>18. SECURITY CLASSIFICATION OF THIS PAGE</b> Unclassified	<b>19. SECURITY CLASSIFICATION OF ABSTRACT</b> Unclassified	<b>20. LIMITATION OF ABSTRACT</b>



## TABLE OF CONTENTS

<u>Title</u>	<u>Page</u>
I. Introduction	1
II. Experimental Apparatus and Procedures	9
III. Ion Thruster Operation and Diagnostics	19
A. Radio-Frequency Thruster	19
1. Ion Beam Extraction	20
2. Langmuir Probe Measurements	24
3. Comparison of Probe and Beam-Extraction Results	27
B. Direct-Current Thruster	30
1. Ion Beam Extraction	31
2. Langmuir Probe Measurements	32
3. Comparison of Probe and Beam-Extraction Results	35
C. The Bohm Factor	37
IV. Fragmentation of the C <sub>60</sub> Molecule	43
A. Residue Analysis and Measurement	43
B. Analysis of Extracted Ion Beams	49
C. Fragmentation Modeling	53
1. Model Development	54
2. Results and Comparison to Experiment	65
3. Comparison to <b>E×B</b> Probe Data	71

V.	Prospects and Recommendations For Future Research	76
A.	ECR Ion Source	77
B.	Helicon Ion Source	79
C.	Recommendations	80
VI.	Conclusions	82
VII.	References	84
	Appendix A. Langmuir Probe Methods	90
A.	RF Probe Design	90
B.	Analysis of Probe Data Acquired in RF Discharges	93
C.	Analysis of Probe Data Acquired in DC Discharges	95
1.	Bohm Velocity in a Plasma Containing Negative Ions and Primary Electrons	95
2.	Relationship Between Particle Densities in Bulk Plasma and at Sheath Edge	99
3.	Calculation of Ion Densities from Probe Data	101
D.	Accuracy of Probe Measurements	102
	Appendix B. Nomenclature	105

## LIST OF TABLES

<u>Table</u>	<u>Page</u>
1. Typical RF Thruster Operating Conditions.	22
2. Typical Plasma Parameters in RF Discharges.	26
3. Typical DC Thruster Operating Conditions.	32
4. Typical Plasma Parameters in DC Discharges.	34
5. Mass Accumulated on Chamber Walls.	47
A1. Uncertainties in Plasma Parameters.	104



## LIST OF FIGURES

<u>Figure</u>	<u>Page</u>
1. Theoretical Effect of Propellant Mass on Thruster Electrical Efficiency.	3
2. Positive and Negative Ionization Cross Sections for C <sub>60</sub> .	4
3. Physical Schematic for Radio-Frequency Thruster.	10
4. Electrical Schematic for Radio-Frequency Thruster.	12
5. Physical Schematic for Direct-Current Thruster.	14
6. Electrical Schematic for Direct-Current Thruster.	16
7. Beam Current Density Extracted from RF Thruster Operating on C <sub>60</sub> .	21
8. Comparison of Argon and C <sub>60</sub> Beam Currents Extracted from RF Thruster.	23
9. Langmuir Probe Traces Acquired in Argon and C <sub>60</sub> RF Plasmas.	25
10. Langmuir Probe Traces Acquired in Argon and C <sub>60</sub> DC Plasmas.	33
11. Variation of Bohm Factor with Negative Ion Concentration.	38
12. Maxwellian Rate Factors for Ionization of C <sub>60</sub> .	40
13. Comparison of Theoretical Thruster Electrical Efficiency for Xenon and C <sub>60</sub> with Different Values of $\epsilon_B$ .	42
14. C <sub>60</sub> Mass Spectrum After No-Plasma Test.	45
15. C <sub>60</sub> Mass Spectrum After Plasma Test.	46
16. $\mathbf{E} \times \mathbf{B}$ Probe Measurement from JPL Thruster - Higher Flow Rate Condition.	50
17. $\mathbf{E} \times \mathbf{B}$ Probe Measurement from JPL Thruster - Lower Flow Rate Condition.	52
18. Cooling Rates for Processes Affecting Vibrationally-Excited C <sub>60</sub> <sup>+</sup> .	61
19. Calculated Fragmentation Rate Distribution Functions for C <sub>60</sub> <sup>+</sup> .	63

19. Calculated Fragmentation Rate Distribution Functions for $C_{60}^+$ .	63
20. Comparison of Measured and Calculated Fragmentation Rates in a DC Discharge.	67
21. Variation of Calculated Fragment Ion Density Ratio with Primary Electron Energy.	70
22. Variation of Calculated Fragment Ion Density Ratio with Electron Temperature.	72
23. Comparison of Experimental $E \times B$ Probe Data and Model Calculations.	74
A1. Schematic of Langmuir Probe for Measurements in RF Plasmas.	91

## I. INTRODUCTION

An ion thruster is a device which electrostatically accelerates a beam of positively-charged ions to high velocities, thereby producing thrust. Ion thrusters can be significantly more efficient than conventional chemical rockets [1], allowing, for example, a greater payload mass for a given total spacecraft mass, or simply a lesser total mass. For a communications satellite in Earth orbit, this can translate to additional revenue or decreased launch costs, respectively. A tremendous demand for communications and scientific satellites exists and ion thrusters are becoming increasingly attractive for those missions.

One area of engineering and research interest for ion thrusters is increasing the efficiency of the devices, and one particular means of achieving this is through the choice of propellant. Desirable properties of a propellant are that it has a relatively large mass and that it is relatively easy to ionize [1]. Mercury and cesium were used in the early stages of thruster development, but for reasons including handling difficulties and toxicity these propellants were abandoned for inert gases, of which xenon is currently the most widely used. The recent discovery of Buckminsterfullerene ( $C_{60}$ ), one of a number of members of the fullerene family, has led to excitement in the thruster community about a possible new propellant [2,3].  $C_{60}$  is 5.5 times more massive than xenon and it is also easier to ionize.

Ion thruster operation with different propellants can be compared by calculating the thruster electrical efficiency, which is defined as the kinetic power of the accelerated ion beam divided by the total electrical power required to operate the thruster. The

electrical efficiency depends on the propellant mass, the energy required to produce an ion that is extracted in the ion beam ( $\epsilon_B$ ), and the specific impulse, which is determined by the spacecraft mission requirements. Thruster efficiencies were calculated [4] for argon, xenon, and  $C_{60}$  propellants and the results are shown in Fig. 1 as a function of specific impulse, assuming a typical value of beam-ion energy cost (200 eV/ion) applies to all of the propellants. The advantage of propellants with larger masses is clearly shown in the figure, and it can be seen that there is a distinct advantage to using  $C_{60}$  propellant, especially at the lower specific impulses. Potentially, efficiency improvements of 20-40% could be achieved with the use of  $C_{60}$  over xenon propellant for near-Earth missions, for example, many of which have desirable specific impulses in the range of 1000-3000 sec [2].

The energy cost of a beam ion is determined in part by the propellant ionization properties, i.e. the ionization potential and cross section.  $C_{60}$  has a lower ionization potential (7.61 eV [5]) than does xenon (12.1 eV) or argon (15.8 eV). Additionally, the positive ionization cross section for  $C_{60}$  is much larger than those for the two inert gases. It has a maximum value of  $25 \text{ \AA}^2$  [6], whereas the maxima for xenon and argon are 5.5 and  $2.9 \text{ \AA}^2$ , respectively [7]. Thus, it was expected at the onset of this study that the beam-ion energy cost could be much lower for  $C_{60}$  than for the inert gases, in which case the thruster electrical efficiency gain could be even greater than that seen in Fig. 1.

In addition to its large cross section for positive ionization, however,  $C_{60}$  has a large electron affinity (2.65 eV [8]) and thus a large cross section for negative ion formation. The two ionization cross sections are shown in Fig. 2 as a function of the ionizing electron energy. The figure shows that the negative ionization cross section [9], which is very large at electron energies less than about 10 eV, does not become less than that for positive ionization until electron energies exceed 14 eV. For this reason, large negative ion densities can be expected at the low electron temperatures that are typical of ion thruster discharge chambers.  $C_{60}$  is often termed an electronegative gas because a

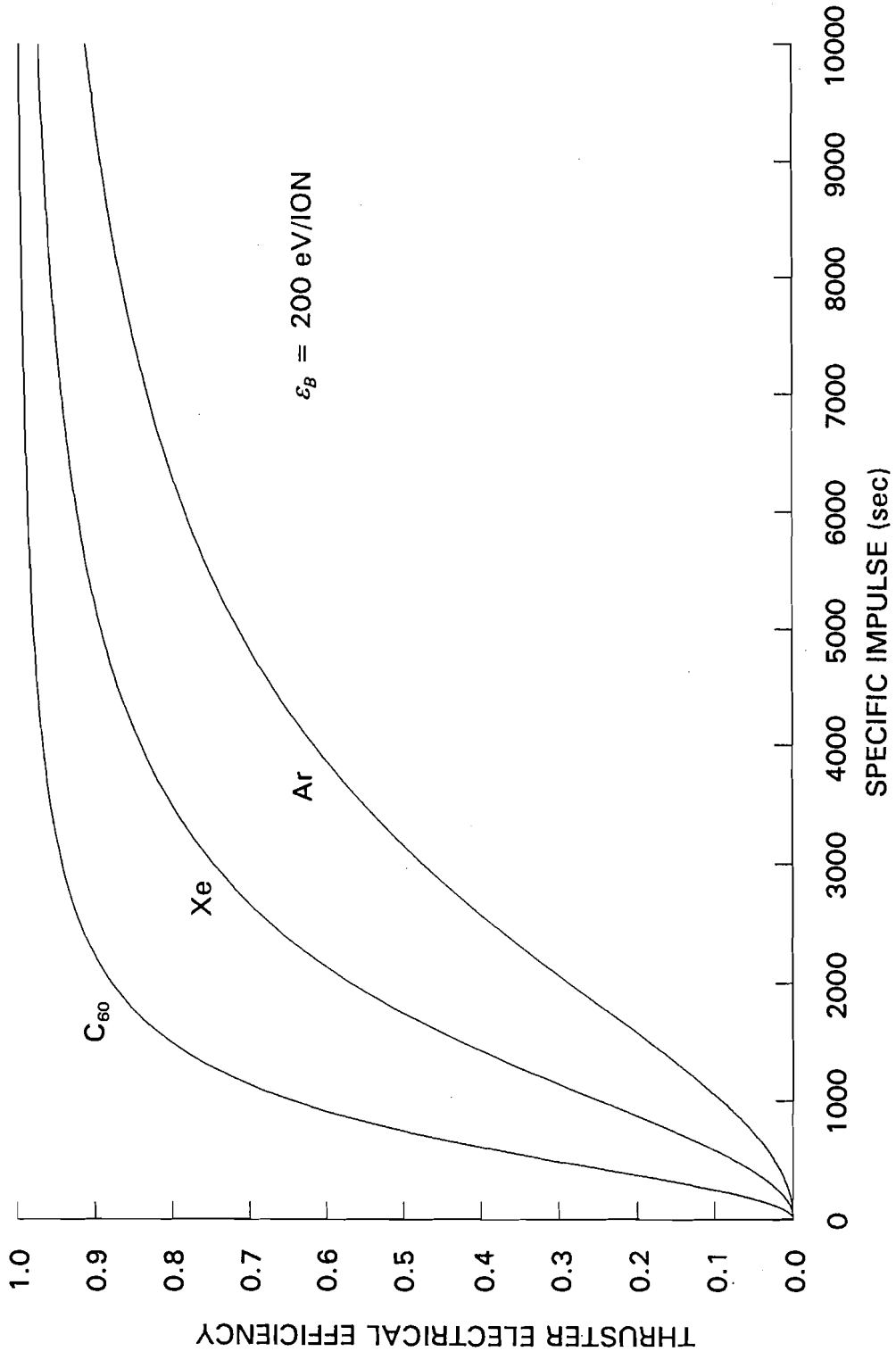


Fig. 1 Theoretical Effect of Propellant Mass on Thruster Electrical Efficiency.

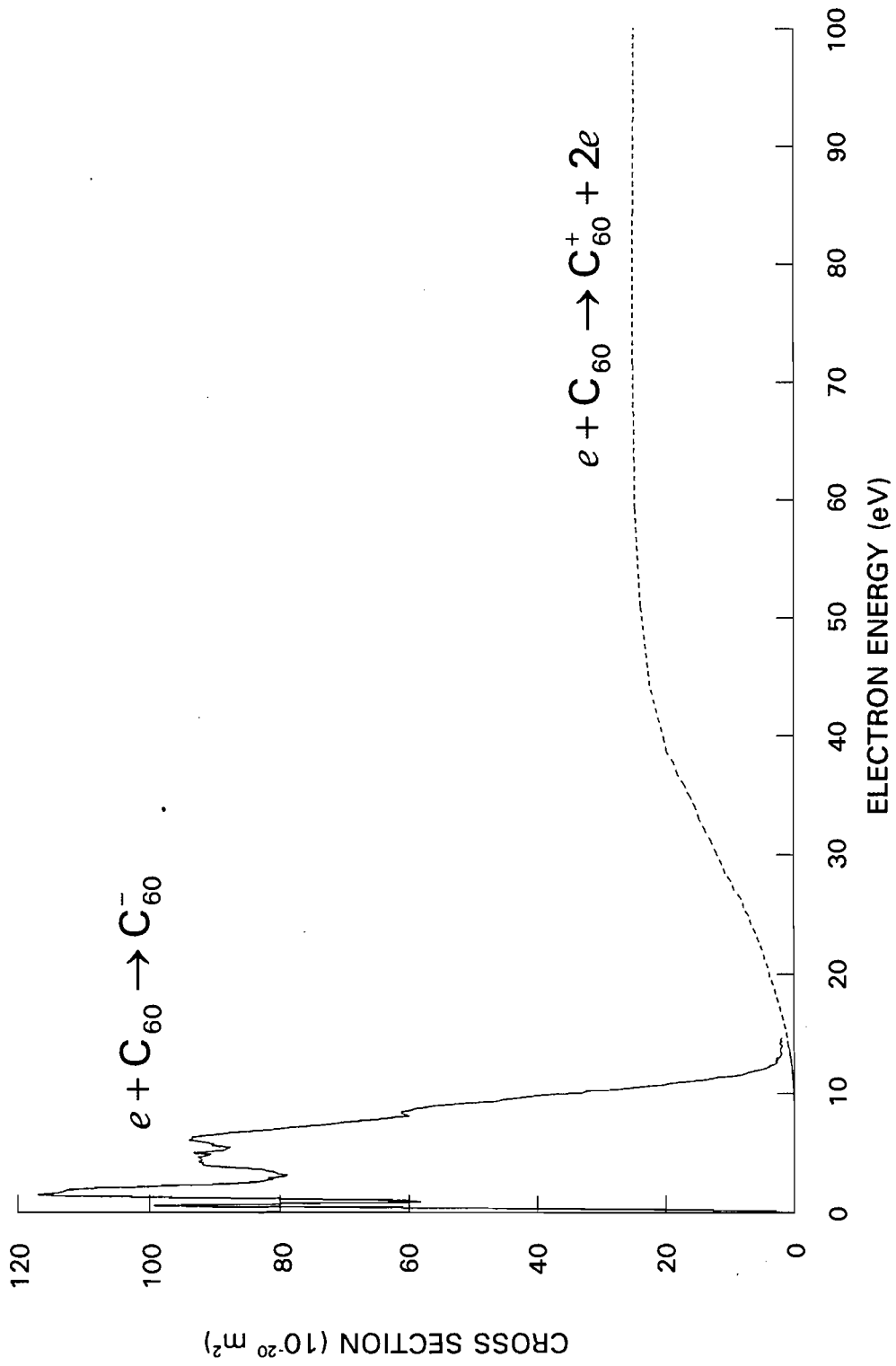


Fig. 2 Positive and Negative Ionization Cross Sections for  $\text{C}_{60}$ .

plasma discharge established with it can contain negative ions; a plasma discharge with an electropositive gas does not contain negative ions (e.g. argon or xenon plasmas).

A large negative ion density in an ion thruster could be detrimental in many ways. For example, the formation of a negative ion obviously removes an electron from the plasma discharge, and if enough electrons are removed the discharge can not be sustained in the face of positive ion losses to wall surfaces. It is also obvious that electrical energy is expended in producing negative ions without generating thrust, which reduces the thruster efficiency. A goal of this work will be to measure the negative ion density in a  $C_{60}$  ion thruster and to determine other undesirable effects of any negative ions that form.

Another potentially unattractive property of  $C_{60}$  is a tendency to fragment into smaller carbon clusters under certain conditions. For example,  $C_{60}$  will decompose into amorphous carbon on surfaces that are at temperatures greater than  $\sim 1200$  K [10] and it can fragment due to energetic processes in plasma discharges [11]. Both of these mechanisms may be important in ion thrusters. During early work on  $C_{60}$  thrusters it was assumed (or it appeared) that fragmentation induced in the plasma discharge would either be acceptably small or that it could be reduced to low values through proper selection of discharge parameters, although more recent research suggests that this may not be true. Another goal of this work will be to determine the causes of  $C_{60}$  fragmentation in ion thrusters and if fragmentation can be controlled.

Over the last several years much research has been focused on understanding the  $C_{60}$  molecular fragmentation process in the gas phase. It has become clear through basic investigations that fragmentation could occur if a molecule acquired sufficient internal energy, whereby a  $C_2$  molecule would be emitted spontaneously from  $C_{60}$  through the process of unimolecular decay [12-14]. For the positive  $C_{60}$  ion, this process is



The fragment molecules undergo the same process, as do neutral molecules and multiply-charged fullerenes.  $C_{60}$  is a kinetically stable molecule, but it is

thermodynamically unstable relative to graphite under ambient conditions. Thus, once it acquires sufficient internal energy and fragments, it will eventually decompose into small carbon groups and amorphous carbon [15].

The unimolecular decay theory that has been used to describe  $C_{60}$  fragmentation is statistical in nature, and one result of this is that the characteristic time for fragmentation depends on the amount of molecular internal energy. Several values have been suggested for the internal energy required before the onset of  $C_{60}$  fragmentation on the microsecond timescale that is typical of mass spectrometric devices, but most of the reported values are close to 40 eV [13,16,17]. Of the many mechanisms that have been studied to impart internal energy to the cluster (e.g. laser-desorption, electron impact, atom bombardment, and surface collisions), the dominant one in a thruster discharge chamber will be electron impact. Experiments with single electron impact on  $C_{60}$  molecules have shown that fragment molecules do not appear, on a microsecond timescale, until electron energies reach approximately 44 eV [18]. The unimolecular decay theory states, however, that the characteristic time for fragmentation increases as the required energy for fragmentation decreases [19]. Since the residence time of a propellant atom or molecule in a thruster discharge chamber is on the order of milliseconds, it is likely that fragmentation may be induced by electrons with energies lower than 40 eV.

Several research groups have investigated beam extraction and fragmentation with  $C_{60}$  propellant in ion thrusters. Hruby *et al.* [20] extracted up to 10 mA of beam current from a direct-current (DC) thruster with a hot-filament cathode. After thruster operation they found a carbonaceous residue covering most of the inside of the discharge chamber which appeared to be fragmented fullerenes. Nakayama and Takegahara [21] extracted 38 mA from their filament-cathode DC thruster. Measurements of the extracted beam with an  $\mathbf{E} \times \mathbf{B}$  probe showed accelerated fragments of  $C_{60}^+$ , and it was observed that as the discharge voltage was decreased from 40 to 35 V the fragmentation became less severe.

In earlier experiments [22] analysis of the “soot” from the inside of their discharge chamber showed no trace of  $C_{60}$ . Anderson *et al.* [23] attempted unsuccessfully to sustain a radio-frequency (RF) discharge on  $C_{60}$  alone. It was found that sufficient  $C_{60}$  added to a xenon RF plasma would quench the discharge, probably because of negative ion formation. Anderson and Fitzgerald [24] used an  $E \times B$  probe to determine the composition of the 8-mA beam extracted from a filament-cathode DC thruster and it was estimated that 70-80% of the singly-ionized particles in the beam were fragmented fullerenes. Additionally, chemical analysis of the considerable residue collected from the discharge chamber revealed no fullerenes.

Ion sources operating on  $C_{60}$  have also been used for non-propulsive applications. Gruen *et al.* [11] operated an argon microwave discharge seeded with  $C_{60}$  to grow carbon films. Spectroscopic analysis showed a large concentration of  $C_2$  in the discharge, indicating extensive fragmentation of  $C_{60}$ . Maiken and Taborek [25] used a filament-cathode DC ion source to extract up to 0.1 mA of beam current and they reported fragmentation in the beam and in residue collected from the inside of the chamber. It was also shown that an increase in the discharge current, with all else held constant, increased the fragmentation in the beam. Finally, Horak and Gibson [26] extracted up to 7 mA while investigating fragmentation in the beam. They reported very little fragmentation at discharge voltages less than 40 V, although fragmentation in the chamber was indicated by an accumulation of residue.

The results of these studies indicate that fragmentation will be an issue for  $C_{60}$  ion thrusters, although it may be controlled by proper selection of operating conditions (e.g. discharge voltage and current). Fragmentation is undesirable because it decreases the efficiency of the thruster [27], increases the difficulty of producing a desired thrust level (because of the unknown and variable composition of the extracted beam), and because carbon residue can build up on discharge chamber surfaces where it can induce a short-

circuit between components such as the screen and accelerator grids which must be maintained at different potentials.

In addition to the fragmentation problem, these studies indicate that much work has yet to be done to produce an efficient  $C_{60}$  thruster. The beam current densities in all of these studies [20-26] except one ranged from 0.04 to 0.25 mA/cm<sup>2</sup>, with Nakayama and Takegahara achieving 0.76 mA/cm<sup>2</sup> [21], whereas efficient noble gas thrusters operate in the range of a few to several mA/cm<sup>2</sup> [28]. In the  $C_{60}$  thruster research the propellant utilization efficiency, which is defined as the fraction of the propellant inflow that is extracted as an ion beam, was low in each case (4-50%) and the beam-ion energy costs were high (~1300-3500 eV/ion). Efficient thrusters operate near 80-90% and a few hundred eV/ion, respectively. More recent experiments were performed by Nakayama *et al.* [29] in which electromagnets were used to in an attempt increase the thruster efficiency, but the beam-ion energy costs were still very large. Recall that  $C_{60}$  is attractive as a propellant because it should be *easier* to ionize and thus have a *lower* beam-ion energy cost. It was unclear whether these thruster inefficiencies were due to thruster design and operating conditions, or characteristics inherent to  $C_{60}$  as a propellant.

The purpose of this study was to investigate ion thruster operation on  $C_{60}$  propellant, including possible fragmentation phenomena, in order to determine the feasibility of  $C_{60}$  as an ion thruster propellant. Both radio-frequency and direct-current thrusters were constructed and tested as illustrated in Chapter II. Chapter III describes the beam-extraction results and factors affecting the thruster efficiency. Fragmentation studies and modeling of the fragmentation process are presented in Chapter IV. Finally, the results obtained in this study are applied to other ion sources which may be used for ion thrusters in Chapter V, and the major conclusions of this work are summarized in Chapter VI.

## II. EXPERIMENTAL APPARATUS AND PROCEDURES

Experiments were conducted in a 44-cm dia. bell-jar vacuum facility, a portion of which is shown in Fig. 3 along with an RF thruster test assembly. This assembly includes a cylindrical quartz discharge chamber that is closed on the upstream end and has a 20-mm dia. hole in the side wall to accommodate a quartz vaporizer. The inner tube of the vaporizer serves as an argon feed and the outer tube forms a crucible in which solid  $C_{60}$  is placed. Resistive heaters and radiation shielding surround the vaporizer and the discharge chamber, and thermocouples were used to monitor their temperatures. The chamber walls were heated to  $\sim 800$  K to prevent condensation of  $C_{60}$ . The chamber rests on a stainless-steel plate to which the thruster grids are attached. The beam diameter was limited to 35 mm so that the discharge chamber pressure could be kept high and also to accommodate feedthroughs that carried electrical power through the stainless-steel plate to terminals inside the discharge chamber. The 189-hole grid set has a screen grid hole diameter and transparency of 2.1 mm and 0.63, respectively, and an accelerator grid hole diameter and transparency of 1.9 mm and 0.50, respectively. For some experiments, a 0.38-mm dia. tantalum filament placed in the discharge chamber served as an electron source. The thruster is suspended from the top flange of the vacuum facility with three support rods (not shown) and surrounded with a ground screen which has the two-fold purpose of preventing electron backstreaming and containing RF energy.

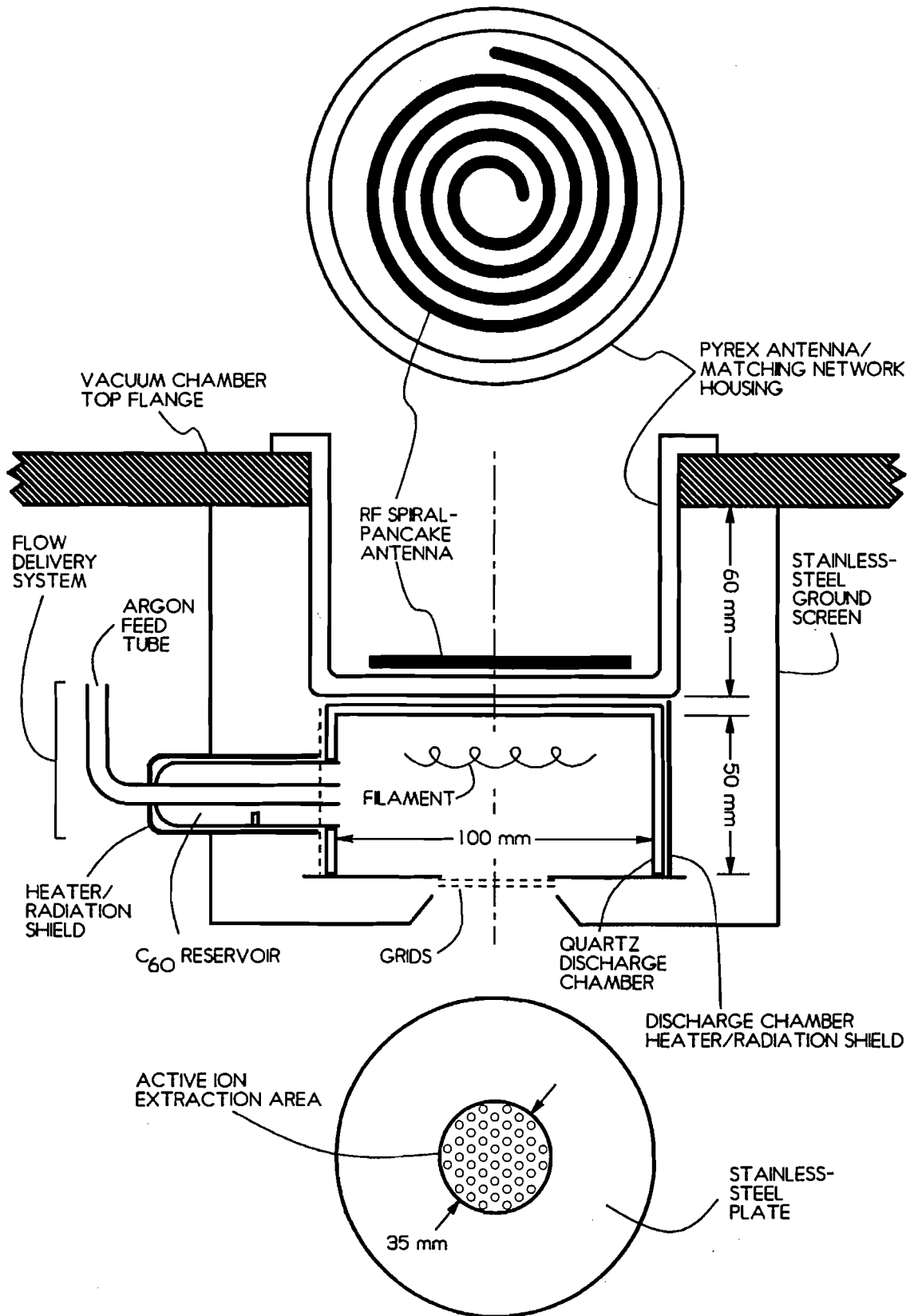


Fig. 3 Physical Schematic for Radio-Frequency Thruster.

Radio-frequency power is supplied to the thruster by means of an antenna which was formed from 6-mm dia. silver-coated copper tubing, coiled into a flat, pancake-like spiral. The antenna is in a plane orthogonal to the axis of the thruster 10 mm from the upstream surface of the discharge chamber and is housed in an inverted pyrex "hat" that forms the vacuum boundary. Both ends of the spiral antenna are connected to an electrical matching network which serves to minimize the reflected power via proper tuning of a high-voltage variable capacitor. Additionally, the antenna and portions of the matching network are water cooled. Radio-frequency power is supplied at a frequency of 13.56 MHz and typical levels of 0-300 W. Although the power supply was regulated to deliver a set RF power to the antenna, the actual power delivered to the plasma is unknown due to matching network losses and coupling between the antenna and the electrically-conductive surfaces that surround it.

The thruster electrical schematic is shown in Fig. 4, where the squares represent power supplies and the circles represent electrical meters. The screen grid is physically attached to the stainless-steel plate and is biased to a high positive potential (several hundred to a thousand volts) with respect to ground by the screen grid power supply. The accelerator (accel) grid is biased to a high negative potential (a few hundred volts) with respect to ground by the accel grid power supply. The beam and impingement currents are monitored with the meters indicated in the figure. For experiments in which a discharge chamber filament is used as an electron source, the filament is heated to thermionic emission temperatures by passing an AC current through it, while the DC current that flows between the filament and the plate is monitored with a meter. A separate hot-filament electron source is used to neutralize the ion beam extracted from the

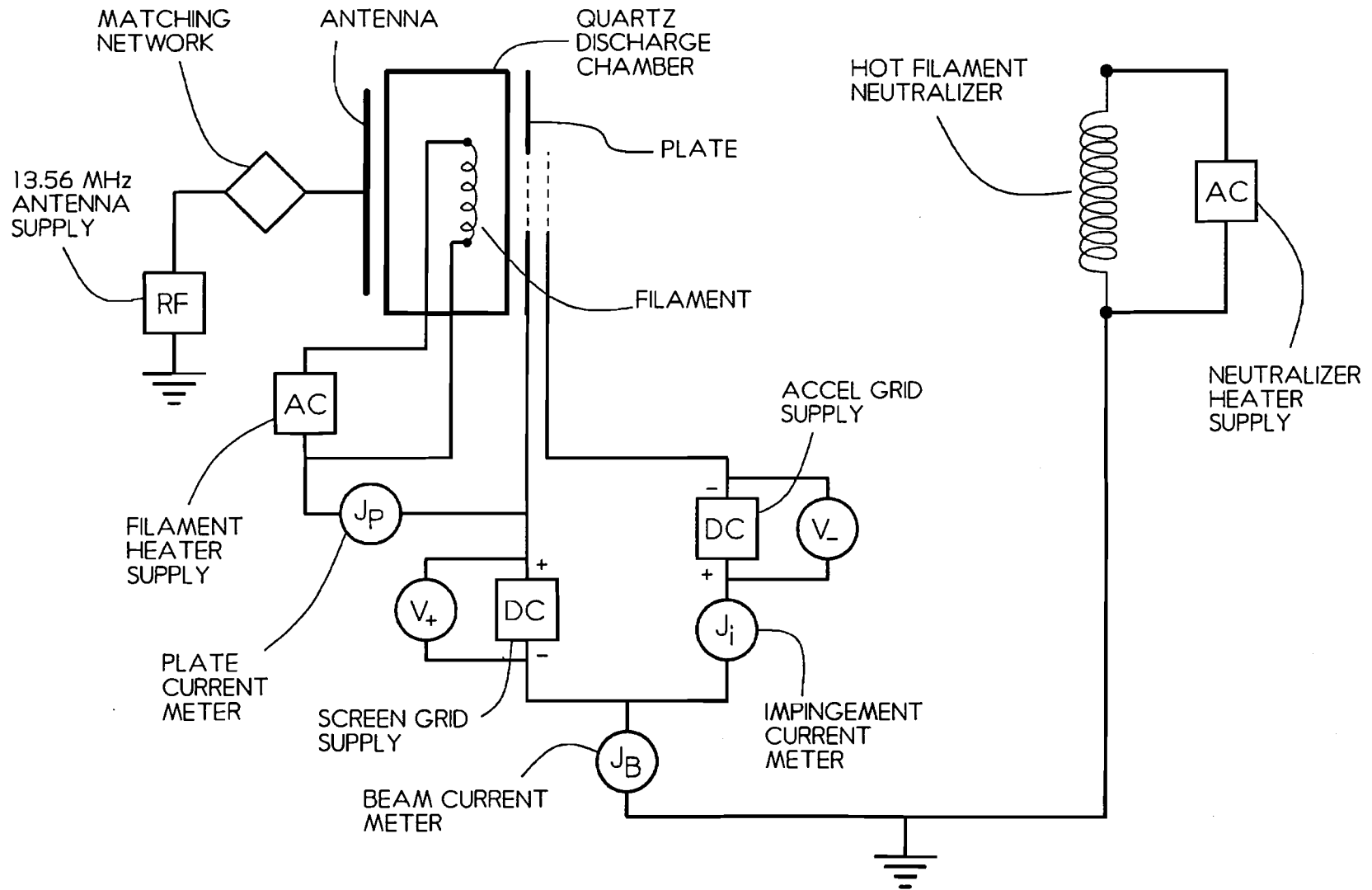
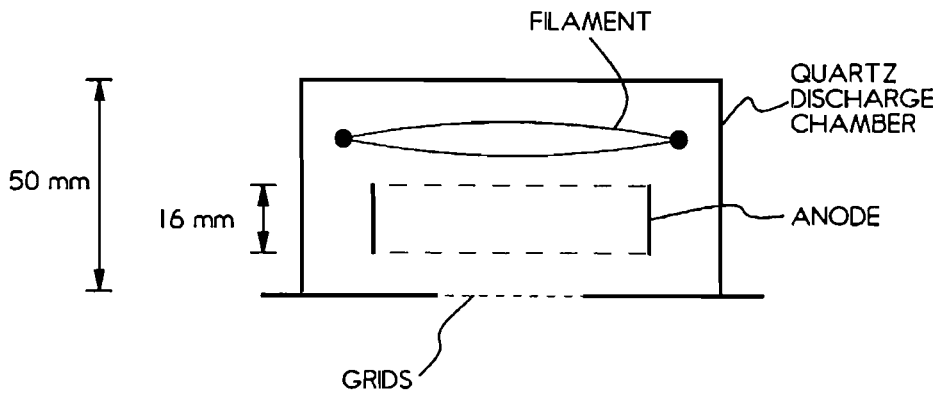


Fig. 4 Electrical Schematic for Radio-Frequency Thruster.

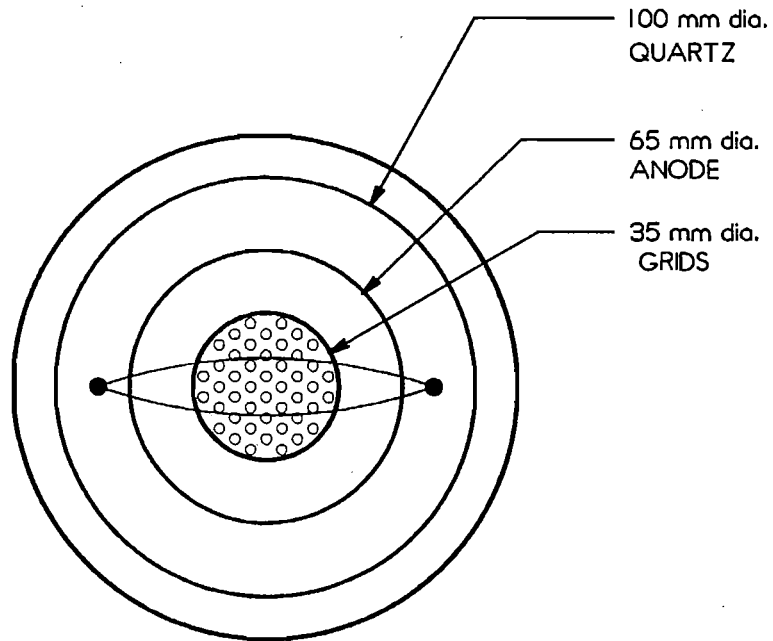
thruster. As indicated in the figure, the RF power circuit operates independently of the DC beam-extraction circuit.

Argon and  $C_{60}$  can be supplied to the discharge chamber in any mixture ratio with the argon flow monitored using a conventional thermal flow meter. When the vaporizer is heated to  $\sim 700$  K the solid  $C_{60}$  will begin to sublime and its flow rate is monitored with an Inficon XTM/2 quartz crystal microbalance (QCM) using the following method. A fraction of the sublimed  $C_{60}$  flows through a small hole in the rear of the vaporizer assembly and condenses on the QCM which is located outside of the ground screen 2 cm from the vaporizer hole. A time history of the flow rate measured by the QCM is logged on a strip-chart recorder. Next, the total  $C_{60}$  mass sublimated from the vaporizer is determined by weighing the vaporizer before and after each experiment, and the total mass deposited on the QCM is read directly from the QCM controller. A flow calibration constant is then defined as the mass sublimated from the vaporizer divided by the mass accumulated on the QCM. The flow rate to the discharge chamber is assumed to be proportional to the QCM flow rate and is determined by multiplying the flow calibration constant by the indicated QCM flow rate. The mass flow to the QCM from the vaporizer was a negligible fraction of the flow to the discharge chamber.

Experiments were also performed with a DC source. The general experimental schematic in Fig. 3 was unchanged except the RF antenna was removed and an anode and cathode were added to the discharge chamber. The discharge chamber configuration for the DC tests is shown in Fig. 5. Two 0.38-mm dia. tantalum filaments serve as the cathode and the anode is fashioned from 0.25-mm-thick stainless steel; both are physically supported from the plate by electrically insulating standoffs (not shown). The electrical



SIDE VIEW



TOP VIEW

Fig. 5 Physical Schematic for Direct-Current Thruster.

schematic for the DC thruster is shown in Fig. 6. One end of the filament cathode is held at the screen grid potential while the anode is biased positive of this potential with the discharge power supply. The discharge voltage and current can be varied independently by changing the discharge power supply voltage and filament heater current, respectively.

A variety of diagnostic methods were employed to characterize the RF and DC thruster operation on argon and C<sub>60</sub> propellant. A 1-cm dia. Faraday probe was used to measure the current density in the ion beam extracted from the thruster. The probe was biased several volts negative of ground potential in order to reflect electrons from the sensing surface, and it was swept through the beam while the positive ion current collected by the probe was logged on an X-Y recorder. Integration of the current density profile yields the total beam current extracted from the thruster, and this value was within 10% of the value given by the beam current meter when operating the thruster on argon propellant. It was found that during experiments with C<sub>60</sub> beam extraction, carbonaceous material would build up on electrical insulators in the thruster and significant leakage currents could develop between the screen grid and ground-potential surfaces. Because of this, reliable measurements of beam current could not be obtained from meters in the electrical circuit, and the C<sub>60</sub> beam currents were obtained instead by integrating the Faraday probe traces. It was observed, however, that in the first stages of an experiment before leakage currents developed, the beam current indicated by the meter would agree to within several percent of that obtained by integrating the Faraday probe trace. Although carbon buildup on Faraday probe surfaces was possible during the ~5-10 minute typical duration of an experiment, it is believed that this did not affect the probe measurements seriously.

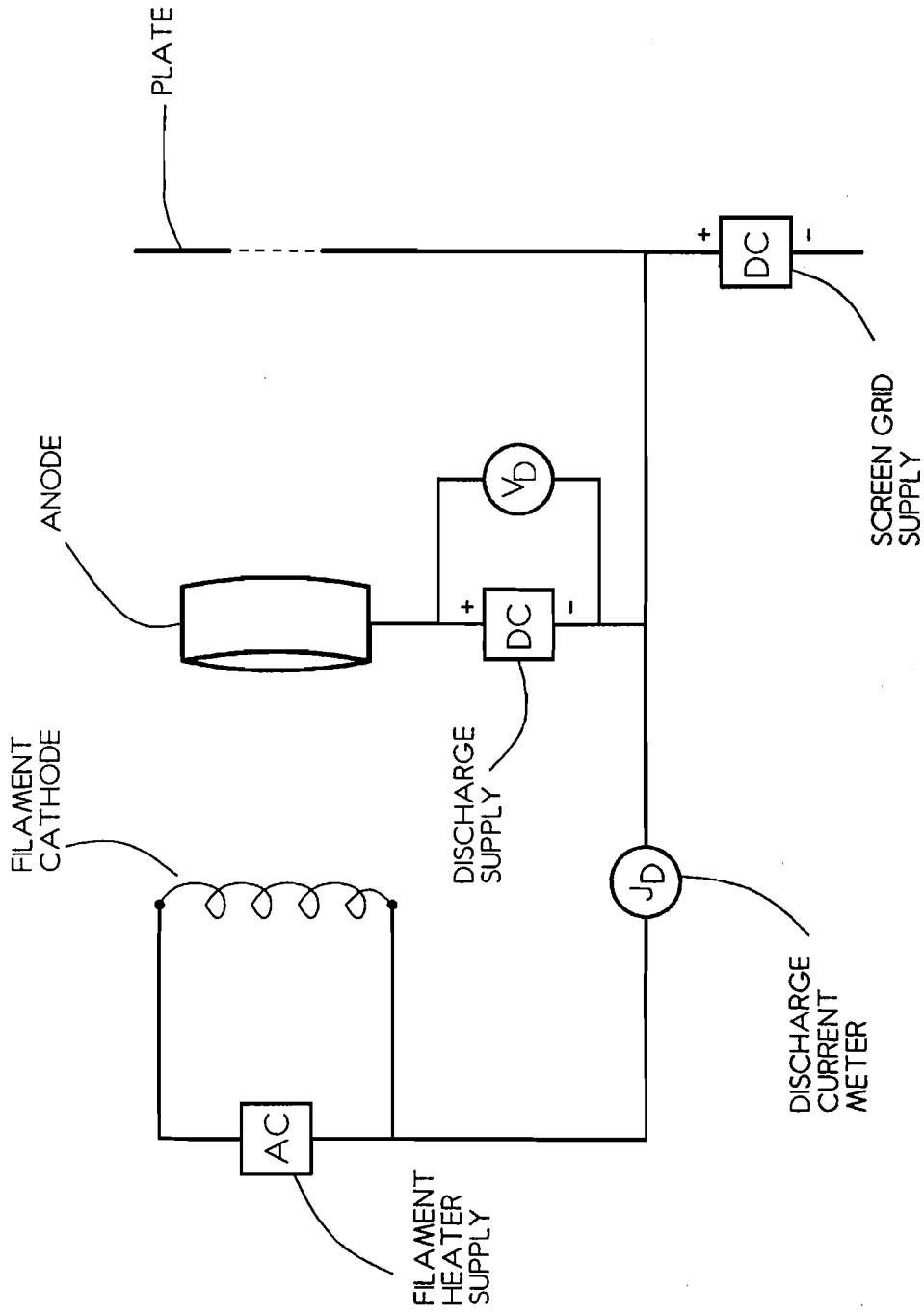


Fig. 6 Electrical Schematic for Direct-Current Thruster.

Additionally, Langmuir probes were used to characterize the argon and  $C_{60}$  plasmas that were produced in the RF and DC discharges. A variety of different probe sizes and shapes were used to ensure accurate measurements and facilitate analysis of the probe data. The probe used in the DC plasmas was a standard 3.2-mm dia. stainless-steel sphere supported by a quartz tube holder [30]. The probe used for measurements in RF plasmas was specially designed to minimize the effect of RF plasma fluctuations on the probe response. The probe collection surface was a 5-mm long tungsten wire, 0.075-mm dia. for argon plasmas and 0.254-mm dia. for  $C_{60}$  plasmas. Analysis of the Langmuir probe data was complicated by the presence of primary electrons in the DC thruster, and by negative  $C_{60}$  ions in both RF and DC thrusters. A complete description of the RF Langmuir probe design and the analysis methods for all probe data can be found in Appendix A. For the probe measurements the grids were replaced with a plate with a similar open area, but with larger holes to admit the probes. Measurements were not made while ion beams were being extracted.

Fragmentation diagnostics were performed on the carbonaceous residue that was found on the inside surfaces of the discharge chamber after many of the individual  $C_{60}$  experiments. Since  $C_{60}$  is soluble in toluene but amorphous carbon is not [31], a simple solubility test can be performed on the residue to determine if it is pure  $C_{60}$  or carbon resulting from  $C_{60}$  fragmentation. Residue samples were also analyzed with mass spectrometry to determine their composition. The solid samples were collected and sent to a mass spectrometry facility where they were vaporized, ionized by 70-eV electron impact, and subsequently mass analyzed. The results are given as the number of ions counted as a function of mass-to-charge ratio.

The extent of fragmentation in the thruster was quantified by determining the mass of fragmented carbon that condensed on the quartz discharge chamber walls. This was done by weighing the chamber before and after each experiment. Although not all fragmented molecules are accounted for with this method, it is believed to be representative of the total amount of fragmentation occurring in the chamber. It is also noted that not necessarily all of the condensed mass was from fragmented C<sub>60</sub>. Some molecular C<sub>60</sub> could condense on relatively cool surfaces of the discharge chamber that were not directly heated such as the grids and also on the upstream surface of the chamber adjacent to the water-cooled antenna.

### III. ION THRUSTER OPERATION AND DIAGNOSTICS

#### A. Radio-Frequency Thruster

The first attempts to operate the RF thruster on  $C_{60}$  propellant were performed by introducing a  $C_{60}$  flow into the thruster when it was operating on argon and then slowly decreasing the argon flow. In all of the tests that were conducted in this fashion, however, there was no observable plasma discharge and no measurable beam current after the argon flow rate had been reduced to zero. It was reasoned that this was likely due to the electronegative properties of  $C_{60}$ , i.e. since  $C_{60}$  is an efficient electron scavenger at low electron energies, the free electron population was depleted to the point where a plasma discharge could not be sustained. This scavenging argument is supported by the observation that small concentrations of electronegative gases are intentionally added to plasmas in order to cause large reductions in electron density [32].

In order to counteract the electron depletion through negative ion formation, an electron source was added to the discharge chamber. Although the main attractive feature of the RF over the DC thruster is the elimination of a hot electron source upon which  $C_{60}$  would degrade, a hot-filament electron source was installed so that RF ion thruster operation on pure  $C_{60}$  could be achieved, the resulting discharge could be studied, and its operation could be characterized.  $C_{60}$  plasmas do not produce visible luminosity, so the presence of a  $C_{60}$  plasma was inferred by a DC current flowing between the filament and

downstream plate. With the addition of the hot filament to the discharge chamber it became possible to sustain a discharge and extract a beam from the thruster supplied with  $C_{60}$  propellant only.

### 1. Ion Beam Extraction

The initial experiments with  $C_{60}$  beam extraction were less than promising. Beam currents of only 50-200  $\mu\text{A}$  were measured with a propellant flow rate ( $\dot{m}$ ) of 20-30 mA eq. Under these conditions the propellant utilization efficiency was less than 1%. It was found that by placing the filament closer to the upstream end of the chamber substantial increases in beam current were achieved. This is because the electric fields radiated from the antenna are stronger near the antenna, and the electrons emitted from the filament are accelerated to the higher energies at which positive ion formation is more probable. A typical Faraday probe trace acquired during thruster operation is shown in Fig. 7 for the experimental conditions indicated. Integration of the trace yields a beam current of 1.2 mA. Beam currents as large as 1.5 mA and propellant utilizations of up to 3% were achieved with the RF thruster in this configuration.

During the experiments with  $C_{60}$ , a direct correlation was observed between the beam current and the filament heater current. If a discharge was obtained and the heater current was turned off (i.e. no electrons were being emitted), the discharge would extinguish and no beam current would be measured. Increasing the heater current would cause the discharge to re-ignite and a beam current would be measured. Thus, it is apparent that, at the RF powers and  $C_{60}$  flow rates investigated in this study (0-300 W and 0-100 mA eq., respectively), a continuous electron source is required to sustain a  $C_{60}$  plasma using an inductive RF power supply.

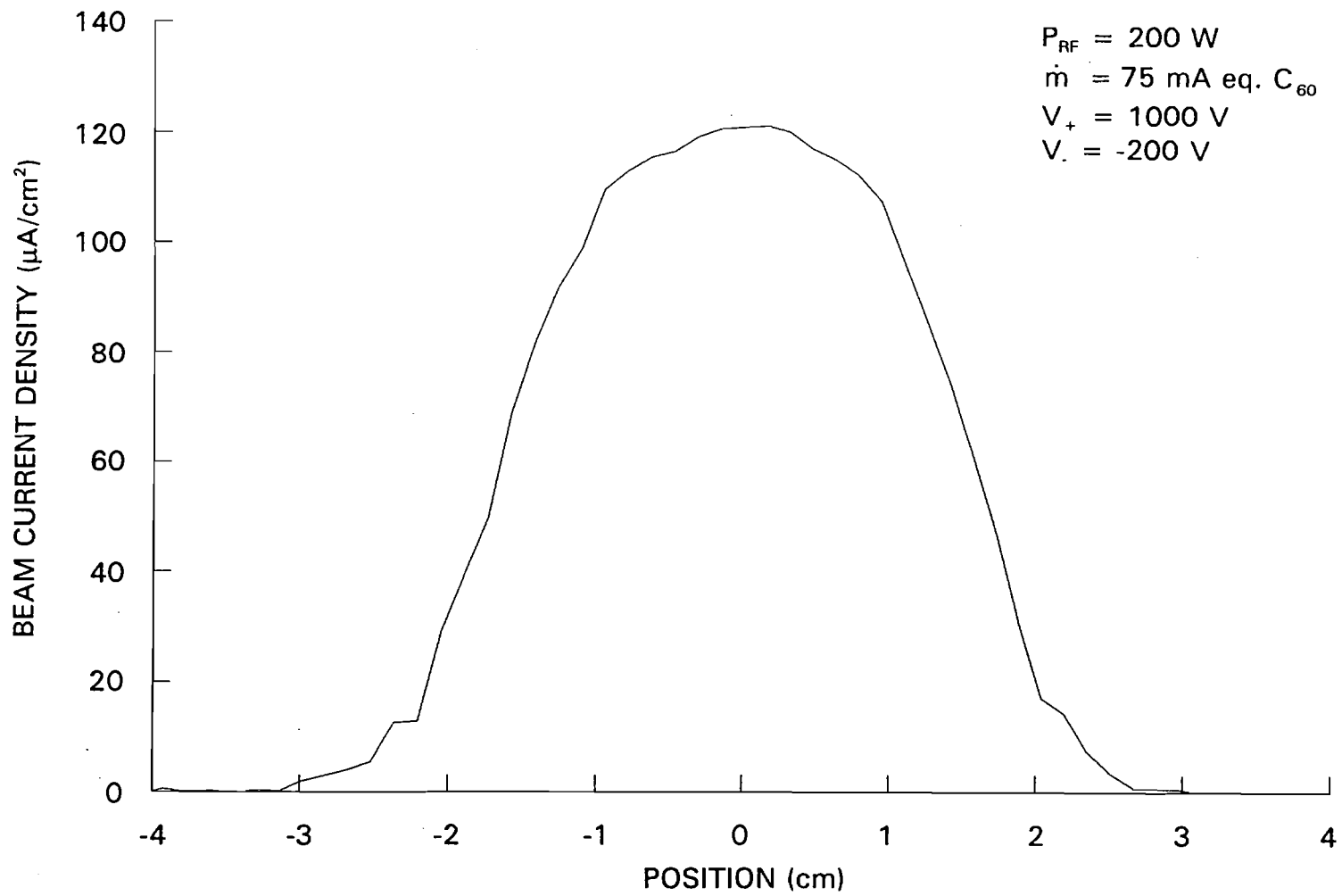


Fig. 7 Beam Current Density Extracted from RF Thruster Operating on  $C_{60}$ .

Ion beam extraction from the thruster was next examined and compared for  $C_{60}$  and argon propellants under the range of operating conditions indicated in Table 1. Beam current as a function of RF power is shown in Fig. 8 for argon and  $C_{60}$  under similar operating conditions. The actual values for argon have been scaled by a factor of 0.03 to facilitate comparison with  $C_{60}$  on the same figure. The maximum  $C_{60}$  beam current that was extracted was 1.5 mA, far lower than that measured with argon propellant (32 mA). It is not immediately clear why the  $C_{60}$  beam current should be so low, although it could be due to a space-charge (i.e. perveance) limit. The normalized perveance per hole [33] associated with the 1.5-mA beam extraction is  $9.1 \times 10^{-11} \text{ A/V}^{1.5}$ , whereas the theoretical maximum is  $1.6 \times 10^{-9} \text{ A/V}^{1.5}$ , so it is clear that the beam extraction was not perveance limited.

Table 1. Typical RF Thruster Operating Conditions.

	Argon	$C_{60}$
$\dot{m}$	80-210 mA eq.	20-100 mA eq.
$P_{RF}$	80-260 W	140-260 W
$V_+, V_-$	+500-1000 V, -300 V	+500-1000 V, -200 V
$J_B$	15-60 mA	0.1-1.5 mA

It is also useful to compare the performance of the thruster with the two different propellants. The beam-ion energy cost for the  $C_{60}$  data in Fig. 8 is very high, about 170,000 eV/ion at an RF power of 260 W. The beam-ion energy cost for the argon thruster at 260 W is 8200 eV/ion, which is large compared to conventional DC noble gas thrusters ( $\sim 200$  eV/ion [28]). The propellant utilization for  $C_{60}$  is 1-2% and for argon is  $\sim 25\%$ , whereas efficient thrusters operate in the range of 80-90% [28]. These poor

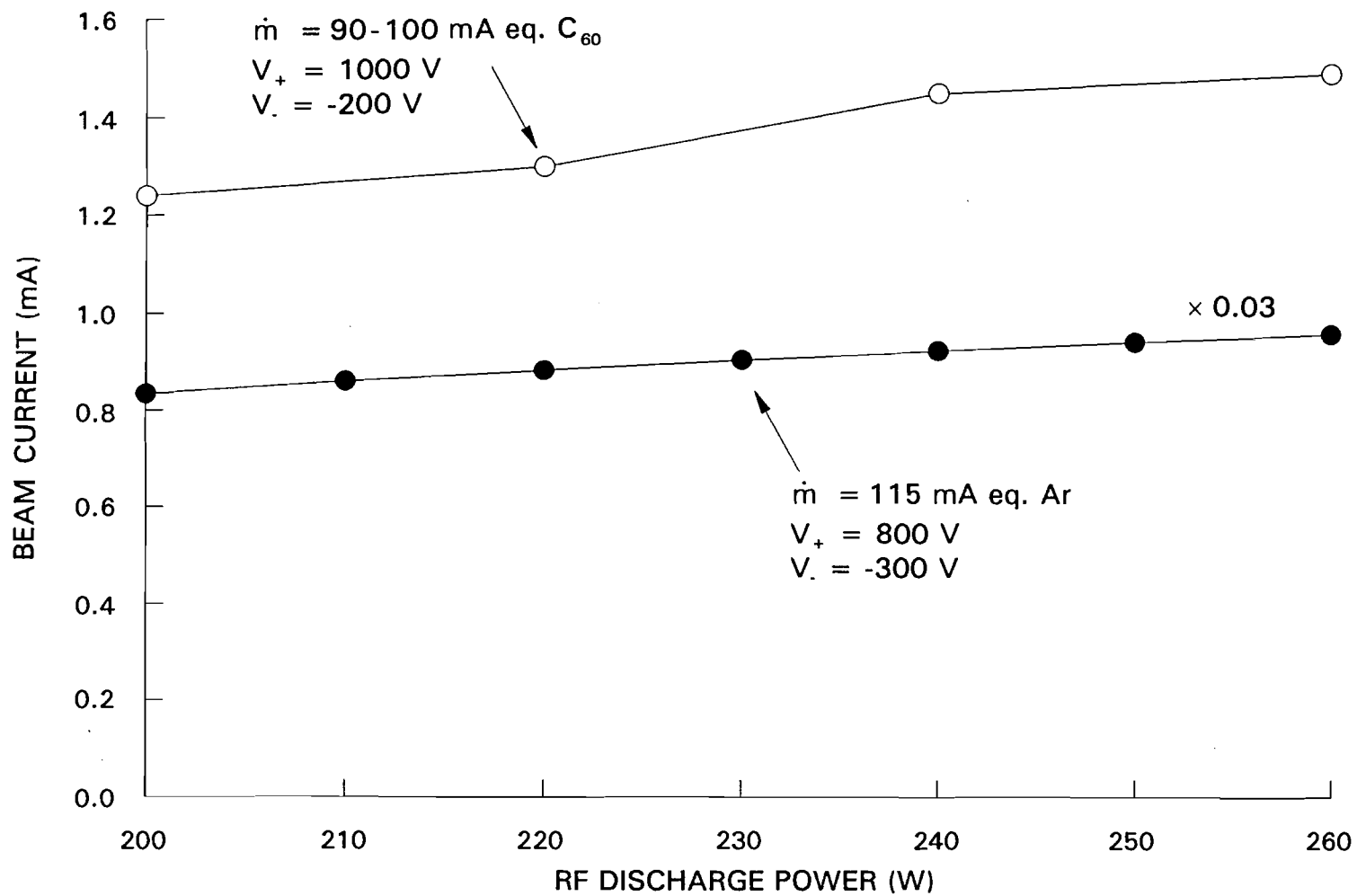


Fig. 8 Comparison of Argon and C<sub>60</sub> Beam Currents Extracted from RF Thruster.

utilizations are expected primarily because of the lack of magnetic confinement and the small ratio of grid open area to total interior surface area, which was 0.02. For argon, a baseline plasma-ion energy cost in the RF thruster of 145 eV/ion was estimated using the thruster geometry and performance curve, and this is only moderately higher than the value for efficient DC thrusters [4]. It appears, then, that the RF ionization source performs reasonably well but the total thruster performance is limited by large ion losses to wall surfaces. Although these arguments provide reasoning for the poor performance of the RF thruster with argon propellant, they do not account for the even poorer performance with  $C_{60}$  propellant. Thus, Langmuir probe measurements were made in the discharge chamber in order to characterize the discharge plasmas and to understand the reason for the difference in the extracted beam currents for the two propellants.

## 2. Langmuir Probe Measurements

Probe measurements were made in argon and  $C_{60}$  discharges under a variety of flow rate and RF power conditions. In order to minimize carbon accumulation on the probe surface during  $C_{60}$  tests, the probe was kept outside of the discharge chamber until a steady  $C_{60}$  discharge had been established; it was then moved quickly into the plasma to acquire data. Semi-log plots of the voltage-current traces acquired in argon and  $C_{60}$  discharges indicated that the electron energy distribution functions in the bulk of the plasmas were Maxwellian or near-Maxwellian in nature.

Typical probe traces acquired in the bulk of argon and  $C_{60}$  plasmas are shown in Fig. 9 for the discharge conditions indicated, where the data have been plotted as current density ( $\text{mA}/\text{mm}^2$ ) vs. voltage because of the different probe collection areas used in each experiment. In addition, the argon data have been scaled by a factor of  $3 \times 10^{-3}$  to facilitate

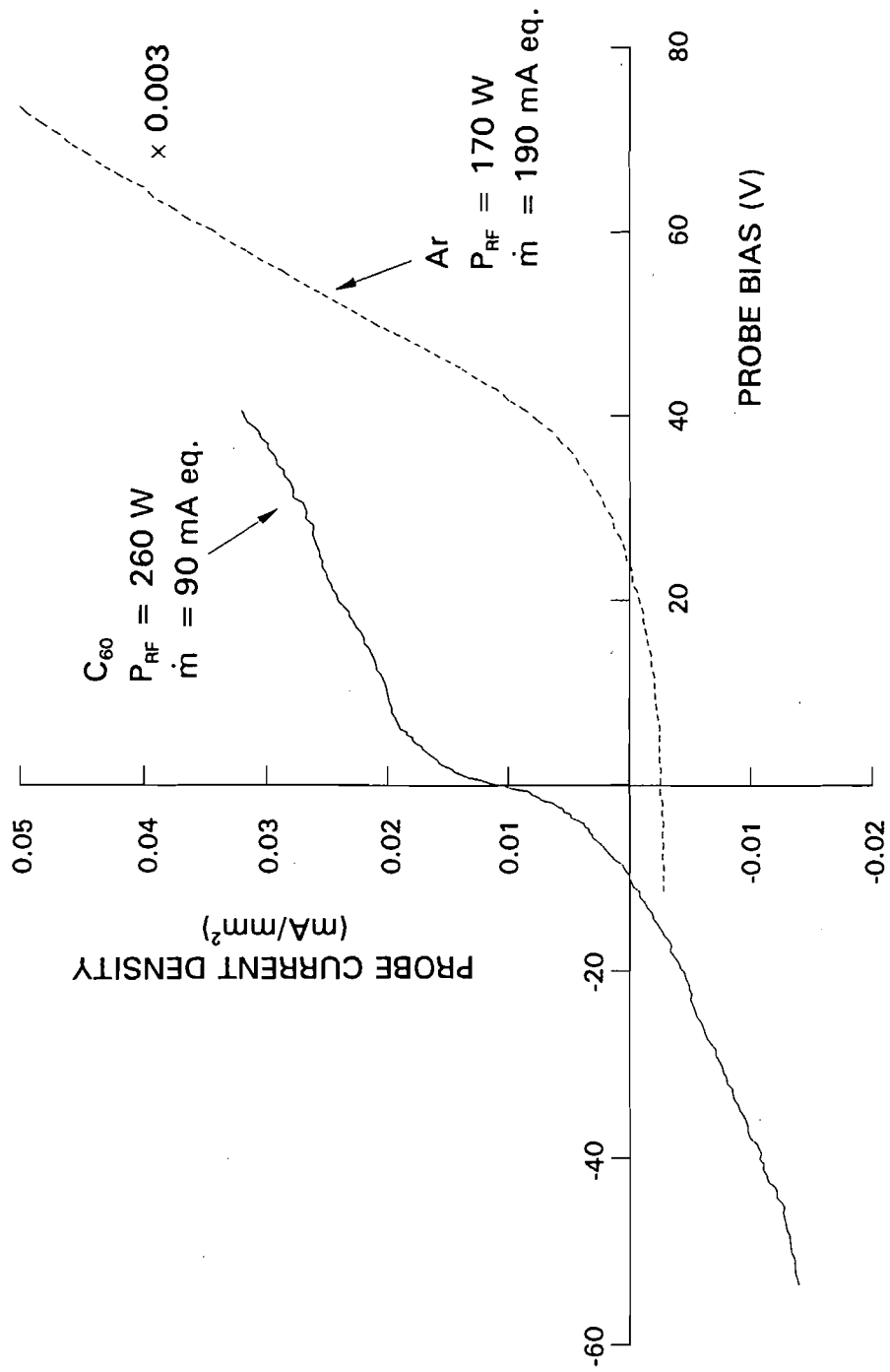


Fig. 9 Langmuir Probe Traces Acquired in Argon and C<sub>60</sub> RF Plasmas.

the comparison (i.e. at a probe bias of +75 V the current density to the probe was 17 mA/mm<sup>2</sup>). Inspection of the probe data shows that the plasma potentials were about 53 V for the argon plasma and about 1 V for the C<sub>60</sub> plasma. It is immediately apparent from the data in the figure that much more current is collected in the argon discharge than in the C<sub>60</sub> discharge at the respective plasma potentials, where the majority of the current is due to negatively-charged particles. Additionally, the relative magnitudes of the currents collected at plasma potential and at negative probe biases, where the current is mostly due to positive ions, are very different. The argon trace shows the typical behavior expected in noble-gas plasmas, i.e. relatively small current at negative probe potentials and relatively large current at the plasma potential. The C<sub>60</sub> trace, however, shows similar magnitudes of current at plasma potential and at negative probe potentials, a behavior that is manifested in plasmas with significant populations of negative ions [34].

The argon probe trace in Fig. 9 was analyzed using standard Langmuir probe techniques and the results of the analysis are shown in Table 2. The electron temperature and density were observed to vary from roughly 10-14 eV and  $5-12 \times 10^{10} \text{ cm}^{-3}$ , respectively, as a function of position in the discharge chamber under the same operating conditions. Appropriate verification of the rather high electron temperature was

Table 2. Typical Plasma Parameters in RF Discharges.

	Argon	C <sub>60</sub>
$T_e$	12 eV	4 eV
$n_{eo}$	$10 \times 10^{10} \text{ cm}^{-3}$	$3 \times 10^8 \text{ cm}^{-3}$
$n_{+o}$	$10 \times 10^{10} \text{ cm}^{-3}$	$9.3 \times 10^{10} \text{ cm}^{-3}$
$n_{-o}$	—	$9.3 \times 10^{10} \text{ cm}^{-3}$

accomplished by writing and solving an simple equation which balanced the ion production and loss rates given the thruster geometry and argon flow rate [35].

The  $C_{60}$  data in Fig. 9 were analyzed using the method for electronegative plasmas in Appendix A, Section B, and those results are also shown in Table 2. It was found that the positive and negative ion densities were approximately equal and that the electron density was much smaller than the ion densities. Even though the total density of negatively-charged particles in the  $C_{60}$  plasma was about the same as that in the argon plasma, the current collected by the probe at plasma potential was much less than in the argon plasma because the vast majority of negative charge carriers were slow-moving  $C_{60}$  negative ions instead of fast-moving electrons.

### 3. Comparison of Probe and Beam-Extraction Results

Before an attempt is made to compare experimentally-acquired beam current data with calculations of expected beam current based on Langmuir probe measurements that were acquired without beam extraction, it should be noted that the plasma properties inside the discharge chamber can be significantly different with and without beam extraction. One reason for this, discussed by Brophy [4], is that higher neutral densities in the chamber are expected without beam extraction. This is especially the case for efficient thrusters where the propellant utilization efficiency is very high, i.e. the majority of propellant molecules in the thruster leave the chamber as accelerated ions rather than as neutrals that leak through the grid open area. For thrusters with very low utilizations, however, propellant loss via beam extraction is of much less relative importance. Thus, it is expected for the argon and  $C_{60}$  thrusters investigated in this study where the utilizations were very low, the discharge chamber plasma properties will not be significantly different

with and without beam extraction, and comparisons of measured and calculated beam currents will be both valid and useful.

The beam current that can be extracted from a given discharge chamber plasma may be approximated using the plasma properties and grid geometry. The relationship is:

$$J_B = e n_{+s} v_{+s} A_g \quad (1)$$

where all symbols and variables are defined in Appendix B. The positive ion velocity at the sheath edge ( $v_{+s}$ ) is called the Bohm velocity, which in a Maxwellian, electropositive plasma is given by:

$$v_{+s} = \sqrt{\frac{k_B T_e}{m_+}} \quad (2)$$

Additionally, in a Maxwellian, electropositive plasma, the relationship between the positive ion density at the sheath edge ( $n_{+s}$ ) and in the bulk plasma ( $n_{+o}$ ) is:

$$n_{+s} = 0.61 n_{+o} \quad (3)$$

(see Ref. 35 or Eq. A26). The electron temperature and ion density for the argon discharge in Fig. 9 were used in Eq. 1 to predict a beam current of 34 mA, whereas the actual beam current measured under the same operating conditions was 46 mA. This difference between calculated and measured beam currents is not remarkable; recall that the plasma properties may be slightly different in this thruster with and without beam extraction under the same operating conditions [4], and the active extraction area is certainly slightly greater than the physical area of the screen grid holes ( $A_g$ ) which was used to calculate beam current. There are also errors associated with the measurement of the plasma properties which are discussed in Appendix A, Sect. D.

The plasma properties measured in the C<sub>60</sub> discharge can also be used to calculate a beam current. At first it may appear, since the positive ion density is essentially the same as in the argon discharge, that a sizable beam current should be extracted from the C<sub>60</sub> discharge. This is not necessarily the case, since for an electronegative plasma such as C<sub>60</sub> the Bohm velocity can be significantly different than in an electropositive plasma such as argon. The Bohm velocity in a Maxwellian, electronegative plasma is given by [36]:

$$v_{+s} = \sqrt{\frac{k_B T_e}{m_+} \left( \frac{1 + \alpha_s}{1 + \gamma \alpha_s} \right)} \quad (4)$$

where the dimensionless parameters  $\alpha_s$  and  $\gamma$  are defined by:

$$\alpha_s = \frac{n_{-s}}{n_{es}}; \quad \gamma = \frac{T_e}{T_-}. \quad (5)$$

The parameter  $\alpha$  is called the negative ion concentration. It is the ratio of negative-ion to Maxwellian-electron density in the plasma and is a critical parameter for electronegative plasmas;  $\alpha_s$  is the negative ion concentration at the edge of the plasma sheath adjacent to the grid apertures. Note that Eq. 4 reduces to the traditional Bohm expression (Eq. 2) for a plasma containing no negative ions ( $n_{-s} = 0$ ).

For the case of a strongly electronegative gas (i.e.  $n_{-s} \gg n_{es}$ ) the negative ion concentration will be much larger than unity, and if the electron temperature is greater than the negative ion temperature (i.e.  $\gamma > 1$ , which is the usual case) then Eq. 4 reduces to an expression that essentially only depends on  $T$ . (instead of  $T_e$ ). In this case, the Bohm velocity is reduced by a factor of the square root of the temperature ratio  $\gamma$ . The beam current for a strongly electronegative gas will then be given by:

$$J_B \approx en_{+s} A_g \sqrt{\frac{k_B T_-}{m_+}}. \quad (6)$$

In order to calculate a beam current that could be extracted from the C<sub>60</sub> plasma, the values of  $n_{+s}$ ,  $\alpha_s$ , and  $T_-$  are needed. It is assumed that all heavy particles are in thermal equilibrium with each other and the discharge chamber walls ( $T_w = 800$  K) because the mean free path for heavy particle collisions with neutral molecules is about 5 cm, which is of the same size as the chamber dimensions. The mean free paths for negative and positive ionization are much greater than this. With the knowledge of the negative ion temperature, and thus the temperature ratio  $\gamma$ , the positive ion density and the negative ion concentration at the sheath edge were determined using the method of Appendix A, Sect. C2. For the C<sub>60</sub> data in Table 2,  $\gamma = 61$ ,  $n_{+s} = 5.6 \times 10^{10} \text{ cm}^{-3}$ , and  $\alpha_s = 210$ . It can be seen that, since the temperature ratio and negative ion concentration are so large, the beam current will be given by Eq. 6. Using these results, a beam current of 0.6 mA was calculated, which is close to half of the 1.5-mA beam current actually measured under similar operating conditions. This is a reasonably good agreement given the limitations of the probe measurements and beam current calculations. These experiments performed with RF thrusters demonstrate that a significant negative ion concentration exists in the C<sub>60</sub> discharge and that it is the primary cause of the very small extracted beam currents.

## B. Direct-Current Thruster

The two main difficulties with the RF thruster operation on C<sub>60</sub>, i.e. the necessity of an electron source and the relatively large population of negative ions, prompted the investigation of a DC thruster. An important benefit for research with C<sub>60</sub> propellant is

that the DC source can produce a plasma with a very different electron energy distribution than the RF source, which may yield a different negative ion concentration. In the RF source, the free electrons have essentially a Maxwellian distribution and are continually being accelerated and decelerated by the RF electric fields, such that those with enough energy to create positive  $C_{60}$  ions may be decelerated and create negative ions instead. In contrast, the electron energy distribution in DC sources is typically characterized by two groups of electrons: a group of low-temperature Maxwellians and a group of high-energy primaries [37]. The energy of a primary electron does not change until it has an inelastic collision with a  $C_{60}$  molecule, so it is unlike a high-energy electron in the RF source. Thus, it might be expected that the DC source will feature greater positive ionization rates and reduced negative ionization rates than the RF source. The DC thruster was built and studied for the primary purpose of investigating the relationship between the extracted beam and the plasma properties through thruster operation and plasma diagnostics, in a similar fashion as was done for the RF thruster.

### 1. Ion Beam Extraction

The DC thruster was operated on argon and  $C_{60}$  propellant under a variety of operating conditions and beam-current data were obtained in the same manner as they were for the RF thruster experiments. There was no attempt, however, to maximize the beam current with  $C_{60}$  propellant by changing the thruster design or operating conditions. Typical operating conditions and beam currents for the two propellants are shown in Table 3.

The thruster performance parameters for the two propellants were very different than in the RF thruster. The propellant utilizations were 1-5% for argon and 5-8% for

Table 3. Typical DC Thruster Operating Conditions.

	Argon	C <sub>60</sub>
$\dot{m}$	~200 mA eq.	20-60 mA eq.
V <sub>D</sub> , J <sub>D</sub>	45 V, 1-3 A	45 V, 1-3 A
V <sub>+</sub> , V <sub>-</sub>	+500-800 V, -200 V	+800-1000 V, -200 V
J <sub>B</sub>	2-10 mA	1-4 mA

C<sub>60</sub>, as opposed to 25% and 2% for argon and C<sub>60</sub>, respectively, in the RF thruster. The beam ion energy costs were about 13,000 eV/ion for argon and 45,000 eV/ion for C<sub>60</sub>, in contrast to the 8200 and 170,000 eV/ion for argon and C<sub>60</sub>, respectively in the RF thruster. It can be seen that for argon propellant the DC thruster yielded poorer performance than the RF thruster, and for C<sub>60</sub> propellant the DC thruster performance was better than for the RF thruster. Note that these are rough comparisons, though, for non-optimized thrusters with different operating conditions. It is important, however, that a greater C<sub>60</sub> beam current was extracted from the DC thruster with a lower flow rate and discharge power than the RF thruster. Langmuir probe measurements were again undertaken to determine plasma properties in argon and C<sub>60</sub> discharges and to compare the results with beam current measurements.

## 2. Langmuir Probe Measurements

Measurements were made in both argon and C<sub>60</sub> plasmas under a wide variety of operating conditions. Typical probe traces acquired in argon and C<sub>60</sub> plasmas are shown in Fig. 10 as probe current density vs. voltage, where the true magnitudes are plotted, i.e. the argon data have not been scaled. Note that the plasma potentials are the same (~48 V) and the probe currents at plasma potential are modestly different. Otherwise, the probe

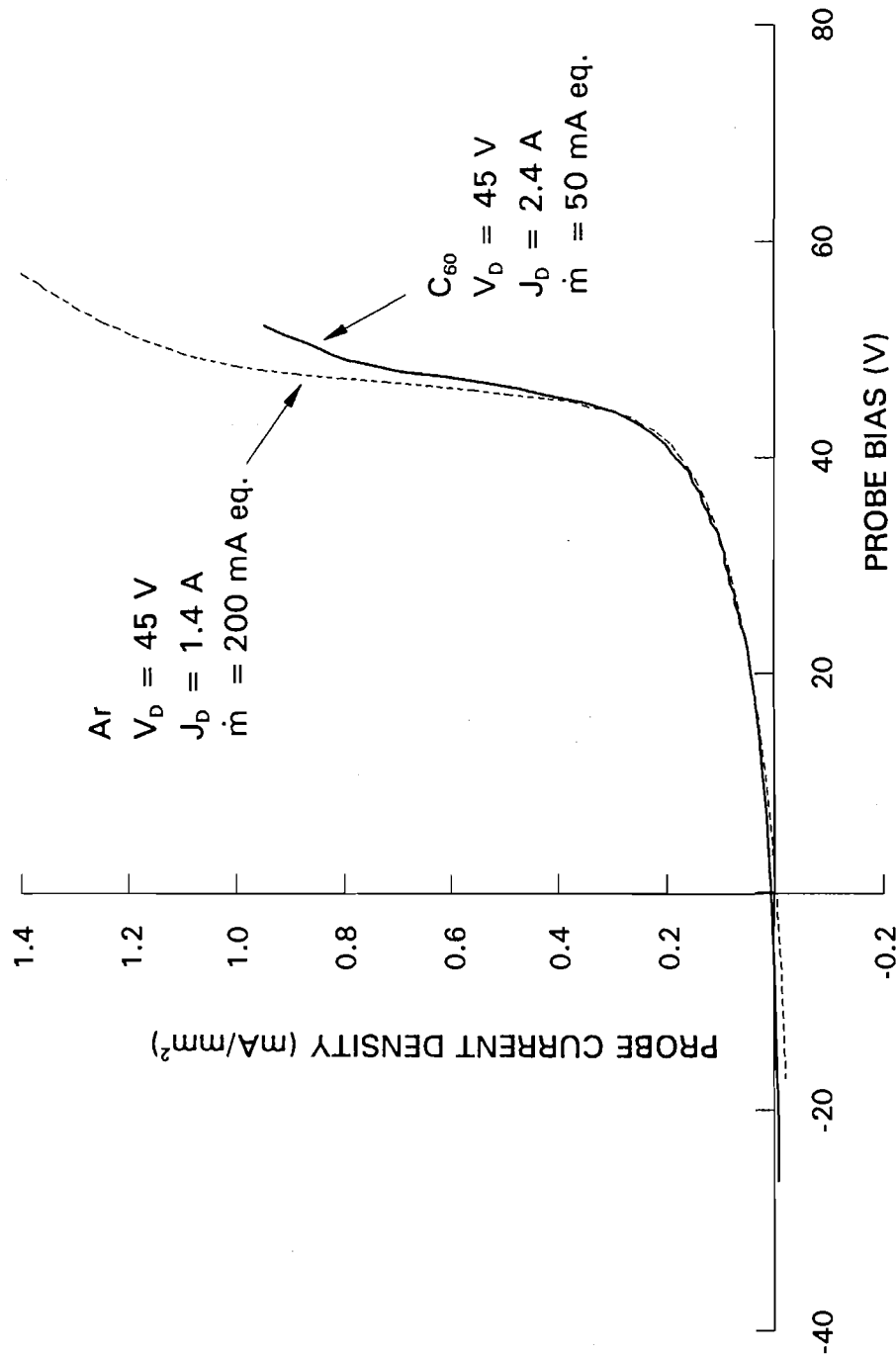


Fig. 10 Langmuir Probe Traces Acquired in Argon and  $C_{60}$  DC Plasmas.

traces look very similar to each other. This is in contrast to the probe traces acquired in the RF thruster (see Fig. 9) where the plasma potentials, the probe currents at plasma potential, and the general shape of the traces were all markedly different for the two propellants. Note also that for the  $C_{60}$  probe trace in Fig. 10 the probe current at plasma potential is much larger than the current at negative probe biases, which indicates a much lower negative ion concentration than was measured in the RF source.

Close inspection of the argon and  $C_{60}$  probe traces in Fig. 10 reveals an electron distribution consisting of both Maxwellian and primary electrons, a distribution which is commonly observed in DC ion thrusters [37]. The traces were analyzed using the method in Appendix A, Sect. C to determine the plasma parameters and the results are displayed in Table 4. The results of the analysis show that the positive ion density and the electron temperature in the argon discharge were much less than in the RF discharge, and this may partly explain the lesser beam current extracted from the DC thruster with argon propellant. In contrast, the  $C_{60}^+$  density in the DC discharge was three times greater than it was in the RF discharge, and this may partly explain the greater beam current extracted

Table 4. Typical Plasma Parameters in DC Discharges.

	Argon	$C_{60}$
$n_{p0}$	$1.2 \times 10^9 \text{ cm}^{-3}$	$9.8 \times 10^8 \text{ cm}^{-3}$
$n_{e0}$	$2.8 \times 10^{10} \text{ cm}^{-3}$	$1.3 \times 10^{10} \text{ cm}^{-3}$
$n_{+0}$	$2.9 \times 10^{10} \text{ cm}^{-3}$	$3.4 \times 10^{11} \text{ cm}^{-3}$
$n_{-0}$	—	$3.2 \times 10^{11} \text{ cm}^{-3}$
$T_e$	2.2 eV	3.3 eV
$\epsilon_p$	47 eV	47 eV

from the DC thruster. The results also show that the  $C_{60}$  plasma contained nearly equal densities of negative and positive ions and that the negative ion concentration in the bulk plasma ( $\alpha_o$ ) was 24, much less than the value of 310 measured in the RF plasma. Over the range of discharge conditions that were investigated with the Langmuir probe ( $V_D = 30-60$  V,  $J_D = 1-3$  A,  $i_n = 20-60$  mA eq.) the negative ion concentration in the bulk  $C_{60}$  plasmas ranged from about 10 to 70. This is a significant improvement over the negative ion concentration measured in RF plasmas, but it is still fairly large.

### 3. Comparison of Probe and Beam-Extraction Results

A beam current can be calculated using the measured plasma parameters as done previously for the RF tests, but the expressions for the Bohm velocity and the positive ion density at the sheath edge will be different due to the presence of the primary electrons. These expressions are derived in Appendix A, Sect. C. The Bohm velocity in a plasma containing Maxwellian electrons, primary electrons, and negative ions is given by:

$$v_{+s} = \sqrt{\frac{k_B T_e}{m_+} \left( \frac{1 + \alpha_s + \beta_s}{1 + \gamma \alpha_s + \frac{1}{2} \gamma_p \beta_s} \right)} \quad (7)$$

where the dimensionless parameters  $\beta_s$  and  $\gamma_p$  are defined by:

$$\beta_s \equiv \frac{n_{ps}}{n_{es}}; \quad \gamma_p \equiv \frac{k_B T_e}{\epsilon_p}. \quad (8)$$

The parameter  $\beta_s$ , called the primary electron concentration, is the ratio of primary-electron to Maxwellian-electron density, and  $\gamma_p$  is the ratio of electron temperature to primary electron energy. Both of these parameters will typically be small in a DC thruster discharge. Recall that  $\alpha_s$  is the negative ion concentration at the sheath edge and  $\gamma$  is the ratio of electron to negative-ion temperature.

The measured plasma properties for the DC argon plasma in Table 4 were used to calculate an extractable beam current with Eq. 7, noting that  $\alpha_s = 0$  in this case. A primary electron concentration at the sheath edge ( $\beta_s$ ) of 0.069 was calculated using the method of Appendix A, Sect. C2, the electron temperature-to-energy ratio ( $\gamma_p$ ) was 0.047, and the positive ion density at the sheath edge was found to be  $1.8 \times 10^{10} \text{ cm}^{-3}$ . Using these data in Eqs. 1 and 7, it was predicted that a 4.4-mA beam current could be extracted from the discharge plasma, which is very close to the 4.5-mA beam current actually extracted from the thruster operating under identical discharge conditions, but probably a fortuitous agreement. It can be seen that the beam current extracted from the DC thruster is much lower than in the RF thruster because of the much smaller positive ion density and electron temperature in the DC discharge.

In a strongly electronegative plasma such as  $C_{60}$ , the Bohm velocity of Eq. 7 will again be dominated by the relatively large negative ion concentration at the sheath edge since the values of  $\beta_s$  and  $\gamma_p$  are typically small (for the  $C_{60}$  data in Table 4,  $\alpha_s = 14$ ,  $\beta_s = 0.074$ , and  $\gamma_p = 0.070$ ). The positive ion density at the sheath edge in the  $C_{60}$  plasma was  $2.0 \times 10^{11} \text{ cm}^{-3}$ , and a beam current of 2.1 mA was calculated using the plasma parameters. The measured beam current extracted from the thruster operating under similar discharge conditions was 2.8 mA, and this agrees well with the predicted beam current. If the negative ion concentration did not affect the Bohm velocity in the  $C_{60}$  plasma (i.e. the Bohm velocity was given by Eq. 2 instead of Eq. 7), the extractable beam current would have been 14 mA. Again, it is seen that the small beam currents extracted from the DC  $C_{60}$  thrusters, even though the positive ion densities are large, are a result of the relatively large negative ion concentrations in the discharge plasmas. Also, because

the Langmuir probe measurements did not show a significant reduction of the negative ion concentration when the discharge conditions were varied, it does not appear likely that large beam currents can be extracted from a thruster of this design.

### C. The Bohm Factor

As the RF and DC thruster experiments have shown, the presence of a large negative ion concentration in a C<sub>60</sub> thruster reduces the beam current that can be extracted from the thruster. This effect should also extend to any propellant which may form negative ions. It is then logical to ask how much the negative ion concentration must be reduced in order to achieve a more reasonable Bohm velocity, and hence beam current. In order to address this question, consider the expression for the Bohm velocity in a plasma containing negative ions and primary electrons, Eq. 7. If this “modified” Bohm velocity is divided by the “conventional” Bohm velocity given in Eq. 2, the following expression, which will be termed the Bohm factor, results:

$$\frac{v_{+s}}{\sqrt{\frac{k_B T_e}{m_+}}} = \sqrt{\frac{1 + \alpha_s + \beta_s}{1 + \gamma \alpha_s + \frac{1}{2} \gamma_p \beta_s}} \quad (9)$$

For a plasma containing only Maxwellian electrons, the Bohm factor would be unity; for a plasma also containing primary electrons the Bohm factor could be greater than one depending on the value of  $\gamma_p$ ; and for a plasma containing negative ions the Bohm factor could be much less than unity.

The Bohm factor is plotted in Fig. 11 as a function of the negative ion concentration at the sheath edge ( $\alpha_s$ ) for typical values of  $\gamma$ ,  $\gamma_p$ , and  $\beta_s$  in a DC discharge.

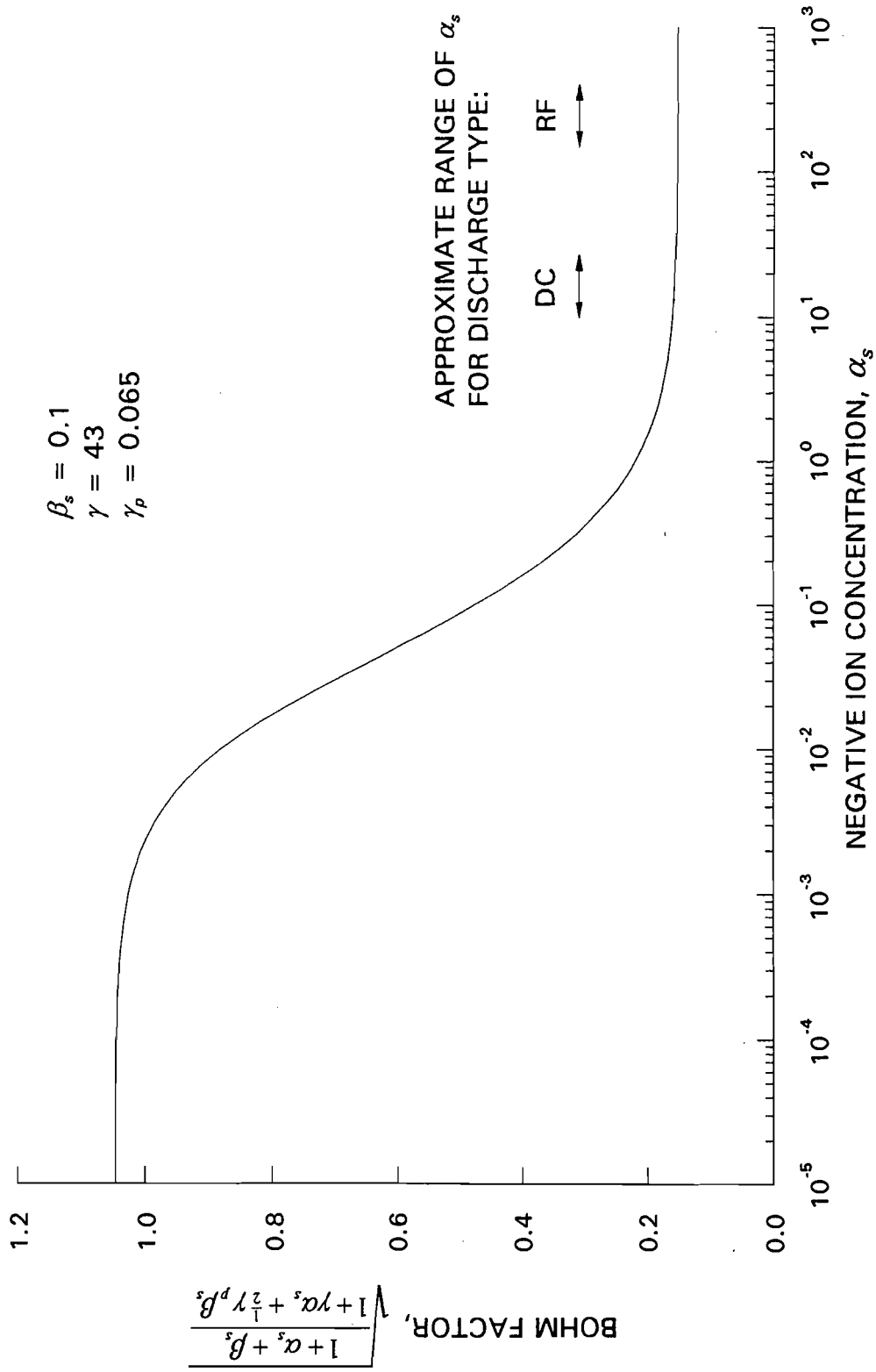


Fig. 11 Variation of Bohm Factor with Negative Ion Concentration.

The ranges of negative ion concentration measured in DC and RF  $C_{60}$  discharges are indicated on the figure. It can be seen that a negative ion concentration greater than about ten yields a Bohm factor, and thus a Bohm velocity, that is significantly less than the maximum plotted values which are typical of those achieved in noble gas thrusters. In order to minimize the effect of the negative ions on the Bohm velocity, Fig. 11 suggests that the negative ion concentration should be reduced to a value of less than  $10^{-2}$ . This would involve a reduction of  $\alpha_s$  of more than three orders of magnitude below the values measured in this study. There is no indication, however, from the range of operating conditions explored in this study for RF and DC thrusters, that such a large reduction in the negative ion concentration and correspondingly large increase in beam current can be achieved.

It may be possible, though, for a plasma discharge to have an electron distribution that does not produce a large negative ion density. If it is assumed that the negative ion density in a plasma is proportional to the rate of negative ion production, then the rate factor for negative ion production by Maxwellian electrons can provide useful information. The Maxwellian rate factor for negative ionization was calculated using the cross-section data in Fig. 2 and the results are shown in Fig. 12, along with the positive ionization rate factor for comparison, as a function of electron temperature. It can be seen that the negative ion production rates are near a maximum at the electron temperatures measured in the RF and DC  $C_{60}$  plasmas (3-4 eV). Based on the rate factor data in the figure, it appears unlikely that the negative ion concentrations can be reduced by an order of magnitude or more in  $C_{60}$  plasmas with appreciable Maxwellian electron populations, except for at very low electron temperatures, i.e. much less than 1 eV.

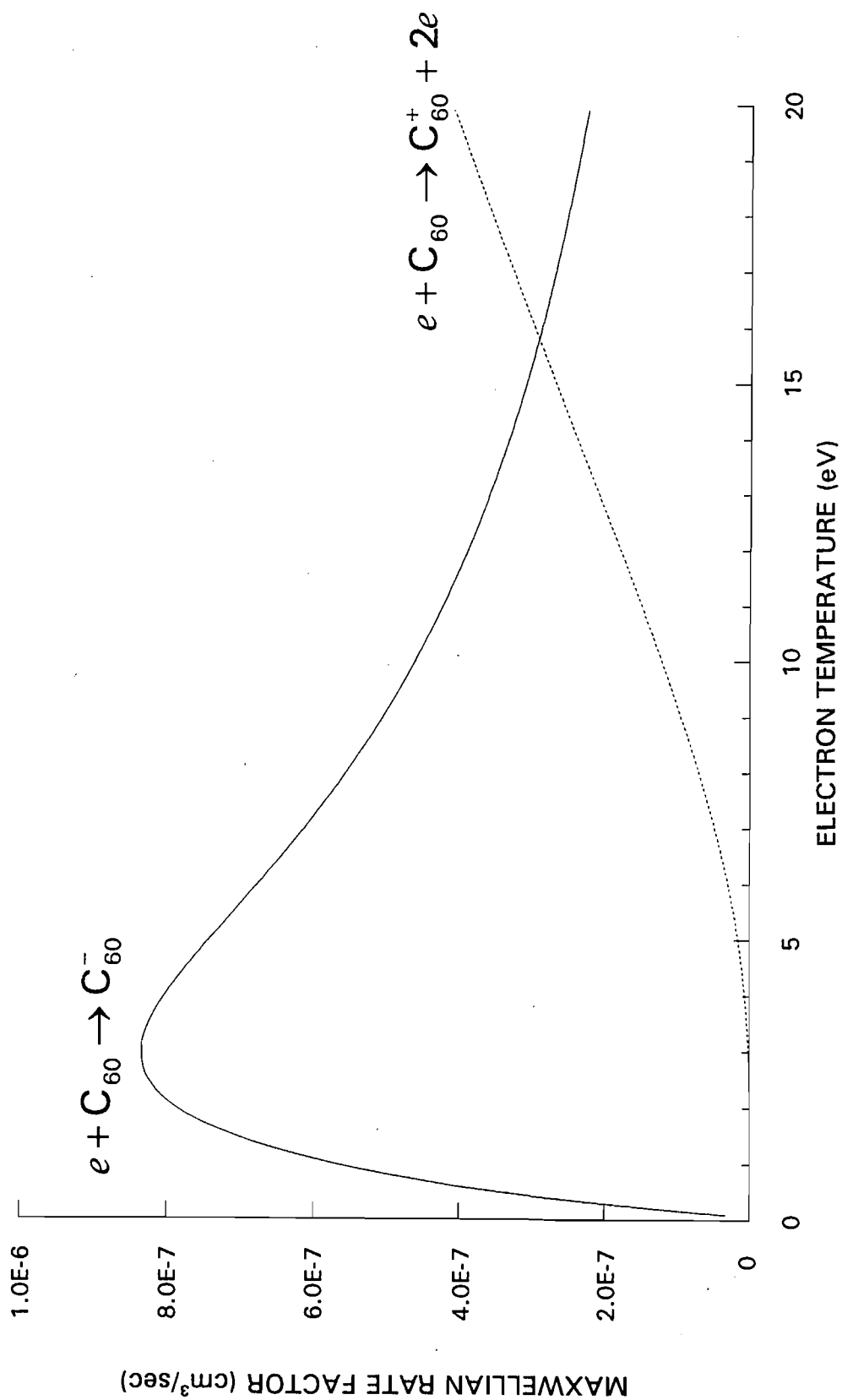


Fig. 12 Maxwellian Rate Factors for Ionization of  $C_{60}$ .

If  $C_{60}$  thrusters are doomed to have low beam currents because of order-of-magnitude reductions in the Bohm velocity caused by negative ions, then the thruster electrical efficiency will accordingly suffer. Recall that part of the initial attractiveness of  $C_{60}$  propellant was the possible efficiency increase at low specific impulses for a given beam-ion energy cost (see Fig. 1). The value of the beam-ion energy cost is closely approximated by the discharge power divided by the beam current [4]. If, for a given discharge power, the beam current is reduced by a factor of ten, then  $\varepsilon_B$  will increase by a factor of ten. The effect of increased  $\varepsilon_B$  on electrical efficiency for  $C_{60}$  propellant is compared to xenon propellant in Fig. 13, assuming that the discharge powers would be equivalent. It is seen that the possible benefits in efficiency due to the large  $C_{60}$  ion mass are lost due to the reduced beam currents and that a  $C_{60}$  thruster then provides worse performance than does a xenon thruster. Thus, the problem of relatively large negative ion concentration in  $C_{60}$  thrusters must be solved before  $C_{60}$  can become truly attractive as a propellant for ion thrusters.

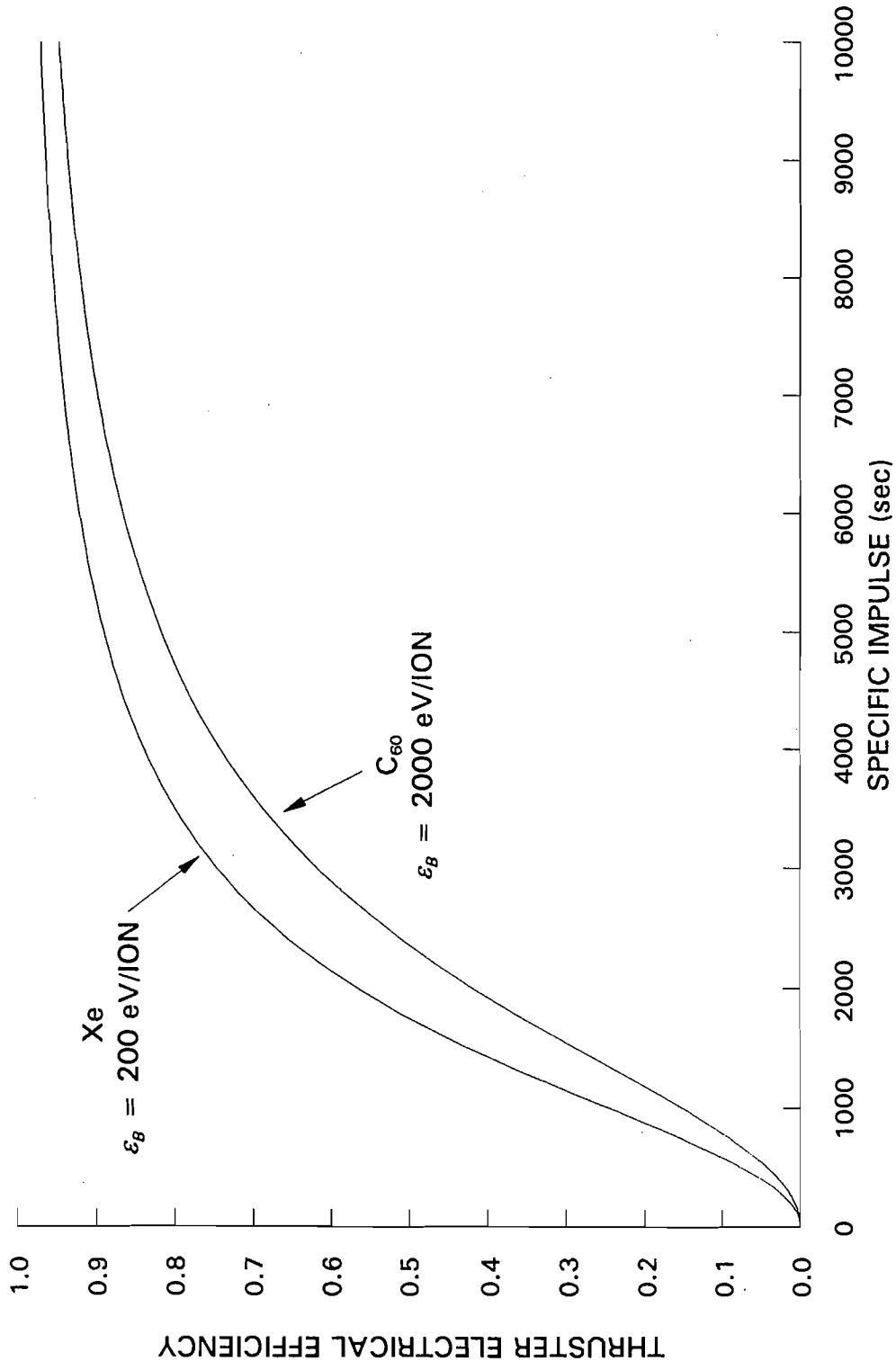


Fig. 13 Comparison of Theoretical Thruster Electrical Efficiency for Xenon and  $C_{60}$  with Different Values of  $\epsilon_B$ .

## IV. FRAGMENTATION OF THE C<sub>60</sub> MOLECULE

As was discussed in Chapter I, C<sub>60</sub> fragmentation has been observed in many different plasma discharges and ion beams. Fragmentation in an ion thruster discharge chamber could be caused by molecules impinging on a hot cathode or by processes inherent in producing a plasma, i.e. the pumping of C<sub>60</sub> vibrational modes by single or multiple collisions with energetic particles. Observation, testing, and modeling were done in this study in an attempt to quantify fragmentation in the chamber and to determine the basic mechanisms which govern the fragmentation process.

### A. Residue Analysis and Measurement

After each experiment in which a C<sub>60</sub> plasma was produced, whether it was with RF or DC power or in combination with an argon plasma, black/brown carbonaceous deposits were found on the interior surfaces of the discharge chamber. It was expected that these deposits were from fragmented C<sub>60</sub>, based on the results of residue analysis from other research [24,25]. In order to determine if this was the case, simple toluene-solubility tests were conducted with residue samples. It was found that samples dissolved to varying degrees in toluene, but significant amounts of insoluble material were always observed, thereby indicating the presence of non-C<sub>60</sub> material.

The residue samples were also subjected to mass spectrometric analysis. A control test in which no fragmentation should have occurred was first performed by sublimating  $C_{60}$  from the vaporizer into the discharge chamber with the discharge power and filament heater power off, and collecting residue that accumulated on a relatively cool portion of the grid surface (there was no visible accumulation on the quartz walls because they were maintained at temperatures above the  $C_{60}$  condensation temperature). The results of the analysis, which are presented as the relative abundance of each of the particle mass-to-charge ratios, are shown in Fig. 14. Visible are singly-charged ( $m/z = 720$ ) and doubly-charged ( $m/z = 360$ )  $C_{60}$  ions as well as some fragments of those ions (e.g.  $C_{58}^+$  at  $m/z = 696$ ). These fragments that are observed in Fig. 14 are known to be caused by the 70-eV electron-impact ionization used in the mass spectrometer. Trace amounts of impurities are observed at  $m/z$  less than 150 as well as polysiloxane peaks ( $m/z = 207, 281$ ) which come from silicone greases used in the thruster vacuum system. The mass spectrum of the as-received  $C_{60}$  was also measured and it was essentially the same as Fig. 14 but with much lesser signals at  $m/z$  less than 300.

Mass spectrometric analysis of the residue coating the chamber walls after the RF thruster was operated on  $C_{60}$  is shown in Fig. 15. As the figure suggests, no signals for ionized  $C_{60}$  or fragments are visible. There are large signals at  $m/z < 150$  and an additional peak at  $m/z = 652$  which comes from an unknown but probably non- $C_{60}$  source (the mass-to-charge ratio is not a multiple of the carbon atomic mass of 12). Since fragmented  $C_{60}$  is expected to decompose to amorphous carbon on discharge chamber surfaces, it is likely that the signals at  $m/z < 150$  are hydrocarbon and other species adsorbed by the carbon on the chamber walls from the atmosphere after the vacuum was broken. Analysis of many

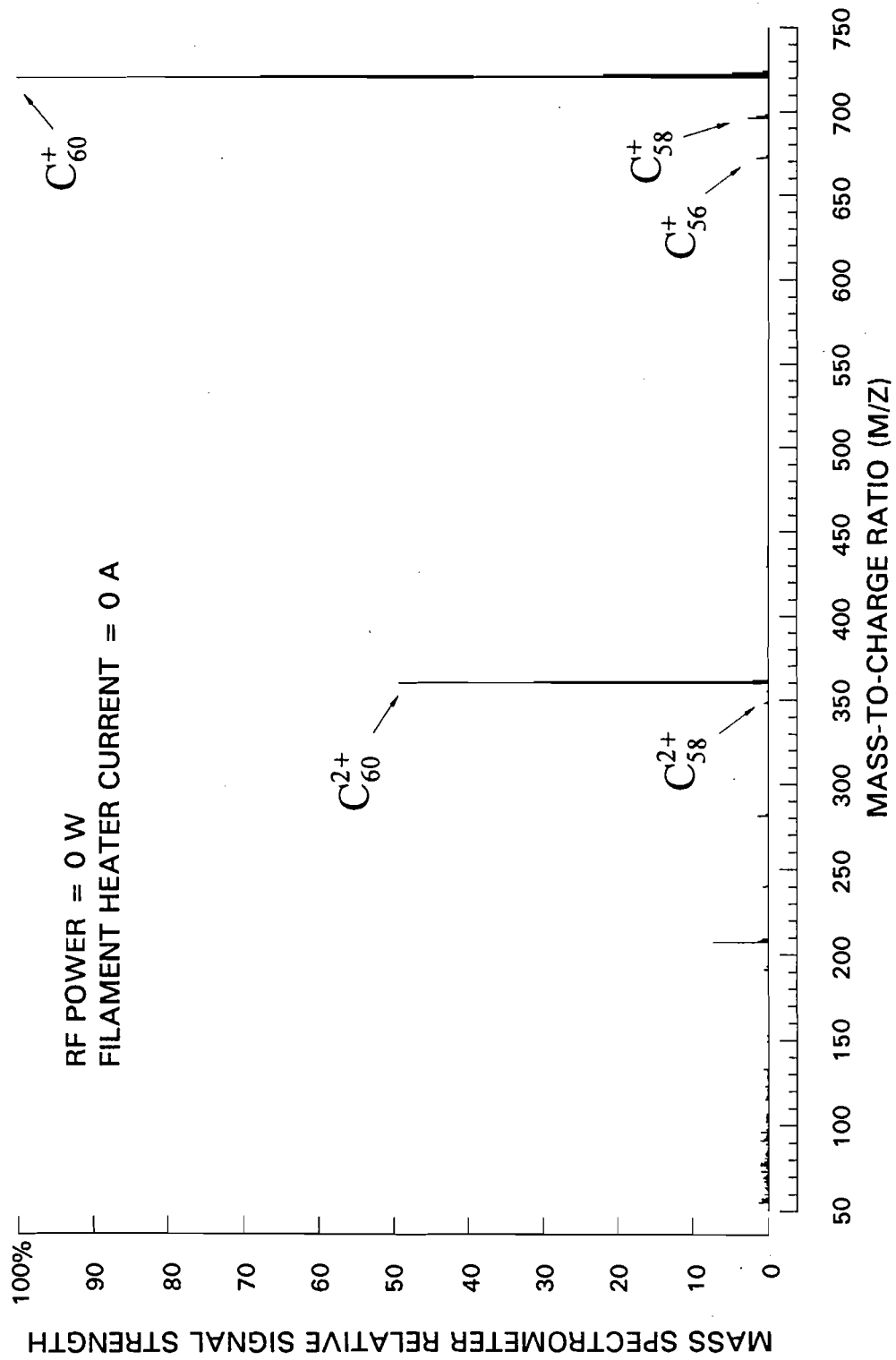


Fig. 14  $C_{60}$  Mass Spectrum After No-Plasma Test.

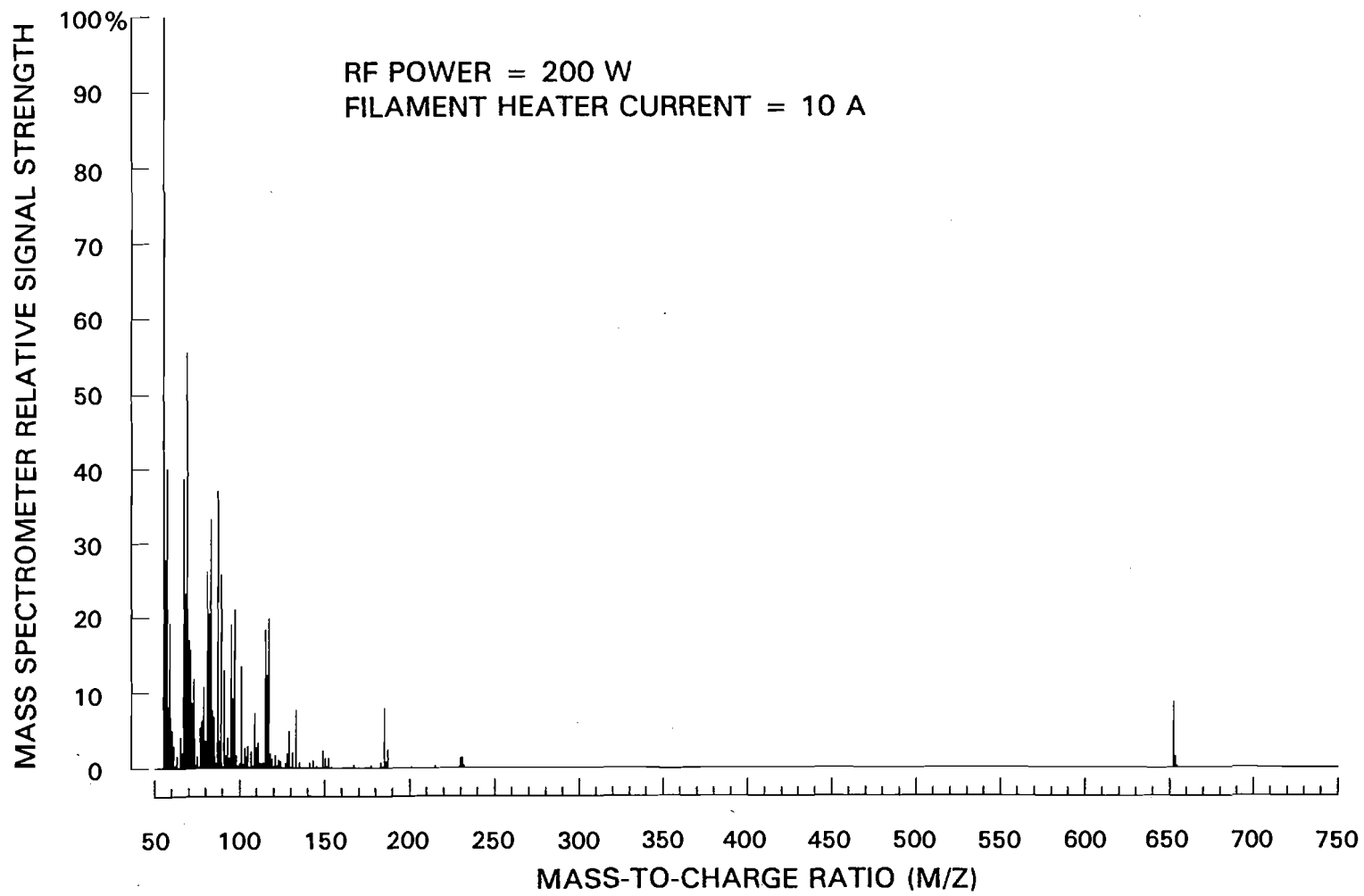


Fig. 15 C<sub>60</sub> Mass Spectrum After Plasma Test.

other residue samples collected after thruster operation showed results similar to that of Fig. 15, although in some cases small  $C_{60}$  signals were observed. Still, it seems clear based on these simple studies that substantial  $C_{60}$  fragmentation was occurring inside the discharge chamber.

An indication of the extent of fragmentation in the discharge chamber is given by the mass of carbonaceous residue that accumulated on the chamber walls during an experiment. Several tests were conducted under different operating conditions with the RF thruster configuration in order to study mass accumulation. In each test, the flow rates of  $C_{60}$  into the chamber were similar and the chamber walls were heated to their operating temperature to minimize  $C_{60}$  condensation. The results are displayed in Table 5, where the mass that accumulated on the chamber walls during the indicated experiment is tabulated as the percentage of the mass that entered the chamber from the vaporizer, i.e. the accumulation fraction.

Table 5. Mass Accumulated on Chamber Walls.

RF POWER	ELECTRON SOURCE	ACCUMULATION FRACTION
Off	None	2%
Off	Tantalum Filament	19%
On	Tantalum Filament	20-30%
On	Argon Discharge	70%

The first test was conducted by feeding  $C_{60}$  into the discharge chamber when neither the filament heater power nor the RF power were supplied. As expected, there

was very little condensation on the walls. This condensation probably occurred on the upstream surface of the chamber adjacent to the water-cooled antenna. In the second test, the filament heater was operating (i.e. the filament was at a temperature greater than 2000 K) but the RF power remained off so that no plasma was produced. It can be seen that a substantial mass accumulated on the walls. Since pure  $C_{60}$  will not condense on the walls and the mass spectrometric analyses showed that there was negligible  $C_{60}$  in the wall residue, the mass accumulation in this test must be fragmented  $C_{60}$ . Also, since no plasma was produced in this test, it is argued that this fragmentation is only due to neutral molecules impinging on the filament surface. It is believed that the neutrals stick to the filament surface for a sufficient length of time so that they acquire the vibrational energy necessary for fragmentation.

Next, the RF power was applied in addition to the filament heater power so that a  $C_{60}$  plasma was produced. In this experiment a greater fragmentation was observed than in the previous test, thereby indicating that plasma processes in the discharge (i.e. bombardment of  $C_{60}$  by energetic particles) may induce fragmentation. Finally, an experiment was performed in which small flow of  $C_{60}$  was fed into an argon discharge, where the hot-filament electron source was not operating. This produced a much greater fragmentation than the other tests, and the fragmentation must have been due to only plasma processes because the filament was cold. Recall from Table 2 in Chapter III that the electron temperatures and densities in RF argon discharges were much greater than those in pure  $C_{60}$  discharges. Hence, more frequent and more energetic electron bombardment of  $C_{60}$  should occur, and it is argued that vibrational energy will be deposited in  $C_{60}$  clusters by the electrons at a greater rate thereby causing greater fragmentation.

Residue mass measurements were also recorded in the DC thruster, where it was found that over a range of testing conditions 60-70% of the mass entering the chamber accumulated on the walls. The tantalum filament used in the DC thruster, however, was physically much longer than in the RF thruster, and thus provided a larger hot surface area on which  $C_{60}$  could impact and degrade. In addition, electron energies and densities in the DC thruster were greater than in the RF thruster and this would be expected to cause a greater vibrational energy addition to the  $C_{60}$  clusters, and thus a greater amount of fragmentation.

#### B. Analysis of Extracted Ion Beams

Perhaps the best way to quantify the effects of fragmentation on ion thruster operation is to determine the composition of the extracted beam with a probe that is sensitive to mass-to-charge ratio. An  $E \times B$  probe, which is sensitive to charged-particle velocity, can be used for these measurements because the velocity of the beam ions depends on their mass-to-charge ratio. Such measurements were made by Anderson and Fitzgerald [24] at the Jet Propulsion Laboratory (JPL) using a filament-cathode DC thruster, and significant fragmentation was observed. Subsequent to that study, additional experiments were performed at JPL with some surprising results, and those data were provided for this investigation of thruster fragmentation. Details of the thruster and  $E \times B$  probe can be found in Ref. 24.

A typical probe trace obtained at an operating condition that yielded substantial fragmentation is shown in Fig. 16. It gives normalized current collected by the probe as a function of the particle mass-to-charge ratio for the operating conditions indicated. The

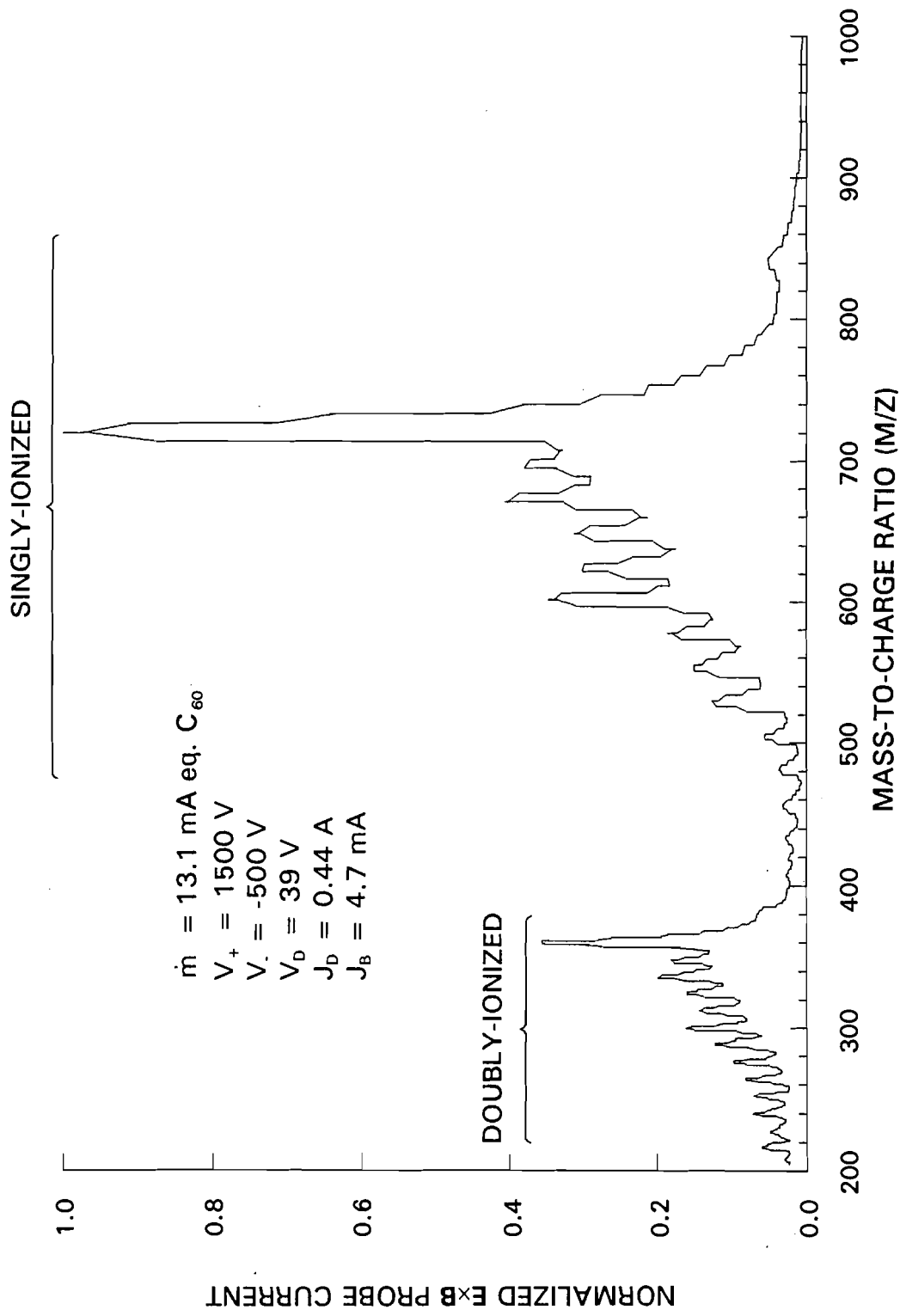


Fig. 16 ExB Probe Measurement from JPL Thruster - Higher Flow Rate Condition. (Courtesy, J. Anderson JPL)

distribution of fragments seen in the figure is typical of that seen in mass-spectrometric studies of fragmentation [12] indicating the sequential loss of  $C_2$  molecules from  $C_{60}$  and fragments,  $C_{2n}^+ \rightarrow C_{2n-2}^+ + C_2$ . Doubly-ionized  $C_{60}$  and fragments are also observed in Fig. 16. In contrast to these probe data are those depicted in Fig. 17 for different operating conditions where very little fragmentation is observed. Note that in the latter figure the mass flow rate, and hence the neutral density, is about one fourth of that in Fig. 16 and the discharge voltage and current are greater. Analysis of all of the  $\mathbf{E} \times \mathbf{B}$  probe traces showed that, in general, fragmentation was less severe at lower mass flow rates and more severe at higher mass flow rates. There was no apparent trend with either discharge voltage or current, but there was also no systematic study of the effect of those parameters on fragmentation.

It is possible that the fragmentation observed in Fig. 16 could have occurred either in the discharge chamber before the ions were accelerated, or after they were accelerated but before they were detected by the  $\mathbf{E} \times \mathbf{B}$  probe. For example, the  $C_{58}^+$  ions formed in the discharge chamber have  $m/z = 696$  and they yield the peak produced at this mass-to-charge ratio in Fig. 16. On the other hand, ions that are  $C_{60}^+$  as they are accelerated through the grids and then fragment to  $C_{58}^+$  before they reach the  $\mathbf{E} \times \mathbf{B}$  probe, are sensed as part of the  $C_{60}^+$  signal at  $m/z = 720$ . This occurs because 1) the  $\mathbf{E} \times \mathbf{B}$  probe is sensitive to velocity only, 2) all ions that pass through the grids as  $C_{60}^+$  exit with the same velocity, and 3) ejection of a  $C_2$  molecule to form  $C_{58}^+$  should not change this velocity significantly. The magnitude of the  $C_{58}^+$  contribution to the  $m/z = 720$  peak can be estimated by recognizing that all fragmentation is initiated in the discharge chamber and is characterized

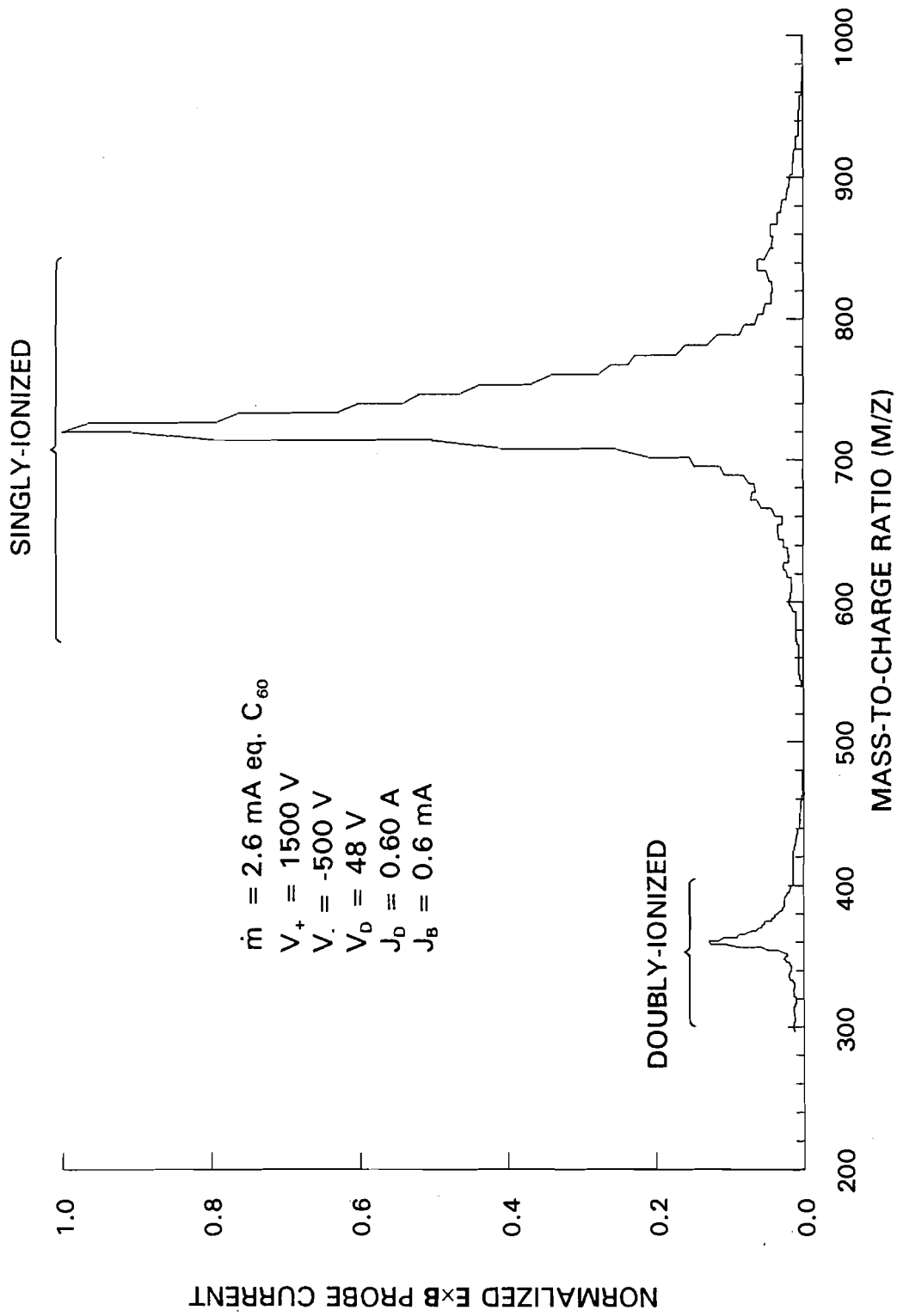


Fig. 17 ExB Probe Measurement from JPL Thruster - Lower Flow Rate Condition. (Courtesy, J. Anderson JPL)

by reaction times that may range from milliseconds to nanoseconds or less depending on the molecular vibrational energy. Further, the residence time of a molecule in the discharge chamber is on the order of milliseconds while the flight time to the  $\mathbf{E} \times \mathbf{B}$  probe collector under the operating conditions of Fig. 16 is about 50  $\mu\text{sec}$ . Hence,  $\text{C}_{60}^+$  ions with characteristic fragmentation times greater than  $\sim 1$  msec will have a probability of fragmenting in the discharge chamber that is  $\sim 20$  times that for the short flight time to the  $\mathbf{E} \times \mathbf{B}$  probe. The ions with characteristic fragmentation times less than  $\sim 1$  msec will have an even lower probability of fragmenting during this flight. Thus, under worst-case conditions, the  $\text{C}_{60}^+$  contribution to the peak at  $m/z = 720$  will be at least an order of magnitude more than that due to  $\text{C}_{58}^+$  formed during the flight from the grids to the probe.

### C. Fragmentation Modeling

A simple modeling effort was performed with the following goals: 1) understand the basic phenomena that govern fragmentation, 2) identify possible thruster operating conditions that minimize or eliminate fragmentation, and 3) identify and evaluate alternative ion sources or ionization methods that could be used for ion thrusters which minimize negative ion formation and fragmentation. While much attention in the scientific literature has been focused on fragmentation kinetics in mass-spectrometric experiments where collisions between particles can be ignored, little modeling has been done in the plasma state where many collisions between particles can be expected. The model that has been developed here extends the work in the literature to the  $\text{C}_{60}$  plasmas that are formed in ion thrusters.

## 1. Model Development

It is known that  $C_{60}$  will fragment in a given timespan if the internal energy is increased to a sufficiently large value, e.g.  $\sim 40$  eV of vibrational energy is sufficient for fragmentation on a microsecond timescale. It follows from the unimolecular fragmentation theory that the *rate* of fragmentation depends on the vibrational energy, and experiments [13,38] have shown that the rate increases dramatically with vibrational energy. For example, the fragmentation rate at a vibrational energy of 51 eV is two orders of magnitude greater than at an energy of 40 eV. Thus, in order to determine the total fragmentation rate, the fragmentation rate must be determined for each infinitesimally small vibrational energy range, and the rates must be summed over all vibrational energies. This means the number density of positive ions at each infinitesimally small vibrational energy range, which is known as the distribution function for vibrationally-excited positive ions,  $dn_+/d\varepsilon_v$ , must be determined.

The fragmentation model was developed based on the principle of detailed balancing [39]. This principle states that not only is the total population of ions in equilibrium, but every individual group of ions with a specific vibrational energy must also be in equilibrium, i.e. the number density must not change with time:

$$\frac{d}{dt} \left( \frac{dn_+(\varepsilon_v)}{d\varepsilon_v} \right) = 0. \quad (10)$$

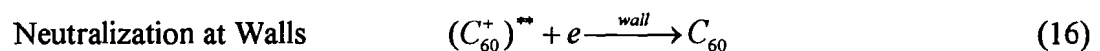
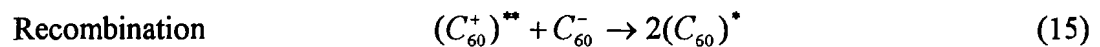
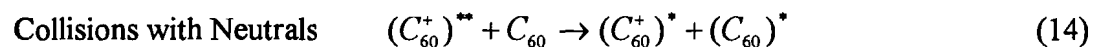
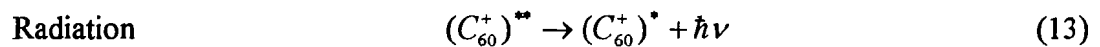
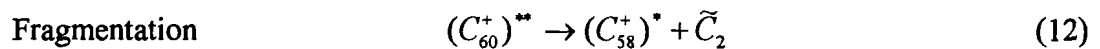
This is equivalent to stating that the rates of production and destruction of vibrationally-excited positive ions must be equal in each energy range  $\varepsilon_v$  to  $\varepsilon_v + d\varepsilon_v$ . Using this method, a rate equation can be written and solved for every vibrational energy group that may exist in the plasma, and the distribution function can be determined from the set of rate equations.

Filament-induced fragmentation will not be specifically incorporated into this model, thus it will be assumed that vibrational energy will be added to the  $C_{60}$  molecules in an ion thruster plasma discharge almost exclusively through electron impact. This is the case because the vibrational energies required for fragmentation (tens of eV) are too large to be pumped by collisions with other heavy particles, which are in equilibrium with the chamber wall temperature and thus have thermal energies of much less than 1 eV. It is further assumed for the model that the production of vibrationally-excited ions occurs only by primary electrons through the electron-impact ionization reaction:



where the asterisks (\*\*) denote a highly vibrationally excited molecule and the tilde ( $\tilde{\phantom{e}}$ ) denotes a particle with a relatively large kinetic energy. Vibrational energy addition is also possible via electron-impact excitation, but the necessary data for excitation reactions are not currently available in the literature and thus these reactions are not included in the model.

Once a vibrationally-excited positive ion is produced, it may lose vibrational energy through a number of plasma kinetic processes:



A vibrationally-excited ion may also be extracted through the grid set whereupon fragmentation is not of concern. The latter four processes (Eqs. 13-16) directly compete with fragmentation and will reduce the total rate of fragmentation to some extent, depending on their relative importance. Note that the recombination and neutralization reactions (Eqs. 15 and 16) remove a positive ion from the discharge. The radiation and neutral collision reactions (Eqs. 13 and 14) reduce the vibrational energy of positive ions; thus they will also be a production mechanism for the lesser vibrational energies, in addition to positive ionization. For the following discussion, a process which reduces the vibrational energy of a molecule will be termed a cooling process.

The rate equation for a specific vibrational energy may now be written assuming that the destruction mechanisms are given by Eqs. 12-16 and that the production is given by ionization and also by radiative and collisional cooling of upper vibrational levels, where applicable. Equating the production and destruction rates of vibrationally-excited positive ions for vibrational energy level  $\varepsilon_v$  yields the resulting expression:

$$n_n n_p \sigma_+(\varepsilon_p) v_p D(\varepsilon_p, \varepsilon_{ex}) V + \frac{dn_+(\varepsilon'_v)}{d\varepsilon_v} k_{rad}(\varepsilon'_v) V + \frac{dn_+(\varepsilon''_v)}{d\varepsilon_v} k_{colls} V = \frac{dn_+(\varepsilon_v)}{d\varepsilon_v} \left[ k_{frag}(\varepsilon_v) V + k_{rad}(\varepsilon_v) V + k_{colls} V + k_{rec} V + v_{+s} A_w \right] \quad (17)$$

where  $\varepsilon'_v$  and  $\varepsilon''_v$  denote upper vibrational levels that populate the  $\varepsilon_v$  level through radiation and collisions with neutrals, respectively. The terms and parameters in Eq. 17 will be addressed individually.

The first term in Eq. 17 gives the ionization rate for a specific primary electron energy  $\varepsilon_p$ . It depends on the neutral and primary electron densities, the positive ionization cross section at the primary electron energy, the primary electron velocity, the discharge

chamber volume, and a function  $D(\varepsilon_p, \varepsilon_{ex})$  which is called the energy deposition function. The energy deposition function describes the probability that a certain amount of vibrational energy will be added to the molecule during the ionization event, which occurs in the following manner. When a neutral  $C_{60}$  molecule is ionized by a primary electron, an amount of energy equal to the ionization potential of  $C_{60}$  ( $\varepsilon_{IP} = 7.6$  eV) must be given up by the primary electron, e.g. a 40-eV primary electron would be left with 32.4 eV of energy after the ionization event. It is also possible that some portion of the remaining energy of the primary electron will be deposited in electronic excitation of the molecule, e.g. 10 eV of the 32.4-eV primary electron could excite electronic levels in the molecule and thus the primary electron would leave with 22.4 eV of energy. Finally, it is known from experiment that the electronic excitation energy remaining in a  $C_{60}$  molecule after an ionization event (e.g. 10 eV) is rapidly converted into vibrational energy [12]; this is in fact a prerequisite for the unimolecular theory that has been successfully used to describe  $C_{60}$  fragmentation [19].

There is some debate in the literature as to how much of the primary electron energy can be deposited as vibrational energy in the  $C_{60}$  cluster during an ionization event [13,14,19,38,40]. An empirical form for the energy deposition function is often used [19], and the functional form that has been chosen for this model is that of Foltin *et al.* [13] but the function has been normalized as suggested by Forst [19] and Kolodney *et al.* [38]:

$$D(\varepsilon_p, \varepsilon_{ex}) = \frac{2}{(\varepsilon_p - \varepsilon_{IP})^2} (\varepsilon_p - \varepsilon_{IP} - \varepsilon_{ex}). \quad (18)$$

The parameter  $\varepsilon_{ex}$  is the primary electron energy that is deposited in the molecule as electronic excitation energy and is rapidly converted to vibrational energy. For a given

primary electron energy  $\varepsilon_p$ , the value of the function  $D(\varepsilon_p, \varepsilon_{ex})$  is the probability per unit energy that  $\varepsilon_{ex}$  energy will be deposited as vibrational energy in the molecule. Note that the probability is a maximum at  $\varepsilon_{ex} = 0$  and decreases linearly to zero at  $\varepsilon_{ex} = \varepsilon_p - \varepsilon_{IP}$ . Kolodney *et al.* [38] used a slightly different form of the energy deposition function for  $C_{60}$ , but the form of Foltin *et al.* [13] was chosen for this model because their results have generally received more acceptance in the literature. Finally, the neutral molecules have an initial, thermal vibrational energy because they are in equilibrium with themselves and the chamber wall ( $\varepsilon_{th} \approx 5$  eV at 800 K [14]), so that the total vibrational energy of the cluster after the ionizing event is  $\varepsilon_v = \varepsilon_{th} + \varepsilon_{ex}$ .

The cooling rates in Eqs. 12-15 are determined by the product of the vibrationally-excited ion distribution function, the reaction rate, and the chamber volume, as shown in the right-hand side of Eq. 17. Recall, the general fragmentation reaction for fullerene ions is  $C_{2n}^+ \rightarrow C_{2n-2}^+ + C_2$ . Experiments [13,38] have shown that the fragmentation kinetics are well described with an Arrhenius-type formula:

$$k_{frag} = B_f \exp(-E_f / k_B T_v) \text{ sec}^{-1} \quad (19)$$

where  $E_f$  is the activation energy required for the reaction,  $T_v$  is the vibrational temperature of the molecule,  $B_f$  is a pre-exponential factor, and  $k_{frag}$  is the reaction rate. The Arrhenius parameters for the fragmentation of  $C_{60}^+$  (Eq. 12) are  $B_f = 2.1 \times 10^{15} \text{ sec}^{-1}$  and  $E_f = 7.1$  eV [13]. A range of values for the fragmentation activation energy  $E_f$  have been reported in the literature, but the value used here is the one that has gained the most acceptance in the literature [41]. The relationship between vibrational energy and vibrational temperature is given by [38]:

$$\begin{aligned}
\varepsilon_v &\approx 7.2 + 0.0138 (T_v - 1000) && \text{for } 1000 \text{ K} < T_v < 1500 \text{ K} \\
\varepsilon_v &\approx 13.9 + 0.0143 (T_v - 1500) && \text{for } 1500 \text{ K} < T_v < 4000 \text{ K}
\end{aligned}
\tag{20}$$

where the vibrational energy is given in eV.

The  $C_{60}^+$  radiative cooling rate (Eq. 13) was determined from the work of Laskin and Lifshitz [42]. The rate is presented in Fig. 4 of their paper as a function of vibrational energy, and a curve fit to their data was found and used in the model:

$$k_{rad} = 10^{(2.05+0.0789 \varepsilon_v)} \text{ sec}^{-1} \tag{21}$$

where the vibrational energy is given in eV. The average photon energy emitted from the molecule is  $4k_B T_v$  [42]. Thus, the group of positive ions at energy level  $\varepsilon_v$  are depleted from that energy level at a rate of  $(dn_+/d\varepsilon_v)k_{rad}V$ , and they populate the lower energy level  $\varepsilon_v - 4k_B T_v$  at the same rate.

For collisional cooling (Eq. 14), Smirnov [43] assumes that the cross section for vibrational energy transfer in a collision between a vibrationally-excited ion and a non-excited neutral molecule is given by the cross section for polarization capture of the ion by the neutral, i.e. the Langevin cross section. The cross section and rate factor were determined [35] using the electric polarizability of  $C_{60}$  ( $84 \text{ \AA}^3$  [44]), and the collisional quenching rate was found to be given by:

$$k_{colls} = 1.13 \times 10^{-15} n_n \text{ sec}^{-1} \tag{22}$$

where the neutral density  $n_n$  is given in  $\text{m}^{-3}$ . Collisional cooling populates lower vibrational energies as does radiative cooling. The amount of vibrational energy that is transferred from an ion to a neutral during a collision was estimated in the following manner. For a large polyatomic molecule with many vibrational degrees of freedom such

as C<sub>60</sub>, the transfer of vibrational energy between molecules can be very efficient if the collision duration is sufficiently larger than the characteristic vibrational time [19,45,46]. The collision time was estimated [47] using the relative velocity of the molecules at 800 K and the molecular diameter of 7.1 Å [44], and the characteristic vibration times were calculated from the C<sub>60</sub> vibrational wave numbers which range from 263 to 1722 cm<sup>-1</sup> [48]. It was thus approximated that the duration of the ion-neutral collision is 13-83 vibrational periods, and it is assumed that this is sufficiently long for the total vibrational energy to equilibrate between the two particles during a collision.

Recombination of positive and negative ions (Eq. 15) was determined [35] to have a rate given by:

$$k_{rec} = 4.30 \times 10^{-15} n_- \text{ sec}^{-1} \quad (23)$$

where the negative ion density is given in m<sup>-3</sup>. Finally, the wall neutralization rate (Eq. 16) was found simply from the arrival rate of ions at wall surfaces, i.e. the product of the ion distribution function, Bohm velocity, and wall area.

All of the cooling mechanism rates are shown as a function of vibrational energy in Fig. 18, where the collisional and recombination cooling rates are given for typical plasma parameters, and the wall loss rate is given for the geometry of the thruster used in this study (the CSU geometry). The wall loss rate is different for different thruster geometries, e.g. the JPL thruster. At energies greater than 45 eV it is apparent that the fragmentation mechanism is dominant, and from about 25-45 eV radiation is the most important cooling mechanism. At lower energies the cooling is dominated by collisions with neutrals and recombination at wall surfaces.

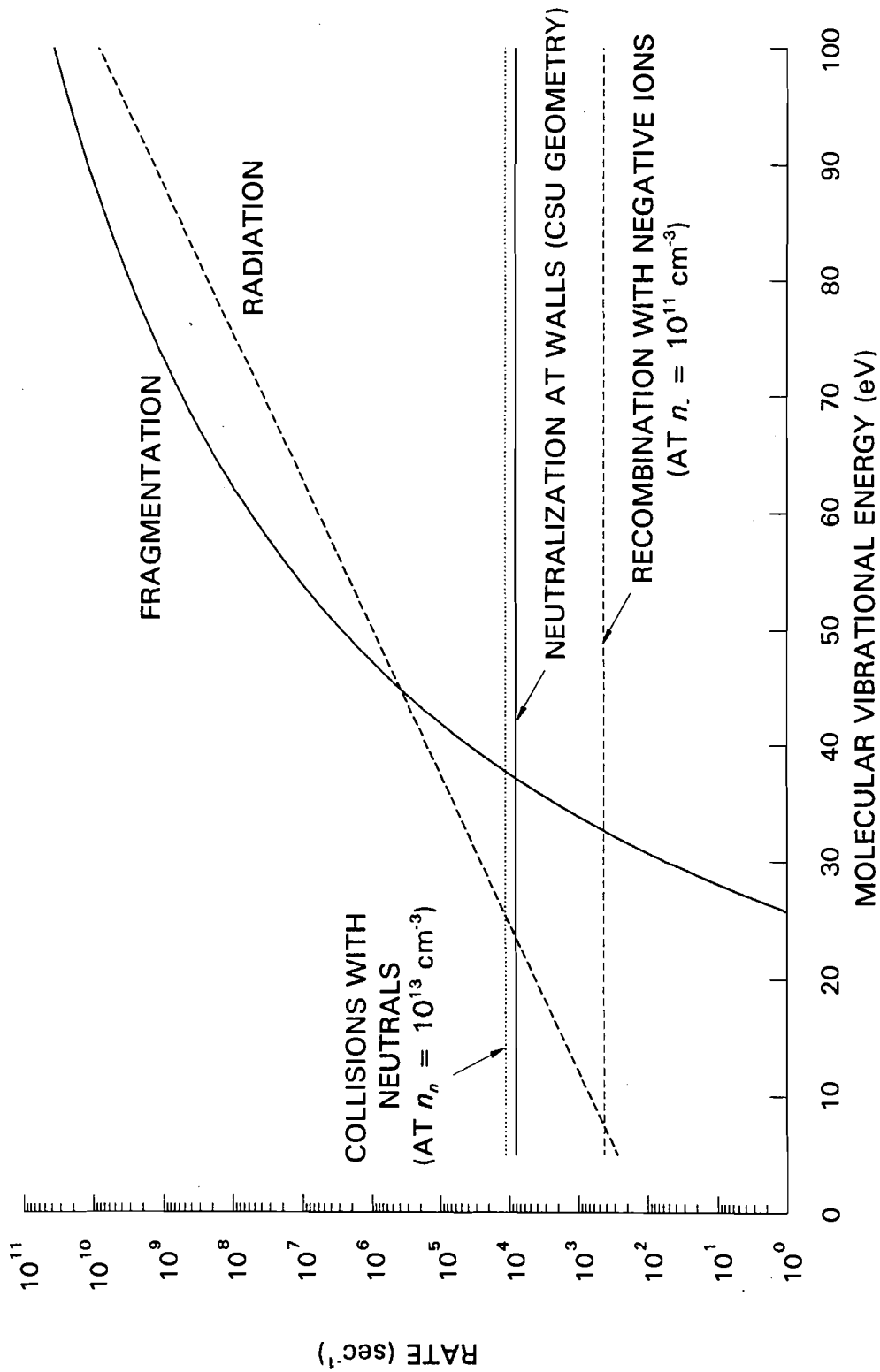


Fig. 18 Cooling Rates for Processes Affecting Vibrationally-Excited  $C_{60}^+$ .

With all of the parameters in Eq. 17 known, the equation can be re-written to solve for the distribution function for vibrationally-excited positive ions at energy level  $\varepsilon_v$ :

$$\frac{dn_+(\varepsilon_v)}{d\varepsilon_v} = \frac{n_n n_p \sigma_+(\varepsilon_v) v_p D(\varepsilon_p, \varepsilon_{ex}) + \frac{dn_+(\varepsilon'_v)}{d\varepsilon_v} k_{rad}(\varepsilon'_v) + \frac{dn_+(\varepsilon''_v)}{d\varepsilon_v} k_{colls}}{k_{frag}(\varepsilon_v) + k_{rad}(\varepsilon_v) + k_{colls} + k_{rec} + v_{+s} \frac{A_w}{V}} \quad (24)$$

The calculation of the distribution function over all vibrational energies is simplified if the computations are performed beginning with the maximum vibrational energy level ( $\varepsilon_v = \varepsilon_{ih} + \varepsilon_p - \varepsilon_{IP}$ ), and proceeding to lower vibrational energy levels. At the maximum  $\varepsilon_v$  the production of vibrationally-excited ions is only due to ionization, and at lower  $\varepsilon_v$  where there is collisional and radiative population from the upper  $\varepsilon_v$  levels, those rates will have already been determined from previous computations. Thus, all of the computations are explicit. The total volumetric fragmentation rate is obtained through integration:

$$\text{Total Volumetric Fragmentation Rate} = \int_0^{\varepsilon_{ih} + \varepsilon_p - \varepsilon_{IP}} \frac{dn_+(\varepsilon_v)}{d\varepsilon_v} k_{frag}(\varepsilon_v) d\varepsilon_v \quad (25)$$

Examples of fragmentation rate distribution functions (i.e. the integrand of Eq. 25) for vibrationally-excited positive ions calculated with Eq. 24 are shown in Fig. 19 for primary electron energies of 40 and 45 eV and typical neutral and primary electron densities. Integration of the distribution functions in the figure yields the fragmentation rate for the conditions indicated. Although the model has been specifically developed for primary electrons, it can be easily modified to account for a Maxwellian electron distribution. Additionally, a similar set of rate equations can be developed to determine the distribution function for negative ions using the data for  $C_{60}^-$  found in Ref. 49.

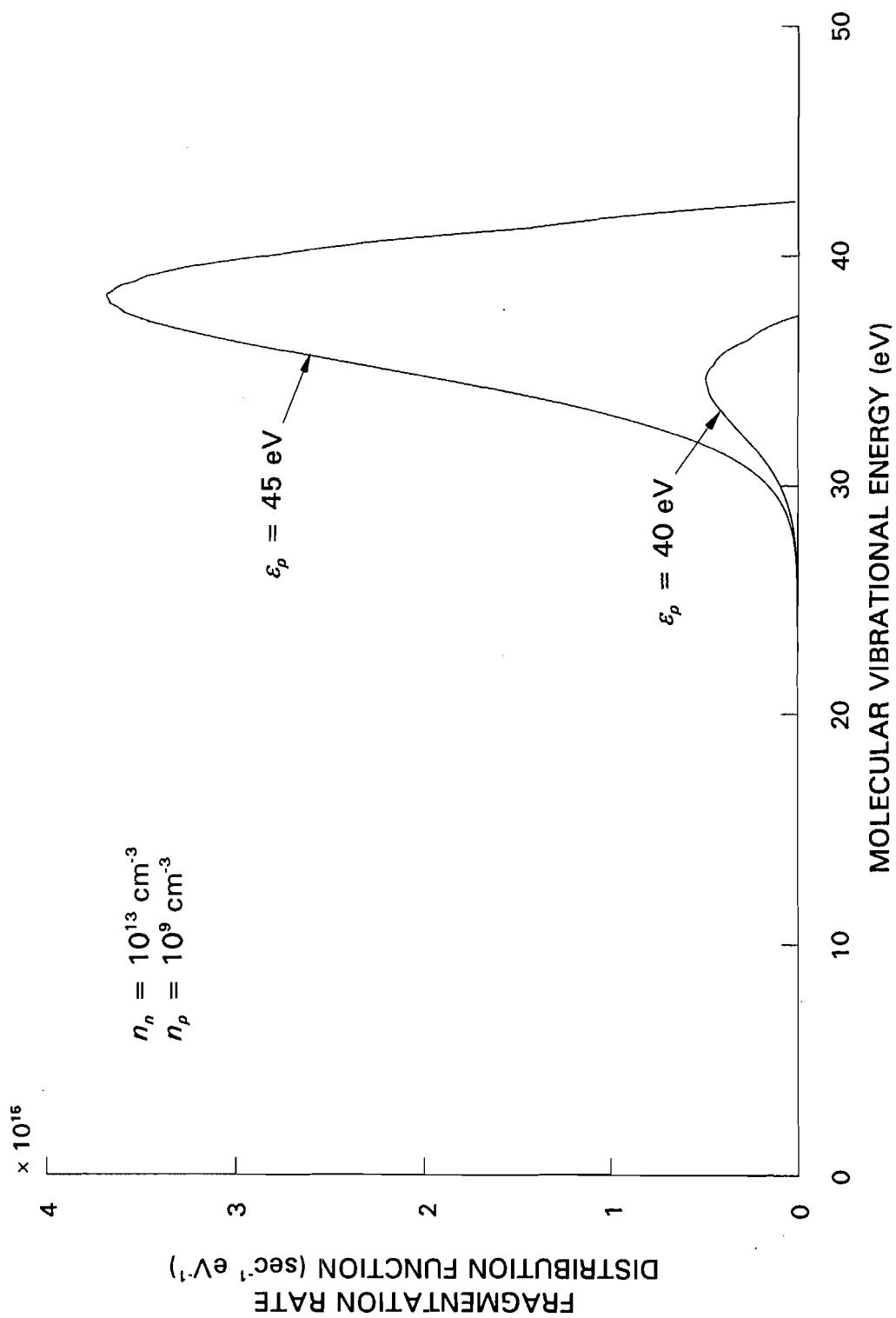


Fig. 19 Calculated Fragmentation Rate Distribution Functions for  $C_{60}^+$ .

The model was also extended to calculate the total equilibrium density of  $C_{58}$  positive ions and neutrals in the discharge chamber. The  $C_{58}$  positive ions were assumed to be created by fragmentation of  $C_{60}^+$  and by electron-impact ionization of  $C_{58}$  neutrals, and were allowed to cool through fragmentation to form  $C_{56}^+$ , radiation, collisions with neutrals, and neutralization at wall surfaces (which produced the  $C_{58}$  neutrals). In order to perform an analysis of the  $C_{58}$  species, it was necessary to make certain assumptions because of the lack of published data on the molecule. Where actual data were unavailable, it was assumed that the properties of  $C_{58}$  were the same as those for  $C_{60}$ , e.g. the ionization cross section, ion-neutral collision cross section, radiative properties, and the relationship between vibrational temperature and energy. The activation energy for the fragmentation of  $C_{58}^+$  to form  $C_{56}^+$  is known (6.78 eV [40]) and was used in the model.

The required inputs for the model calculations are the densities of primary electrons, neutral molecules, and negative ions, the primary electron energy, and the thruster geometry (wall surface area, chamber volume, and grid geometry). In order to calculate fragmentation due to Maxwellian electrons, the electron temperature and density are required. The model will calculate the distribution functions for vibrationally-excited ions, the total fragmentation rate in the discharge chamber, and the  $C_{58}^+$ -to- $C_{60}^+$  density ratio in the discharge chamber.

The model can also be used to calculate the  $C_{60}^+$  density in the discharge chamber, and experimental Langmuir probe data were used to check the model calculations. The agreement was typically very good, as evidenced by model calculations performed for the  $C_{60}$  plasma parameters given in Table 4. The measured positive ion density was

$3.4 \times 10^{11} \text{ cm}^{-3}$ , and the positive ion density calculated by the model given the required input parameters was  $6.1 \times 10^{11} \text{ cm}^{-3}$ .

## 2. Results and Comparison to Experiment

Fragmentation rates computed with the model were compared to experiment using rough estimations of the experimental fragmentation rates. Fragmentation rate means, for the purposes of this discussion, the specific reaction  $\text{C}_{60}^+ \rightarrow \text{C}_{58}^+ + \text{C}_2$ . Assuming that the total mass of a  $\text{C}_{60}$  molecule which fragmented condensed on the inside surfaces of the chamber, and assuming that the accumulation rate on the walls was indicative of the accumulation rate for all interior thruster surfaces, a rough estimate of the total number of molecules which fragmented could be determined. This number divided by the duration of the experiment then gave the fragmentation rate. For example, in one ten-minute experiment it was found that 38.1 mg of residue accumulated on the discharge chamber walls, and this corresponds to a fragmentation rate of  $9.0 \times 10^{16} \text{ sec}^{-1}$ .

Complicating the comparison between model and experiment is the fact that the hot filament in the discharge chamber can induce fragmentation and mass accumulation on the chamber walls in addition to plasma processes. It is necessary to separate filament-induced fragmentation from plasma-induced fragmentation calculated with the model for meaningful comparisons. Investigation has shown that the measured fragmentation rate (i.e. that calculated from mass deposition on the walls) due to the filament corresponds to the arrival rate of neutral molecules on the filament surface ( $\frac{1}{4} n_n v_n A_{fil}$ ) to within a factor of two. Hence, it appears that every  $\text{C}_{60}$  molecule that impinges on the filament acquires enough energy to fragment immediately.

Detailed comparisons of fragmentation induced by the filament and the plasma were conducted with the DC thruster, which was equipped with only a single cathode filament instead of the usual two filaments. Three experiments were performed with the same filament and  $C_{60}$  flow rate over the same length of time, so the only difference between experiments was the discharge voltage which was 0 V (i.e. no plasma), 45 V, and 60 V, respectively, for the three tests. Langmuir probe measurements were made in the discharges to determine the primary electron energy and density so that model calculations could be performed. The results of fragmentation measurements and calculations are shown in Fig. 20 as a function of the primary electron energy. The open circles represent measurements of the fragmentation rate based on chamber residue, the dashed line is calculated fragmentation rates from neutral arrival on the filament, and the solid line without symbols indicates model calculations based on probe measurements *added to* the filament fragmentation. With no plasma present, the measured fragmentation is within a factor of two of the expected filament-induced fragmentation. At a discharge voltage of 45 V ( $\epsilon_p = 42$  eV) the measured fragmentation nearly doubled while only a slight increase was predicted by the model for primary-electron fragmentation. At 60 V ( $\epsilon_p = 55$  eV) the model predicted a fragmentation rate closer to that measured experimentally. It is apparent that the model does not accurately predict the fragmentation at moderate electron energies and that the agreement is much better at  $\epsilon_p = 55$  eV. Most importantly, however, the trends of the measured and calculated fragmentation rate with energy do not appear to agree.

Fragmentation in the RF  $C_{60}$  discharges with the hot filament was also investigated. The measured fragmentation rates were near  $10^{17}$  sec<sup>-1</sup>, and calculation of

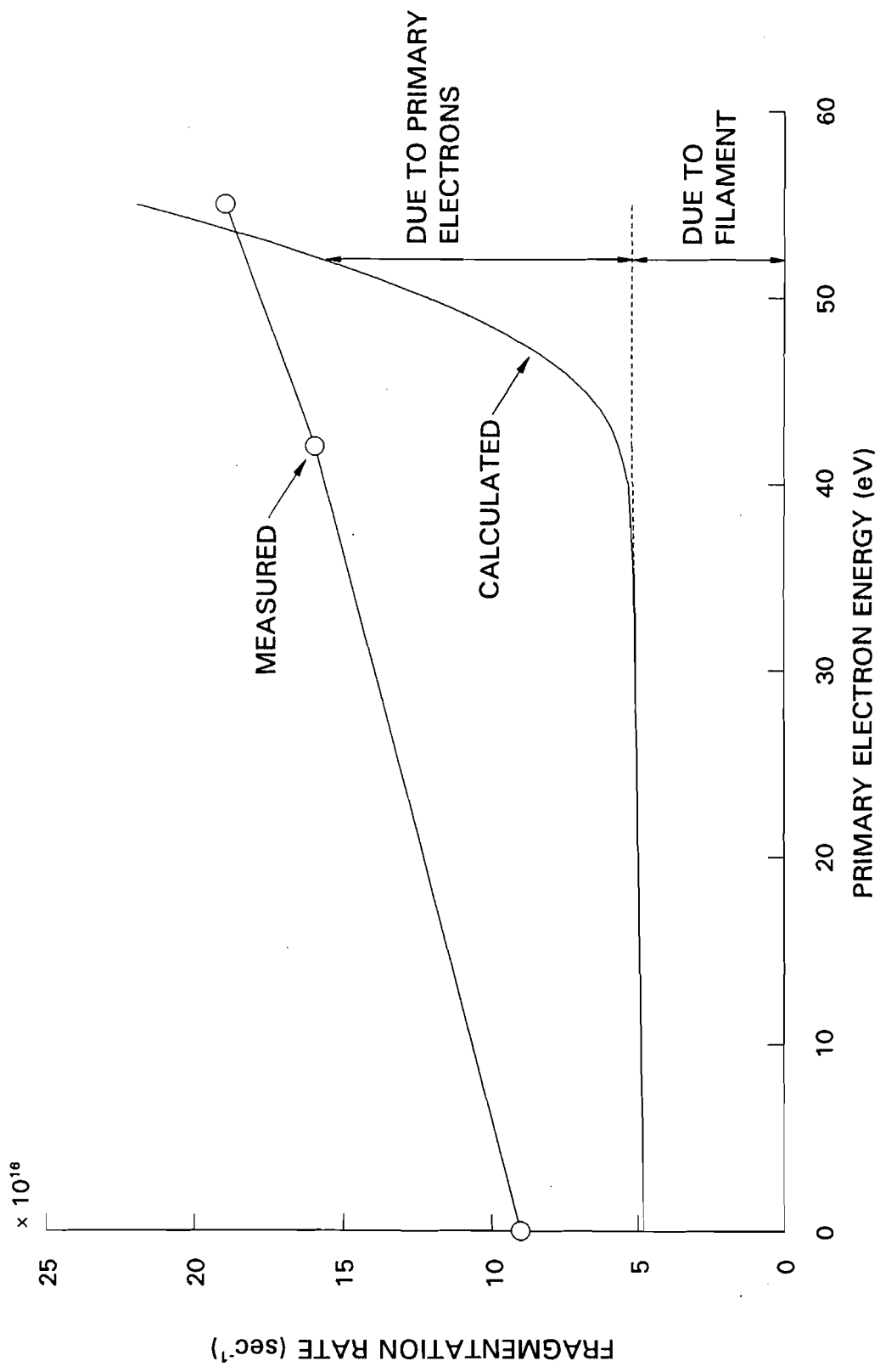


Fig. 20 Comparison of Measured and Calculated Fragmentation Rates in a DC Discharge.

the arrival rate of neutrals on the filament surface yielded a fragmentation rate that was also  $10^{17} \text{ sec}^{-1}$ . The Langmuir probe measurements of plasma parameters in the discharge ( $n_e = 3 \times 10^8 \text{ cm}^{-3}$ ,  $n_n = 2 \times 10^{13} \text{ cm}^{-3}$ , and  $T_e = 4 \text{ eV}$ ) were then used with the model to calculate a fragmentation rate of  $4 \times 10^{12} \text{ sec}^{-1}$ . Since this is so much lower than the measured fragmentation rates, it is obvious that the vast majority of fragmentation is due to the filament in RF  $\text{C}_{60}$  plasmas.

Fragmentation was also studied in an argon RF discharge seeded with  $\text{C}_{60}$  where the hot filament was unnecessary. Up to 2 mA eq. of  $\text{C}_{60}$  flow was introduced into a discharge of 200 W RF power and 200 mA eq. argon flow, and carbonaceous residue accumulated on the chamber walls during this test at an estimated fragmentation rate near  $10^{16} \text{ sec}^{-1}$ . The actual electron temperature and density in the Ar/ $\text{C}_{60}$  plasma was unknown, but probe measurements made in the pure argon discharge gave plasma parameters  $T_e = 13 \text{ eV}$  and  $n_e = 10^{11} \text{ cm}^{-3}$ . It is known, however, that the addition of a small amount of an electronegative gas such as  $\text{C}_{60}$  to a plasma can cause significant decreases in the electron density with only a modest effect on the electron temperature [50], hence a reasonable assumption for the model input parameters are a temperature of 13 eV and a density of  $10^{10} \text{ cm}^{-3}$ . Using these values and the  $\text{C}_{60}$  neutral density in the model yielded a fragmentation rate of  $2 \times 10^{16} \text{ sec}^{-1}$  which, while sensitive to the assumption of plasma parameters, is still in reasonable agreement with the rate determined from the mass measurements ( $10^{16} \text{ sec}^{-1}$ ). Fragmentation in this experiment could only be caused by plasma processes, and, given the rough assumptions, these results indicate that the model can predict the experimentally observed fragmentation in RF discharges to within an order of magnitude.

Fragmentation rates of  $10^{16}$ - $10^{17}$   $\text{sec}^{-1}$  have been measured and calculated in this study. The effects of this rate of fragmentation on actual ion thruster operation could be severe. If it is assumed that all fragments are deposited on the discharge chamber wall surfaces instead of being extracted, the fragmentation rates correspond to an accumulation rate of residue on discharge chamber surfaces of 1-10 grams per day of operation. This significant residue accumulation could short-circuit the anode or cathode of a DC discharge or the acceleration grid optics, and it could reduce the efficiency of RF energy deposition in the plasma in an RF thruster. In order to avoid these possible problems the fragmentation rates must be reduced as much as possible below those measured here. The results of the kinetic model have shown that the total fragmentation rate can be reduced by decreasing the primary electron energy (or Maxwellian electron temperature), electron density, or neutral density.

One of the major concerns for  $C_{60}$  ion thruster operation is the composition of the extracted beam, i.e. the relative amounts of  $C_{60}^+$ ,  $C_{58}^+$ , and other fragment ions. The relative populations of the fragments in the extracted ion beam will be approximately the same as in the discharge chamber, with a slight difference existing because of the dependence of the Bohm velocity on the ion mass. The kinetic model was used to predict the densities of  $C_{58}$  and  $C_{60}$  ions in a DC discharge and to determine how the ratio of the ion densities depended on the  $C_{60}$  neutral density and primary electron energy and density. The results are shown in Fig. 21 as the  $C_{58}^+$ -to- $C_{60}^+$  density ratio as a function of primary electron energy for typical neutral and primary electron densities. It can be seen in the figure that an order-of-magnitude decrease in the neutral density causes an increase in the fragment density ratio of ~100% at a primary electron energy of 30 eV and ~40% at an

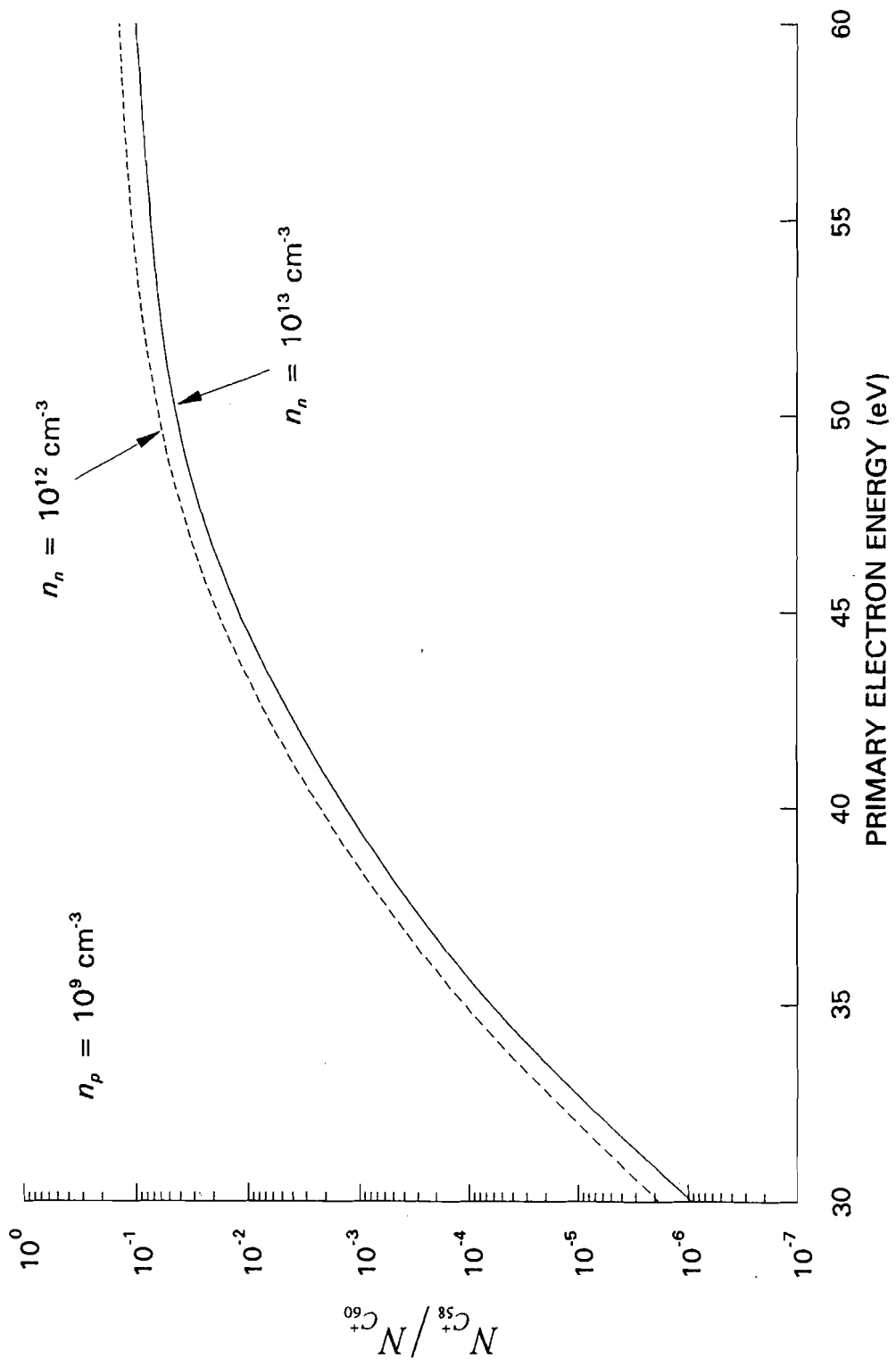


Fig. 21 Variation of Calculated Fragment Ion Density Ratio with Primary Electron Energy.

energy of 60 eV. Additionally, the ratio increases dramatically with primary electron energy, reaching about 10% at 60 eV. Note that increasing the energy from 55 to 60 eV causes fragmentation to increase by ~20%. The fragment density ratio is much less sensitive to the primary electron density; an order-of-magnitude decrease in the density causes decreases in the fragment density ratio of only 15-25%. The model then suggests that at moderate electron energies the most critical parameter for fragmentation is the primary electron energy.

Fragment density ratios were also computed for fragmentation due to Maxwellian electrons. The results are shown in Fig. 22 as a function of electron temperature for typical neutral and primary electron densities. The fragment density ratio is seen to have a strong dependence on temperature, reaching a value of 1% near 10 eV. Order-of-magnitude changes in neutral and primary electron density had very small effects on the ratio (less than 20%) which would be difficult to discern on the semi-log plot. The trends in these changes, though, were the same as in Fig. 21 (e.g. a decrease in neutral density caused an increase in the fragment density ratio).

### 3. Comparison to $\mathbf{E} \times \mathbf{B}$ Probe Data

Model calculations of fragmentation produced by primary electrons were next compared to the  $\mathbf{E} \times \mathbf{B}$  probe data acquired from the DC thruster at JPL. Langmuir probe measurements were not made during those experiments, so the parameters required for model calculations were deduced from the experimental data that were provided by JPL. The thruster neutral density was easily calculated from the  $C_{60}$  flow rate and thruster geometry, and the primary electron energy was assumed to be equal to the discharge voltage. Finally, the primary electron density was estimated from the beam current data

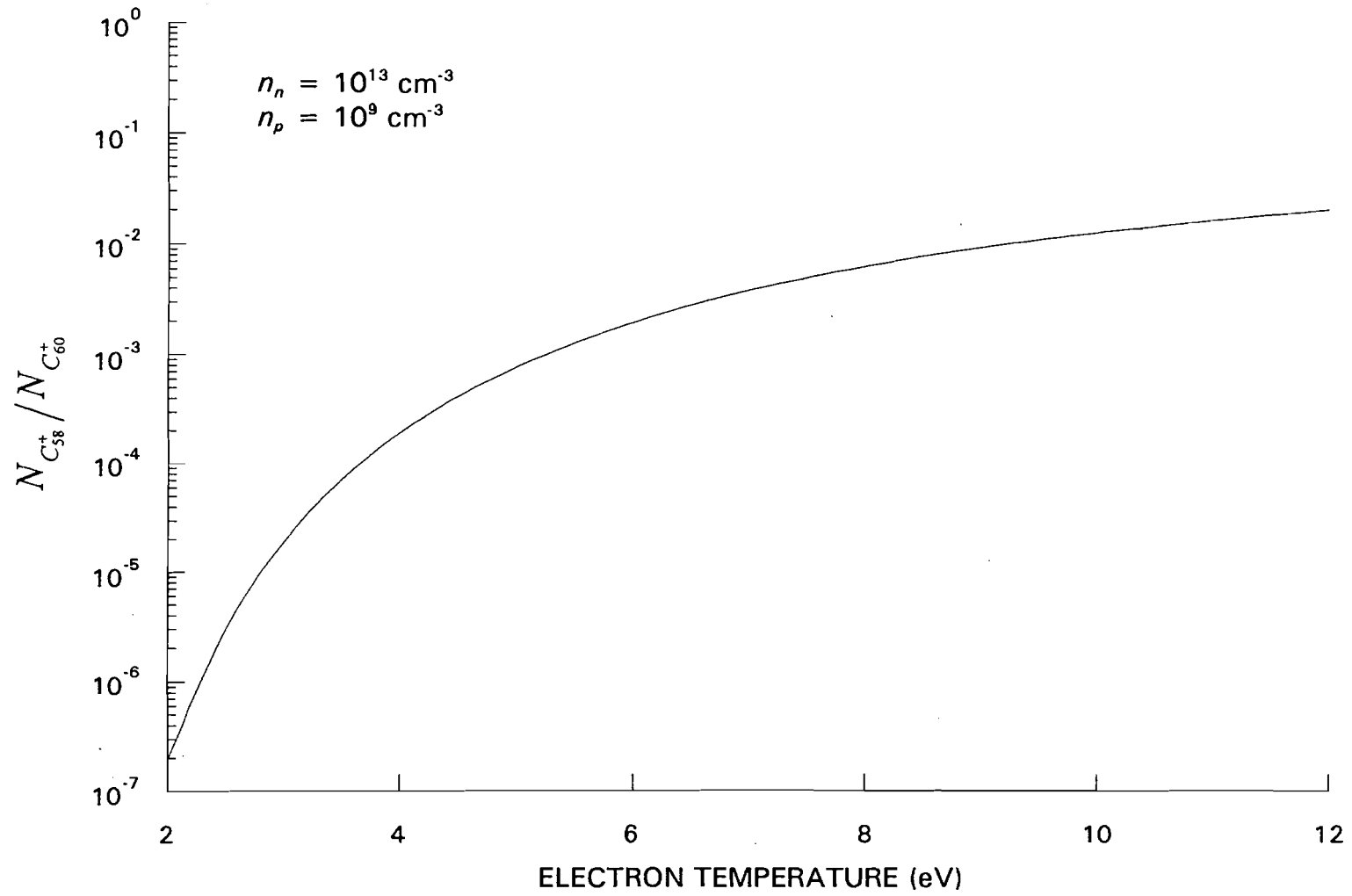


Fig. 22 Variation of Calculated Fragment Ion Density Ratio with Electron Temperature.

using the following procedure. It was assumed that the negative ion density in the thruster was large so that the beam current could be described by Eq. 6, and the positive ion density was calculated using that equation. The kinetic model has been shown to predict the positive ion density in the experiments conducted in this study fairly well, so a primary electron density was chosen for the JPL thruster such that the model calculated the positive ion density deduced from Eq. 6. This does not, however, ensure a false agreement between model and experiment. If the primary electron density in the JPL thruster is estimated by assuming the same ratio of primary-electron to positive-ion density as in Table 4, the final results would differ by only 10-20%. With the necessary plasma properties at hand, the ratio of  $C_{58}^+$  to  $C_{60}^+$  in the discharge chamber could be calculated with the model. The experimentally observed ratio was determined directly from the  $\mathbf{E} \times \mathbf{B}$  data.

The  $\mathbf{E} \times \mathbf{B}$  probe data and the model calculations based on the experimental data are plotted in Fig. 23 as a function of discharge voltage, because the model results suggest that the fragment density ratio is most sensitive to the primary electron energy, which was determined directly from the discharge voltage. The error bars on the experimental data were determined using the bracketing procedure of Ref. 24. At discharge voltages greater than about 55 eV the model yields results that lie within the error bars associated with about half of the data points, so they seem reasonable. At the lower voltages the model predictions appear to be less accurate, but there is also a greater spread in the experimental data. Additionally, filament-induced fragmentation was not incorporated into the model calculations and it is known from Fig. 20 that the relative importance of filament-induced fragmentation becomes greater at lower primary electron energies.

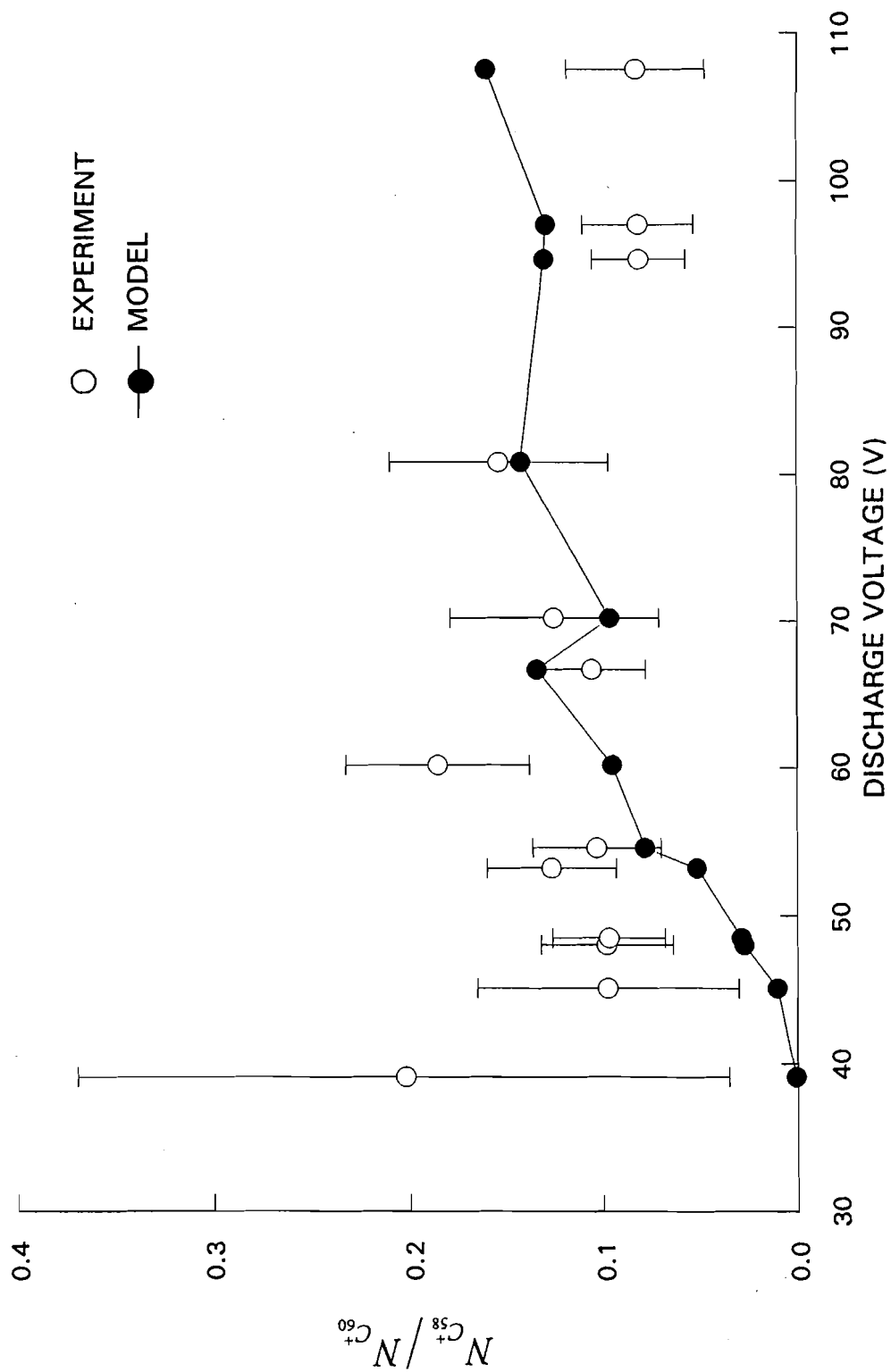


Fig. 23 Comparison of Experimental ExB Probe Data and Model Calculations.

Given all of the assumptions that have been made in the modeling and the deduction of plasma parameters from experimental data, the agreement between experiment and model in Fig. 23 is considered fairly good. The model does not, however, completely predict fragmentation behavior. Consider, for example, the  $\mathbf{E} \times \mathbf{B}$  data of Fig. 16 which correspond to the experimental point in Fig. 23 at a discharge voltage of 39 V. It is clear that this operating condition yields extensive fragmentation in the discharge chamber, but the model predicts that there should be very little fragmentation. The reason for this discrepancy is unknown, but may be related to the discrepancy observed in the experimental results depicted in Fig. 20.

In spite of some of the differences between experimental data and model calculations, it appears that the essential kinetic processes for  $C_{60}$  fragmentation are included in the model. This suggests that fragmentation is caused by pumping energy into  $C_{60}$  vibrational modes through a single electron impact. The experimental data could probably be more accurately described with a model that includes electron-impact excitation and multiple electron impacts, although the data required to include these effects are not readily available yet. A more detailed accounting of cluster vibrational energy changes during collisions with walls and other particles might also yield more accurate results.

## V. PROSPECTS AND RECOMMENDATIONS FOR FUTURE RESEARCH

The research in this study has shown that the use of  $C_{60}$  propellant in conventional RF and DC ion thrusters is limited by molecular fragmentation and negative ion formation. Fragmentation occurs when the  $C_{60}$  molecule either lands on a surface which is at a high temperature (greater than about 1200 K) or when its vibrational energy is increased to a critical level through kinetic processes in a plasma discharge, whereby it may undergo unimolecular dissociation. A large negative ion concentration can significantly limit the beam current which may be extracted from a thruster because of a large reduction of the Bohm velocity.

The inductively-coupled RF source was initially investigated because it does not require a hot electron source on which  $C_{60}$  would dissociate, but a discharge could not be sustained on pure  $C_{60}$  without a hot-filament cathode that would supply electrons to satisfy the demand for electrons to form negative ions. Direct-current discharges in  $C_{60}$  were relatively easy to establish and maintain compared to the RF discharges, but they suffered from the same fragmentation and negative ion concentration problems as the RF source. Fragmentation was actually worse in the DC discharges because of the high-energy primary electron group which pumped energy into  $C_{60}$  vibrational modes and drove the unimolecular dissociation.

There are mechanisms other than RF or DC for sustaining plasma discharges for ion thrusters which might suffer less from  $C_{60}$  fragmentation and negative ion production. These include electron cyclotron resonance (ECR) and helicon (i.e. whistler wave) plasma sources. Both of these are attractive because they are driven by electromagnetic waves

and thus do not require hot cathodes for operation. Published literature has been reviewed for the ECR and helicon sources and their feasibility for  $C_{60}$  ion thrusters has been investigated based on the results of this study.

#### A. ECR Ion Source

An electron cyclotron resonance condition is created in an ECR discharge with the launch of right-hand circularly polarized microwaves into a chamber with a static magnetic field. The magnetic field strength is chosen such that the electron cyclotron frequency matches the microwave frequency (e.g. an 875 Gauss magnetic field with a 2.45 GHz microwave frequency). An electron in the resonance zone thus sees a steady azimuthal electric field and is continuously accelerated. This is in contrast to the inductively-coupled RF source in which the azimuthal electric fields are time-varying and thus alternately accelerate and decelerate free electrons. Experimental measurements in ECR discharges show that the ECR resonance zone has a roughly toroidal shape and its location depends on the microwave frequency, magnetic field, and geometry of the discharge chamber. For the inert gases which are typically used, the electron population is usually near-Maxwellian with temperatures of a few eV in the bulk plasma and  $\sim 10$  eV or more in the resonance zone, and typical electron densities are in the range of  $10^{10}$ - $10^{12}$   $\text{cm}^{-3}$  [51,52].

A 10-GHz ECR ion source has been used to produce a  $C_{60}$  plasma and ion beam in a study of  $C_{60}$  ionization and fragmentation [53]. Mass spectrometry of the extracted beam clearly showed fragmentation of the  $C_{60}$  ions (the  $C_{58}^+$  signal strength was 14% of the  $C_{60}^+$  signal strength) as well as doubly-charged  $C_{60}$  and fragments. The fragmentation patterns observed in the ECR experiment were very similar to those observed in an experiment in which fullerene ions were produced by laser-desorption, a process which is known to create ions with large internal energies [54]. Thus, at least under the operating

conditions in the experiment described here, it is known that C<sub>60</sub> fragmentation can be induced in ECR sources.

In order to determine if an ECR source might be acceptable for a C<sub>60</sub> ion thruster, the kinetic model was applied using conditions that might be expected in an ECR source. Nishayama *et al.* [52] performed extensive plasma diagnostics in an argon ECR thruster and their results were used as a reference for the model calculations. It was assumed that the electron temperatures for C<sub>60</sub> would be similar to those measured in argon, and that the electron densities would likely be an order of magnitude or more smaller due to negative ion formation. Under these circumstances, fragmentation will be caused almost exclusively by the ~10-12 eV Maxwellian electrons in the resonance zone because the ~3 eV electrons in the bulk plasma do not have sufficient energy to induce significant fragmentation (see Fig. 22). Vibrational quenching of the excited molecules will be dominant as soon as they escape from the resonance zone into the bulk plasma. Ionization of C<sub>60</sub> will be effective throughout the whole discharge chamber, including the electrons in the bulk plasma.

The kinetic model was used to estimate the C<sub>58</sub><sup>+</sup>-to-C<sub>60</sub><sup>+</sup> ratio in the discharge chamber for electron temperatures of 10-12 eV (in the resonance zone only), electron densities of 10<sup>9</sup>-10<sup>10</sup> cm<sup>-3</sup>, and neutral densities of 10<sup>12</sup>-10<sup>13</sup> cm<sup>-3</sup>. The model calculations predict that the fragment ratio would be about 1-2% over the variety of conditions tested. This value is lower than seen in the C<sub>60</sub> ECR ion source [53] and the JPL DC thruster **E×B** probe measurements, and may be an acceptable fragmentation level for many purposes. The calculated fragmentation rates for the ECR thruster, however, were 10<sup>15</sup>-10<sup>16</sup> sec<sup>-1</sup> and these rates would yield, if all fragments were deposited on the discharge chamber wall surfaces instead of being extracted, an accumulation rate of residue on the walls of up to a gram per day of operation. As discussed earlier, this could have severe effects for ion thruster operation.

## B. Helicon Ion Source

Helicon ion sources are driven by helicon waves, which belong to the whistler wave family, and can produce very high plasma densities with ionization levels approaching 100%. One reason for the large ionization efficiency is that a helicon source can be designed to accelerate electrons directly through the helicon wave [55], thereby producing a high-energy electron group with a desired energy, e.g. 70 eV, which is the peak of the  $C_{60}$  positive-ionization cross section [6]. Helicon sources have been reviewed by Chen [55]. In addition to the high-energy primary electron group, a background Maxwellian group exists as in a DC source. For example, one particular helicon source operated on argon produced electron temperatures of about 5 eV and densities of  $\sim 10^{11}$ - $10^{12}$   $cm^{-3}$  [56]. Electron temperatures of 2-7 eV were measured in an  $SF_6$  discharge, although the densities were not reported [57]. Electron densities greater than  $10^{13}$   $cm^{-3}$  are not uncommon [58]. These studies do not report the relative densities of the Maxwellian and primary electrons.

A helicon ion source may be effective for a  $C_{60}$  thruster, although much more research needs to be done to make a determination. First, no hot electron source is necessary for helicon operation, and this eliminates a known fragmentation mechanism in DC thrusters. Second, the primary electron energy can be chosen through design to minimize fragmentation. Recall that the kinetic model in Chapter IV suggests that fragmentation drops sharply with primary electron energy. For example, if a helicon discharge is designed to produce a primary electron energy of 20 eV, and the primary electron density and  $C_{60}$  neutral density are  $10^{11}$   $cm^{-3}$  and  $10^{13}$   $cm^{-3}$ , respectively, the model predicts a  $C_{58}^+$ -to- $C_{60}^+$  density ratio of  $\sim 10^{-10}$ . The model indicates, then, that fragmentation could be controllable in a helicon thruster, although this is not necessarily supported by the JPL  $E \times B$  data at low primary electron energies. The negative ion density, however, will probably be large if the Maxwellian electron density is more than a

small fraction of the primary electron density and the electron temperature is a few eV, and will limit the Bohm velocity and thus beam extraction. Since helicon ion sources are a relatively recent development and have not yet been applied to ion thrusters, it is difficult to anticipate whether a  $C_{60}$  helicon thruster would be viable.

### C. Recommendations

The results contained in this study suggest some possibilities for future research that may provide further insight to the operation of  $C_{60}$  ion thrusters. The most obvious of those is that a systematic study of the effects of operating conditions on DC thruster performance could be conducted. For example, certain operating conditions or thruster designs may minimize the negative ion densities which can limit performance.

Additionally, there appear to be three particular parameters that influence fragmentation: discharge voltage, discharge current, and neutral density. The effects of each could be studied and quantified with a series of  $E \times B$  probe measurements, and it may be possible to reduce fragmentation to acceptable levels through proper design and choice of operating conditions. Fragmentation due to a hot-filament cathode or hollow cathode could be eliminated by using a cold field-emission cathode, which is also worth investigation. The fragmentation modeling discussed in Chapter IV could be expanded to include more plasma phenomena such as multiple electron impacts with molecules and non-ionizing impacts. The accuracy of the model will increase as more research is performed on the fundamental properties of fullerenes, i.e. electron excitation cross section, electron energy deposition function, and fragmentation phenomena.

Two alternative ion sources to the RF and DC types have been discussed in light of the current research results. An ECR thruster could be built and tested, as could a helicon thruster. Other ion sources not evaluated here could be a possibility. Based on the results presented in this study, an “ideal” electron population can be surmised. It should consist

of a relatively large density of primary electrons with an energy of 20-30 eV, which is large enough for substantial ionization but small enough to avoid significant fragmentation. It should also have no more than a very small population of very low temperature Maxwellian electrons (much less than 1 eV) in order to limit the negative ion density (see discussion of Fig. 12). If such a source can even be designed, it may be too complicated for ion thruster use. Unfortunately, it is also likely that such a source would have a large beam-ion energy cost, and thus electrical efficiency, and negate the advantageous properties of C<sub>60</sub> propellant.

Finally, other members of the fullerene family could be investigated for use as propellant. The first obvious member for study is C<sub>70</sub>, but its cross section for negative ion formation is also large [9] and thus it may prove unfeasible. Larger fullerenes exist [59], although they are not easily produced and the properties relevant for ion thruster research are largely unknown as of yet. A fullerene with sufficient mass, even if it has a large cross section for negative ion formation, could still provide thruster electrical efficiencies in excess of those for conventional xenon thrusters. Other properties of the large fullerenes such as vapor pressure, fragmentation behavior, and cost, however, may preclude their use.

## VI. CONCLUSIONS

The results contained in this study prove that ion thrusters can operate with  $C_{60}$  propellant, but with poor performance. The initial attempts to run the thruster with RF power failed because of negative ion production, and an electron source was found necessary to sustain an RF  $C_{60}$  plasma. It was shown that a beam of  $C_{60}$  ions could be extracted from the RF thruster with the electron source, but that the performance was significantly worse than with argon propellant. Langmuir probe measurements in the  $C_{60}$  plasma, coupled with knowledge of the physics in an electronegative plasma discharge, revealed a relatively large negative ion density which limited the rate at which positive ions could be extracted from the thruster. Calculations of beam current based on the Langmuir probe data agreed with experimentally observed beam currents to within a factor of two to three.

Unfortunately, the need for an electron source negates the potentially significant advantage of RF over DC ion sources. Therefore, a DC source was tested and the results were compared to those measured during RF thruster operation. The performance of the DC source was again poor, but better than the RF source. Langmuir probe measurements showed that the negative ion concentration was substantially less in the DC thruster than it had been in the RF thruster, but it was still sufficiently large so that the beam current that could be extracted was limited to a value substantially below those of current thrusters. The calculations and measurements of beam current for the DC thruster agreed to within 25%. It was determined that the negative ion concentrations would have to be reduced by orders of magnitude in order to realize acceptable beam currents.

In both RF and DC thrusters, fragmentation of the  $C_{60}$  molecule was significant. Fragmentation in the RF thruster was dominated by the hot-filament electron source, but fragmentation was also observed in an argon discharge seeded with  $C_{60}$  in which there was no hot filament, and this indicated that plasma processes also induced fragmentation. Filament-induced fragmentation was also important in the DC source, but it was observed that fragmentation rates could be increased by increasing the primary electron energy. It appears that an ion thruster operating on  $C_{60}$  propellant will generally suffer significant amounts of fragmentation equal to that caused by a hot filament or other type of hot electron source. The fragmentation observed in this study was described by a kinetic model that accounted for only single impacts of high-energy electrons on  $C_{60}$  molecules. The model predicted the relative densities of whole and fragmented molecules measured in an ion beam with an  $\mathbf{E} \times \mathbf{B}$  probe to within a factor of  $\sim 3$  over a range of operating conditions. The results of the experiments and modeling in this study indicate that fragmentation may be controllable through correct choices in thruster design and operating conditions.

Radio-frequency ion sources are not practical for  $C_{60}$  ion thrusters. Even if an RF source can be operated on  $C_{60}$  without a hot electron source or any electron source at all, it will inherently produce a large negative ion density because of the electron energy distributions that exist in such sources. Thus, beam currents will be severely limited. Direct-current ion sources are not promising, but with many improvements may be useful. Fragmentation due to hot surfaces and primary electrons needs to be limited or eliminated, and the negative ion densities must be decreased before this type of thruster will be practical. Current research shows that the fragmentation problem may be approachable but the negative ion problem is not. It is possible that other types of ion sources may prove useful if they can produce specific electron energy distributions that avoid fragmentation and negative ion production. Based on the results of this study, however, it appears very unlikely that  $C_{60}$  could be a suitable propellant for any type of ion thruster.

## VII. REFERENCES

1. Jahn, R. G., Physics of Electric Propulsion, McGraw-Hill, New York, 1968, Chaps. 1 and 7.
2. Leifer, S. D., Rapp, D., and W. A. Saunders, "Electrostatic propulsion using C<sub>60</sub> molecules," J. Propulsion and Power, v. 8 (6), Nov.-Dec. 1992, pp. 1297-1300.
3. Torres, E. R., Matossian, J. N., Williams, J. D., and M. Martinez-Sanchez, "Prediction of the performance of an ion thruster using Buckminsterfullerene as the propellant," AIAA 93-2494, 29<sup>th</sup> Joint Propulsion Conference, June 1993, Monterey, CA.
4. Brophy, J. R., "Ion Thruster Performance Model," NASA CR-174810, Dec. 1984.
5. Lichtenberger, D. L., Jatcko, M. E., Nebesny, K. W., Ray, C. D., Huffman, D. R., and L. D. Lamb, "The ionizations of C<sub>60</sub> in the gas phase and in thin solid films," Mat. Res. Soc. Symp. Proc., v. 206, 1991, pp. 673-678.
6. Matt, S., Dünser, B., Lezius, M., Deutsch, H., Becker, K., Stamatovic, A., Scheier, P., and T. D. Märk, "Absolute partial and total cross-section functions for the electron impact ionization of C<sub>60</sub> and C<sub>70</sub>," J. Chem. Phys., v. 105 (5), 1 Aug. 1996, pp. 1880-1896.
7. Rapp, D., and P. Englander-Golden, "Total cross sections for ionization and attachment in gases by electron impact. I. Positive ionization," J. Chem. Phys., v. 43 (5), 1 Sep. 1965, pp. 1464-1479.
8. Wang, L., Conceicao, J., Jin, C., and R. E. Smalley, "Threshold photodetachment of cold C<sub>60</sub><sup>-</sup>," Chem. Phys. Lett., v. 182 (1), 19 July 1991, pp. 5-11.
9. Jaffke, T., Illenberger, E., Lezius, M., Matejčík, Š., Smith, D., and T. D. Märk, "Formation of C<sub>60</sub><sup>-</sup> and C<sub>70</sub><sup>-</sup> by free electron capture. Activation energy and effect of the internal energy on lifetime," Chem. Phys. Lett., v. 226, 12 Aug. 1994, pp. 213-218.
10. Stetzer, M. R., Heiney, P. A., Fischer, J. E., and A. R. McGhie, "Thermal stability of solid C<sub>60</sub>," Phys. Rev. B, v. 55 (1), 1 Jan. 1997, pp. 127-131.

11. Gruen, D. M., Liu, S., Krauss, A. R., and X. Pan, "Buckyball microwave plasmas: Fragmentation and diamond-film growth," J. Appl. Phys., v. 75 (3), 1 Feb. 1994, pp. 1758-1763.
12. Wurz, P., and K. R. Lykke, "Multiple excitation, dissociation, and ionization of C<sub>60</sub>," J. Phys. Chem., v. 96 (25), 1992, pp. 10129-10139.
13. Foltin, M., Lezius, M., Scheier, P., and T. D. Märk, "On the unimolecular fragmentation of C<sub>60</sub><sup>+</sup> fullerene ions: The comparison of measured and calculated breakdown patterns," J. Chem. Phys., v. 98 (12), 15 June 1993, pp. 9624-9634.
14. Foltin, M., Echt, O., Scheier, P., Dünser, B., Wörgötter, R., Muigg, D., Matt, S., and T. D. Märk, "Dissociation of singly and multiply charged fullerenes: Emission of C<sub>4</sub>, or sequential emission of C<sub>2</sub>?" J. Chem. Phys., v. 107 (16), 22 Oct. 1997, pp. 6246-6256.
15. Gruen, D. M., "C<sub>60</sub> interactions with surfaces, gaseous species and photons: an overview," Nucl. Instr. and Meth. In Phys. Res., v. B78, 1993, pp. 118-125.
16. Mitzner, R., and E. E. B. Campbell, "Optical emission studies of laser desorbed C<sub>60</sub>," J. Chem. Phys., v. 103 (7), 15 Aug. 1995, pp. 2445-2453.
17. Christian, J. F., Wan, Z., and S. L. Anderson, "Ne<sup>+</sup> + C<sub>60</sub> collisions: The dynamics of charge and energy transfer, fragmentation, and endohedral complex formation," J. Chem. Phys., v. 99 (5), 1 Sep. 1993, pp. 3468-3479.
18. Scheier, P., Dünser, B., Wörgötter, R., Lezius, M., Robl, R., and T. D. Märk, "Appearance and ionization energies of singly, doubly and triply charged C<sub>60</sub> and its fragment ions produced by electron impact ionization," Int. J. of Mass Spec. and Ion Proc., v. 138, 1994, pp. 77-93.
19. Forst, W., Theory of Unimolecular Reactions, Academic Press, New York, 1973, Chaps. 1, 2, 8, 10.
20. Hruby, V., Monheiser, J., and J. Kolencik, "Fullerene ion thruster development," IEPC 97-074, 25<sup>th</sup> International Electric Propulsion Conference, Aug. 1997, Cleveland, OH.
21. Nakayama, Y., and H. Takegahara, "C<sub>60</sub> application to ion thruster – inspection of ionized and extracted particle," IEPC 97-076, 25<sup>th</sup> International Electric Propulsion Conference, Aug. 1997, Cleveland, OH.
22. Takegahara, H., and Y. Nakayama, "C<sub>60</sub> feasibility study on application to ion thruster," AIAA 95-2665, 31<sup>st</sup> Joint Propulsion Conference, July 1995, San Diego, CA.

23. Anderson, J. R., Fitzgerald, D., Leifer, S., and J. Mueller, "Design and testing of a fullerene RF ion engine," AIAA 95-2664, 31<sup>st</sup> Joint Propulsion Conference, July 1995, San Diego, CA.
24. Anderson, J. R., and D. Fitzgerald, "Fullerene propellant research for electric propulsion," AIAA 96-3211, 32<sup>nd</sup> Joint Propulsion Conference, July 1996, Lake Buena Vista, FL.
25. Maiken, E. B., and P. Taborek, "Ion-beam deposition of hard, amorphous carbon from a fullerene discharge," J. Appl. Phys., v. 78 (1), 1 July 1995, pp. 541-549.
26. Horak, P. D., and U. J. Gibson, "Broad fullerene-ion beam generation and bombardment effects," Appl. Phys. Lett., v. 65 (8), 22 Aug. 1994, pp. 968-970.
27. Leifer, S. D., "Characterization of fullerenes for electrostatic propulsion applications," Ph.D. dissertation, California Institute of Technology, Pasadena, CA, 1995.
28. Polk, J. E., Patterson, M. J., Brophy, J. R., Rawlin, V. K., Sovey, J. S., Myers, R. M., Blandino, J. J., Goodfellow, K. D., and C. E. Garner, "A 1000 hour wear test of the NASA NSTAR ion thruster," AIAA 96-2784, 32<sup>nd</sup> Joint Propulsion Conference, July 1996, Lake Buena Vista, FL.
29. Nakayama, Y., Sugaya, S., and H. Takegahara, "C<sub>60</sub> Application to Ion Thruster - Improvement of Plasma Production," ISTS 98-a-2-22P, 21<sup>st</sup> International Symposium on Space Technology and Science, May 1998, Sonic City, Omiya, Japan.
30. Williams, J. D., "An Experimental Investigation of Hollow Cathode-Based Plasma Contactors," NASA CR-187120, May 1991.
31. Koruga, D., Hameroff, S., Withers, J., Loutfy, R., and M. Sundareshan, Fullerene C<sub>60</sub>, North-Holland, Amsterdam, 1993, Chap. 8.
32. Starner, K. E., "Evaluation of electron quench additives in a subsonic air arc channel," AIAA Journal, v. 7 (12), Dec. 1969, pp. 2357-2358.
33. Aston, G., "The Ion-Optics of a Two-Grid Electron-Bombardment Thruster," NASA CR-135034, May 1976.
34. Amemiya, H., "Plasmas with negative ions – probe measurements and charge equilibrium," J. Phys. D: Appl. Phys., v. 23, 1990, pp. 999-1014.
35. Lieberman, M. A., and A. J. Lichtenberg, Principles of Plasma Discharges and Materials Processing, John Wiley & Sons, New York, 1994, Chaps. 3, 6, 8, 10.

36. Boyd, R. L. F., and J. B. Thompson, "The operation of Langmuir probes in electronegative plasmas," Proc. of the Royal Society of London, Series A, v. 252, 27 Oct. 1959, pp. 102-119.
37. Strickfaden, W. B., and K. L. Geiler, "Probe measurements of the discharge in an operating electron bombardment engine," AIAA Journal, v. 1 (8), Aug. 1963, pp. 1815-1823.
38. Kolodney, E., Tsipinyuk, B., and A. Budrevich, "The thermal energy dependence (10-20 eV) of electron impact induced fragmentation of C<sub>60</sub> in molecular beams: Experiment and model calculations," J. Chem. Phys., v. 102 (23), 15 June 1995, pp. 9263-9275.
39. Vincenti, W. G., and C. H. Kruger, Jr., Introduction to Physical Gas Dynamics, John Wiley & Sons, New York, 1965, Chap 7.
40. Wörgötter, R., Dünser, B., Scheier, P., Märk, T. D., Foltin, M., Klots, C. E., Laskin, J., and C. Lifshitz, "Self-consistent determination of fullerene binding energies BE (C<sub>n</sub><sup>+</sup> - C<sub>2</sub>), n = 58, ..., 44," J. Chem. Phys., v. 104 (4), 22 Jan. 1996, pp. 1225-1231.
41. Matt, S., Echt, O., Wörgötter, R., Scheier, P., Klots, C. E., and T. D. Märk, "Relative dissociation energies of singly and doubly charged fullerene ions, C<sub>n</sub><sup>z+</sup>, for n = 52 to 70," Int. J. of Mass Spec. and Ion Proc., v. 167/168, 1997, pp. 753-759.
42. Laskin, J., and C. Lifshitz, "Time-resolved metastable fractions of fullerenes," Chem. Phys. Lett., v. 277, 17 Oct. 1997, pp. 564-570.
43. Smirnov, B. M., Negative Ions, McGraw-Hill, New York, 1982, Chap. 2, Sect. 2.
44. Cioslowski, J., Electronic Structure Calculations on Fullerenes and Their Derivatives, Oxford University Press, New York, 1995, Chap. 3.
45. Pilling, M. J., and P. W. Seakins, Reaction Kinetics, Oxford University Press, Oxford, 1995, Chap. 5.
46. Callear, A. B., "Basic RRKM Theory," appears in Modern Methods in Kinetics, ed. by C. H. Bamford and C. F. H. Tipper, Elsevier Scientific Publishing Company, Amsterdam, 1983.
47. Massey, H. S. W., and E. H. S. Burhop, Electronic and Ionic Impact Phenomena, Oxford University Press, London, 1956, Chap. 7, Sect. 12.
48. Stanton, R. E., and M. D. Newton, "Normal vibrational modes of Buckminsterfullerene," J. Phys. Chem., v. 92 (8), 1988, pp. 2141-2145.

49. Matejčík, Š., Märk, T. D., Španěl, P., Smith, D., Jaffke, T., and E. Illenberger, "Formation and decay of  $C_{60}^-$  following free electron capture by  $C_{60}$ ," J. Chem. Phys., v. 102 (6), 8 Feb. 1995, pp. 2516-2521.
50. Strele, D., Winkler, C., Krumm, P., and R. Schrittwieser, "A simple source for a  $C_{60}$  plasma," Plasma Sources Sci. Technol., v. 5, 1996, pp. 603-606.
51. Weng, Y., and M. J. Kushner, "Electron energy distributions in electron cyclotron resonance discharges for material s processing," J. Appl. Phys., v. 72 (1), 1 July 1992, pp. 33-42.
52. Nishiyama, K., Satori, S., Kuninaka, H., Kuriki, K., and Y. Arakawa, "Plasma diagnostics inside a microwave discharge ion thruster," IEPC 97-061, 25<sup>th</sup> International Electric Propulsion Conference, Aug. 1997, Cleveland, OH.
53. Völpel, R., Hofmann, G., Steidl, M., Stenke, M., Schlapp, M., Trassl, R., and E. Salzborn, "Ionization and fragmentation of fullerene ions by electron impact," Phys. Rev. Lett., v. 71 (21), 22 Nov. 1993, pp. 3439-3441.
54. Ehlich, R., Westerburg, M., and E. E. B. Campbell, "Fragmentation of fullerenes in collisions with atomic and molecular targets," J. Chem. Phys., v. 104 (5), 1 Feb. 1996, pp. 1900-1911.
55. Chen, F. F., "Plasma ionization by helicon waves," Plasma Physics and Controlled Fusion, v. 33 (4), 1991, pp. 339-364.
56. Boswell, R. W., and R. K. Porteous, "Large volume, high density rf inductively coupled plasma," Appl. Phys. Lett., v. 50 (17), 27 Apr. 1987, pp. 1130-1132.
57. Chabert, P., Boswell, R. W., and C. Davis, "Investigation of a  $SF_6$  helicon plasma," J. Vac. Sci. Technol. A, v. 16 (1), Jan./Feb. 1998, pp. 78-86.
58. Chen, F. F., "Experiments on helicon plasma sources," J. Vac. Sci. Technol. A, v. 10 (4), July/Aug. 1992, pp. 1389-1401.
59. Parker, D. H., Chatterjee, K., Wurz, P., Lykke, K. R., Pellin, M. J., Stock, L. M., and J. C. Hemminger, "Fullerenes and giant fullerenes: Synthesis, separation, and mass spectrometric characterization," appears in The Fullerenes, ed. by H. W. Kroto, J. E. Fischer, and D. E. Cox, Pergamon Press, Oxford, 1993, pp. 29-44.
60. Gagné, R. R. J., and A. Cantin, "Investigation of an rf plasma with symmetrical and asymmetrical electrostatic probes," J. Appl. Phys., v. 43 (6), June 1972, pp. 2639-2647.

61. Godyak, V. A., Piejak, R. B., and B. M. Alexandrovich, "Measurements of electron energy distribution in low-pressure RF discharges," Plasma Sources Sci. Technol., v. 1, 1992, pp. 36-58.
62. Laframboise, J. G., "Theory of spherical and cylindrical Langmuir probes in a collisionless, Maxwellian plasma at rest," University of Toronto, Institute for Aerospace Studies, UTIAS Report No. 100, June 1966.
63. Wainman, P. N., Lieberman, M. A., Lichtenberg, A. J., Stewart, R. A., and C. Lee, "Characterization at different aspect ratios (radius/length) of a radio frequency inductively coupled plasma source," J. Vac. Sci. Technol. A, v. 13 (5), Sep./Oct. 1995, pp. 2464-2469.
64. Beattie, J. R., "Numerical procedure for analyzing Langmuir probe data," AIAA Journal, v. 13 (7), July 1975, pp. 950-952.
65. Brophy, J. R., "Modified Bohm velocity for plasma containing primary electrons and doubly charged ions," appears in NASA CR-165253, "Ion & Advanced Electric Thruster Research," ed. by P. J. Wilbur, Dec. 1980, pp. 107-112.
66. Braithwaite, N. St. J., and J. E. Allen, "Boundaries and probes in electronegative plasmas," J. Phys. D: Appl. Phys., v. 21, 1988, pp. 1733-1737.
67. Jaeger, E. F., Berry, L. A., and D. B. Batchelor, "Characteristics of a cylindrical Langmuir probe of finite length," J. Appl. Phys., v. 69 (10), 15 May 1991, pp. 6918-6922.
68. Clements, R. M., "Plasma diagnostics with electric probes," J. Vac. Sci. Technol., v. 15 (2), Mar./Apr. 1978, pp. 193-199.
69. Godyak, V. A., Piejak, R. B., and B. M. Alexandrovich, "Probe diagnostics of non-Maxwellian plasmas," J. Appl. Phys., v. 73 (8), 15 Apr. 1993, pp. 3657-3663.

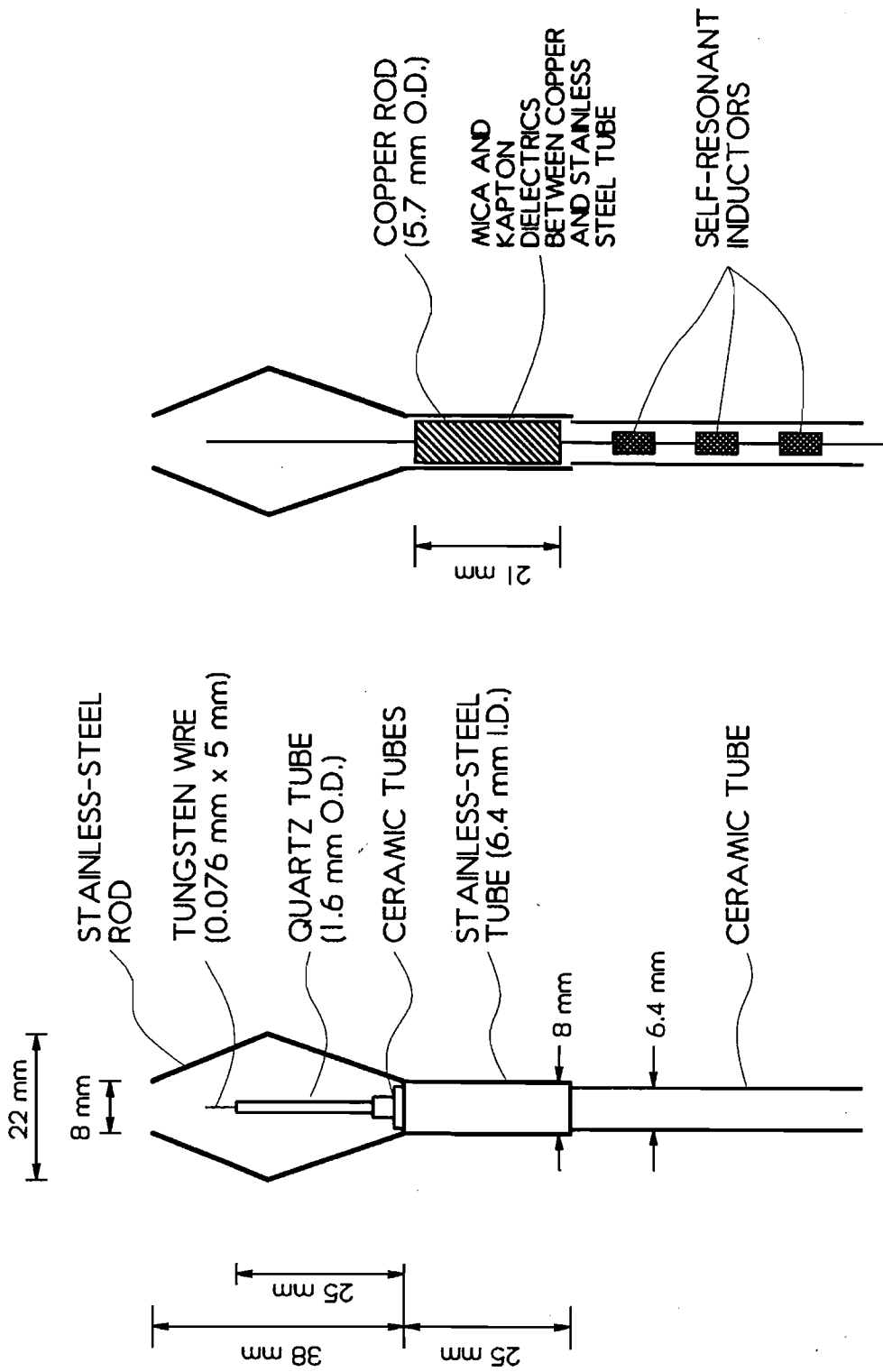
## APPENDIX A

### LANGMUIR PROBE METHODS

#### A. RF Probe Design

The substantial RF plasma fluctuations that develop in inductive plasmas can lead to inaccurate Langmuir probe measurements. Specifically, plasma potential fluctuations over the RF period will cause the DC bias between the probe tip and the plasma to fluctuate about the mean probe bias, and analysis of the probe traces with conventional theories will yield erroneous results. The solution to this problem is to make the probe tip “follow” the plasma potential fluctuations so the DC bias between the probe and the plasma is constant [60,61]. This is accomplished by creating a very large impedance at the RF frequencies between the probe tip and the measuring circuit, so the probe tip will be forced to follow the RF fluctuations. With these precautions, the probe I-V data may be acquired and analyzed accurately with conventional methods.

A schematic of the Langmuir probe that was constructed for RF plasma measurements is shown in Fig. A1. Three self-resonant inductors are housed inside the ceramic tube at the base of the probe. One of the inductors is resonant (i.e. has a large impedance) at the fundamental frequency (13.56 MHz) and the other two are resonant at the first and second harmonics, respectively (27 and 41 MHz). The inductors are electrically connected to copper rod housed inside the stainless-steel tube. The copper is



a) External View.

b) Cross-Sectional View.

Fig. A1 Schematic of Langmuir Probe for Measurements in RF Plasmas.

wrapped in dielectrics so that it and the stainless-steel tube are electrically isolated from each other and form a cylindrical body capacitor. The tungsten wire probe tip is then attached at the other end of the copper rod.

Electrically, the inductors provide the necessary RF impedance between the probe tip and the measuring circuit. Equally important is the body capacitor, which was designed to have a capacitance near 60 pF. The capacitance between the plasma and probe tip, based on expected plasma conditions in an inductive argon discharge, is estimated to be near 0.2 pF. Thus, the body capacitance between the probe tip and the plasma will dominate the probe-plasma capacitance and substantially reduce the probe-plasma impedance and enable the probe to follow plasma fluctuations more closely. The large body capacitance also has the added effect of keeping the probe-plasma capacitance essentially constant and this reduces errors associated with the changing sheath capacitance as the probe bias voltage is varied. The arms attached to the stainless-steel tube are required to keep the body capacitor in contact with the plasma as the probe tip is drawn to the downstream end of the discharge chamber where the tube is no longer immersed in the plasma. Conservative estimates of the plasma potential fluctuations and the total probe circuit impedance indicate that the probe design meets the criteria of Godyak *et al.* [61] for accurate measurements in RF plasmas.

The probe measuring circuit is essentially a conventional probe circuit. The reference electrode is the stainless-steel plate which is located at downstream end of the discharge chamber. In addition, low-pass RF filtering circuits are used on the atmospheric side of the vacuum feed-throughs for electrical connections to both the probe and the plate. The RF probe design and the low-pass filters reduced RF fluctuations at the

measuring equipment to less than 5 mV, whereas potential fluctuations in the plasma are expected to be tens of volts.

### B. Analysis of Probe Data Acquired in RF Discharges

The conventional analysis method for a plasma containing only Maxwellian electrons and positive ions involves: 1) the subtraction of ion current from the probe trace, 2) preparation of a semi-log plot of I-V data from which the electron temperature and plasma potential are inferred, and 3) calculation of the electron density from the probe current collected at plasma potential. The positive ion density is then known by assuming quasi-neutrality in the bulk plasma (i.e.  $n_{+o} = n_{eo}$ ). In a plasma also containing negative ions, the analysis is complicated by an additional species of negatively-charged particle carrying current to the probe, and by the fact that the positive ion density and electron density are not equal. In order to calculate the value of an additional variable ( $n_{-o}$ ), an additional piece of information must be obtained from the probe trace. This is often achieved by calculating the positive ion density from the positive ion saturation portion of the probe trace.

In the limit where the plasma Debye length is much greater than the radius of a cylindrical probe (i.e. the thick sheath case), the current to the probe is described by Langmuir's orbital-motion-limited (OML) theory. Laframboise [62] has numerically verified the accuracy of the simple form of the OML for probe radii less than the Debye length, which is the case for the C<sub>60</sub> plasmas. For positive ions, the OML current to the probe at large potentials compared to the ion temperature is given by [62]:

$$I_{OML} = eA_p n_{+o} \sqrt{\frac{-2e(\phi_{probe} - \phi_{plasma})}{\pi^2 m_+}} \quad (A1)$$

(it was assumed for all the Langmuir probe analyses that all heavy particles were C<sub>60</sub> and none were fragments for simplicity). If the probe data are plotted as I<sup>2</sup> vs. V, the OML regime appears as a linear portion of the curve and the positive ion density can be calculated from the slope of a linear curve fit at negative probe potentials. This regime, however, must be at potentials that are large compared to the electron temperature to assure that the current to the probe is only ions, but not so large that the probe sheath becomes more spherical than cylindrical and the OML relationship changes.

The OML ion current can be subtracted from the total probe current using the method of Wainman *et al.* [63] and then a traditional semi-log plot can be prepared to determine the electron temperature. Since it is assumed that the negative ions are at the wall temperature ( $T_w = 800 \text{ K} = 0.07 \text{ eV}$ ), at a probe potential of one volt less than plasma potential, essentially all negative ions will be repelled from the probe and the electrons will dominate the probe current. Thus, the electron temperature is obtained from the I-V data at probe potentials just less than plasma potential.

The electron density is determined from the current to the probe at plasma potential ( $I_p$ ), where no sheath exists around the probe and all charged particles arrive at the probe surface with their thermal velocities. If quasi-neutrality is invoked ( $n_{+o} = n_{eo} + n_{-o}$ ) and it is assumed that all heavy particles are in thermal equilibrium with each other and the chamber walls, the electron density can be calculated using:

$$\frac{I_p \sqrt{2\pi}}{eA_p} = n_{eo} \left( \sqrt{\frac{k_B T_e}{m_e}} - \sqrt{\frac{k_B T_w}{m_+}} \right). \quad (\text{A2})$$

The negative ion density is then calculated using quasi-neutrality.

### C. Analysis of Probe Data Acquired in DC Discharges

The electron energy distribution function in a DC discharge is frequently and accurately modeled as consisting of a low-temperature Maxwellian group and a high-energy primary electron group. If the plasma sheath adjacent to the probe is approximately planar, the primary-electron contribution to the probe current appears on a probe trace as a linear I-V relationship, while the Maxwellian-electron contribution is the typical exponential I-V relationship [37]. The planar sheath condition is satisfied with a spherical probe if the plasma Debye length is much smaller than the probe radius (i.e. the thin-sheath case). The probe data can be fitted with a curve that is the sum of a linear and an exponential component and the resulting curve fit will yield the primary electron energy and density, and the Maxwellian electron temperature and density [64]. Even though the negative ion density in the C<sub>60</sub> plasmas that were investigated were appreciable, the curve fits yielded accurate results because the negative ion currents to the probe were negligible compared to the electron currents.

In order to determine the positive and negative ion densities in a C<sub>60</sub> plasma, the positive ion saturation portion of the probe trace must again be used. In the thin sheath case, this requires a knowledge of the positive ion velocity at the sheath edge (i.e. the Bohm velocity) and knowledge of the electrical potential distribution near the probe. The Bohm velocity is also used to predict the beam current that can be extracted from the C<sub>60</sub> plasmas in the DC thruster. The necessary expressions are derived in following sections.

#### 1. Bohm Velocity in a Plasma Containing Negative Ions and Primary Electrons

The one-dimensional Poisson equation applied to the sheath region is given by:

$$\frac{d^2 \phi}{dx^2} = -\frac{e}{\epsilon_0} [n_+(x) - n_-(x) - n_e(x) - n_p(x)] \quad (\text{A3})$$

where all variables are defined in Appendix B. The potential ( $\phi$ ) and position ( $x$ ) are defined to be zero at the sheath edge (i.e. the plasma/sheath boundary).

The Maxwellian-electron and negative-ion densities in the sheath are given by the barometric equation:

$$\begin{aligned} n_e(x) &= n_{es} \exp(e\phi/k_B T_e) \\ n_-(x) &= n_{-s} \exp(e\phi/k_B T_-) \end{aligned} \quad (\text{A4})$$

and are referenced to the densities at the sheath edge ( $x=0$ ).

The continuity and energy equations are used to determine the densities of primary electrons and positive ions in the sheath. Continuity of primary electrons is given by:

$$n_p(x)v_p(x) = n_{ps}v_{ps} \left(1 + \frac{e\phi}{\epsilon_p}\right) \quad (\text{A5})$$

where the multiplier on the right-hand side of the equation accounts for reflection of electrons in the sheath. The corresponding expression for conservation of energy is:

$$\frac{1}{2}m_e v_p^2(x) - e\phi(x) = \frac{1}{2}m_e v_{ps}^2 = \epsilon_p. \quad (\text{A6})$$

Combining Eqs. A5 and A6 yields the expression for the primary electron density in the sheath:

$$n_p(x) = n_{ps} \left[1 + \frac{e\phi}{\epsilon_p}\right]^{\frac{1}{2}}. \quad (\text{A7})$$

The continuity and energy equations through the sheath for positive ions are:

$$\begin{aligned}
n_+(x)v_+(x) &= n_{+s}v_{+s} \\
\frac{1}{2}m_+v_+^2(x) + e\phi(x) &= \frac{1}{2}m_+v_{+s}^2 = \varepsilon_+.
\end{aligned} \tag{A8}$$

Combining the two equations yields:

$$n_+(x) = n_{+s} \left[ \frac{\varepsilon_+}{\varepsilon_+ - e\phi} \right]^{1/2}. \tag{A9}$$

Now, substituting Eqs. A4, A7, and A9 into Eq. A3, multiplying both sides of the equation by  $d\phi/dx$ , and integrating using the boundary condition  $d\phi/dx \approx 0$  at  $\phi=0$ , yields:

$$\begin{aligned}
\left( \frac{d\phi}{dx} \right)^2 &= \frac{4}{\varepsilon_o} \left\{ n_{+s} \varepsilon_+ \left( \sqrt{1 - \frac{e\phi}{\varepsilon_+}} - 1 \right) + \frac{k_B T_-}{2} n_{-s} \left[ \exp(e\phi/k_B T_-) - 1 \right] \right. \\
&\quad \left. + \frac{k_B T_e}{2} n_{es} \left[ \exp(e\phi/k_B T_e) - 1 \right] + \frac{\varepsilon_p}{3} n_{ps} \left[ \left( 1 + \frac{e\phi}{\varepsilon_p} \right)^{3/2} - 1 \right] \right\}.
\end{aligned} \tag{A10}$$

In order for this equation to be meaningful, the term inside the braces on the right hand side must be non-negative, hence

$$\begin{aligned}
&n_{+s} \varepsilon_+ \left( \sqrt{1 - \frac{e\phi}{\varepsilon_+}} - 1 \right) + \frac{k_B T_-}{2} n_{-s} \left[ \exp(e\phi/k_B T_-) - 1 \right] \\
&\quad + \frac{k_B T_e}{2} n_{es} \left[ \exp(e\phi/k_B T_e) - 1 \right] + \frac{\varepsilon_p}{3} n_{ps} \left[ \left( 1 + \frac{e\phi}{\varepsilon_p} \right)^{3/2} - 1 \right] \geq 0.
\end{aligned} \tag{A11}$$

The following power series expansions are used to simplify this expression:

$$\begin{aligned}
\exp(e\phi/k_B T) &= 1 + \frac{e\phi}{k_B T} + \frac{1}{2} \left( \frac{e\phi}{k_B T} \right)^2 + \dots \\
\left( 1 - \frac{e\phi}{\varepsilon_+} \right)^{1/2} &= 1 - \frac{1}{2} \frac{e\phi}{\varepsilon_+} - \frac{1}{8} \left( \frac{e\phi}{\varepsilon_+} \right)^2 + \dots \\
\left( 1 + \frac{e\phi}{\varepsilon_p} \right)^{3/2} &= 1 + \frac{3}{2} \frac{e\phi}{\varepsilon_p} + \frac{3}{8} \left( \frac{e\phi}{\varepsilon_p} \right)^2 + \dots.
\end{aligned} \tag{A12}$$

Near the sheath edge,

$$\frac{e\phi}{k_B T} \ll 1, \quad \frac{e\phi}{\varepsilon_+} \ll 1, \quad \frac{e\phi}{\varepsilon_p} \ll 1, \quad (\text{A13})$$

so higher-order terms can be discarded and Eq. A11 reduces to:

$$\begin{aligned} -n_{+s} \left[ \frac{e\phi}{2} + \frac{(e\phi)^2}{8\varepsilon_+} \right] + \frac{n_{-s}}{2} \left[ e\phi + \frac{(e\phi)^2}{2k_B T_-} \right] \\ + \frac{n_{es}}{2} \left[ e\phi + \frac{(e\phi)^2}{2k_B T_e} \right] + n_{ps} \left[ \frac{e\phi}{2} + \frac{(e\phi)^2}{8\varepsilon_p} \right] \geq 0. \end{aligned} \quad (\text{A14})$$

Rearranging Eq. A14 and recognizing that quasi-neutrality holds at the sheath edge

( $n_{+s} = n_{-s} + n_{es} + n_{ps}$ ) one obtains

$$\frac{1}{8}(e\phi)^2 \left[ \frac{-n_{+s}}{\varepsilon_+} + \frac{2n_{-s}}{k_B T_-} + \frac{2n_{es}}{k_B T_e} + \frac{n_{ps}}{\varepsilon_p} \right] \geq 0 \quad (\text{A15})$$

which simplifies to

$$\frac{2n_{es}}{k_B T_e} + \frac{2n_{-s}}{k_B T_-} + \frac{n_{ps}}{\varepsilon_p} \geq \frac{n_{+s}}{\varepsilon_+}. \quad (\text{A16})$$

Solving Eq. A16 for the positive ion kinetic energy gives:

$$\varepsilon_+ = \frac{1}{2} m_+ v_{+s}^2 \geq \frac{n_{+s}}{\frac{2n_{es}}{k_B T_e} + \frac{2n_{-s}}{k_B T_-} + \frac{n_{ps}}{\varepsilon_p}}. \quad (\text{A17})$$

Solving for  $v_{+s}$  and rearranging yields:

$$v_{+s} \geq \sqrt{\frac{k_B T_e}{m_+} \frac{n_{+s}}{n_{es} + \frac{T_e}{T_-} n_{-s} + \frac{k_B T_e}{2\varepsilon_p} n_{ps}}}. \quad (\text{A18})$$

Equation A18 is the expression for the modified Bohm velocity in a plasma containing negative ions and primary electrons. Eliminating  $n_{+s}$  using the quasi-neutrality expression and using the non-dimensional parameters defined below,

$$\alpha_s \equiv \frac{n_{-s}}{n_{es}} \quad \beta_s \equiv \frac{n_{ps}}{n_{es}} \quad (A19)$$

$$\gamma \equiv \frac{T_e}{T_-} \quad \gamma_p \equiv \frac{k_B T_e}{\epsilon_p},$$

the final expression for the Bohm velocity becomes:

$$v_{+s} \geq \sqrt{\frac{k_B T_e}{m_+} \frac{1 + \alpha_s + \beta_s}{1 + \gamma \alpha_s + \frac{1}{2} \gamma_p \beta_s}} \quad (A20)$$

Equation A20 reduces to the conventional Bohm velocity for a plasma containing only positive ions and Maxwellian electrons ( $\alpha_s = \beta_s = 0$ ). It also reduces to the expression derived by Boyd and Thompson [36] for a plasma with no primary electrons ( $\beta_s = 0$ ) and to that derived by Brophy [65] for a plasma with no negative ions ( $\alpha_s = 0$ ).

Typical ion thruster DC discharges have primary electron concentrations of a few percent (i.e.  $\beta_s$  of order  $10^{-2}$ ). Since plasmas established with strongly electronegative gases such as  $C_{60}$  often have large negative ion concentrations ( $\alpha_s > 10$ ), it can be seen that the Bohm velocity will be dominated by the effect of the negative ions and that the effect of the primary electrons will be negligible.

## 2. Relationship Between Particle Densities in Bulk Plasma and at Sheath Edge

In reality, the ion density at the sheath edge is different than in the bulk plasma as a result of the potential variation in the presheath (i.e. the region of space between the bulk plasma and the sheath edge). Boyd and Thompson [36] derived an expression for the

variation in particle density through the presheath in a plasma containing negative ions, and their development will be extended here for a plasma containing both negative ions and primary electrons.

The plasma potential (i.e. the potential that exists in the bulk of the plasma) is taken to be the zero point for potential variations. The potential at the sheath edge is then  $\phi_s$ , which is non-dimensionalized with respect to the temperature of the Maxwellian electrons,

$$\eta_s \equiv \frac{-e\phi_s}{k_B T_e}. \quad (\text{A21})$$

If it is assumed that the positive ions have zero kinetic energy in the bulk of the plasma, then the kinetic energy that they possess at the sheath edge will be equivalent to the energy gained by falling through the potential change in the presheath:

$$\frac{1}{2} m_+ v_{+s}^2 = -e\phi_s. \quad (\text{A22})$$

Substituting Eqs. A20 and A21 into Eq. A22 and solving for  $\eta_s$  yields:

$$\eta_s = \frac{1}{2} \left( \frac{1 + \alpha_s + \beta_s}{1 + \gamma \alpha_s + \frac{1}{2} \gamma_p \beta_s} \right). \quad (\text{A23})$$

The relationship between  $\alpha$  in the bulk plasma and at the sheath edge may be determined from the sheath potential and the barometric equation:

$$\alpha_s = \frac{n_{-s}}{n_{es}} = \frac{n_{-o} \exp(e\phi_s / k_B T_-)}{n_{eo} \exp(e\phi_s / k_B T_e)} = \alpha_o \exp[-\eta_s(\gamma - 1)]. \quad (\text{A24})$$

Similarly for  $\beta$ ,

$$\beta_s = \frac{n_{ps}}{n_{es}} = \frac{n_{po} \sqrt{1 + e\phi_s / \epsilon_p}}{n_{eo} \exp(e\phi_s / k_B T_e)} = \beta_o \exp(\eta_s) \sqrt{1 - \gamma_p \eta_s}. \quad (\text{A25})$$

Using quasi-neutrality, the positive ion density may then be determined at the sheath edge:

$$\begin{aligned} n_{+s} &= n_{es} + n_{-s} + n_{ps} \\ &= n_{eo} \left[ \frac{n_{es}}{n_{eo}} + \frac{n_{-o}}{n_{eo}} \frac{n_{-s}}{n_{-o}} + \frac{n_{po}}{n_{eo}} \frac{n_{ps}}{n_{po}} \right] \\ &= n_{eo} \left[ \exp(-\eta_s) + \alpha_o \exp(-\gamma \eta_s) + \beta_o \sqrt{1 - \gamma_p \eta_s} \right]. \end{aligned} \quad (\text{A26})$$

### 3. Calculation of Ion Densities from Probe Data

Following the method of Braithwaite and Allen [66], the current to the probe at plasma potential and the positive ion saturation current are determined from the probe data. The positive ion saturation current is given by:

$$I_+ = eA_s n_{+s} v_{+s}. \quad (\text{A27})$$

Substituting Eqs. A20, A23, and A26 into Eq. A27:

$$I_+ = eA_s n_{eo} \left[ \exp(-\eta_s) + \alpha_o \exp(-\gamma \eta_s) + \beta_o \sqrt{1 - \gamma_p \eta_s} \right] \sqrt{\frac{2\eta_s k_B T_e}{m_+}}. \quad (\text{A28})$$

The net current to the probe at plasma potential is given by:

$$I_p = eA_s \left[ n_{eo} \sqrt{\frac{k_B T_e}{2\pi m_e}} + n_{-o} \sqrt{\frac{k_B T_-}{2\pi m_+}} - n_{+o} \sqrt{\frac{k_B T_+}{2\pi m_+}} + \frac{n_{po}}{4} \sqrt{\frac{2e\epsilon_p}{m_e}} \right]. \quad (\text{A29})$$

Assuming that the positive and negative ion temperatures are equal, Eq. A29 can be rewritten:

$$I_p = eA_s n_{eo} \left[ \sqrt{\frac{k_B T_e}{2\pi m_e}} - (1 + \beta_o) \sqrt{\frac{k_B T_-}{2\pi m_+}} + \frac{\beta_o}{4} \sqrt{\frac{2e\epsilon_p}{m_e}} \right]. \quad (\text{A30})$$

The ratio of the two currents ( $I_p/I_+$ ) is then taken and the resulting expression is rearranged:

$$\frac{1}{2} \frac{I_+}{I_p} \left\{ \sqrt{\frac{m_+}{\pi m_e}} + \frac{\beta_o}{2} \sqrt{\frac{1}{\gamma_p} \frac{m_+}{m_e}} - (1 + \beta_o) \sqrt{\frac{1}{\pi \gamma}} \right\} = \sqrt{\eta_s} \left[ \exp(-\eta_s) + \alpha_o \exp(-\gamma \eta_s) + \beta_o \sqrt{1 - \gamma_p \eta_s} \right]. \quad (\text{A31})$$

The initial analysis of the Langmuir probe trace may be done without knowledge of the ion densities, as discussed earlier, and will yield all of the electron parameters. The left-hand side of Eq. A31 then is known, and the right-hand side is a function of  $\eta_s$  and  $\alpha_o$ . Finally, Eqs. A23, A24, and A25 are solved simultaneously with Eq. A31 to yield the non-dimensional parameters  $\alpha_o$ ,  $\alpha_s$ ,  $\beta_s$ , and  $\eta_s$ . The positive and negative ion densities in the bulk plasma and at the sheath edge may then be calculated.

#### D. Accuracy of Probe Measurements

A Langmuir probe used for plasma measurements must have certain physical dimensions compared to characteristic plasma dimensions to ensure accurate results [61]. For example, the probe tip and probe holder near the tip must have dimensions smaller than the electron mean free path so that the local plasma electron density is not depleted by probe collection and so that the sheath surrounding the probe is essentially collisionless. The electron mean free path was greater than 100 mm in all the plasmas considered in this study, which is much larger than the probe dimensions. As mentioned previously, the probe tip must also have a certain size compared to the plasma Debye length depending on the analysis method. The Debye length for the DC plasmas was 4-7% of the probe radius which is considered acceptable for the thin-sheath requirement. For the C<sub>60</sub> RF plasmas

the Debye length was several times larger than the probe radius which is a necessary condition for the OML theory of positive ion collection. Additionally, the mean free path for positive ions was at least 8 mm in the C<sub>60</sub> RF plasma which assured collisionless OML ion collection. The length-to-diameter ratio of the cylindrical probes was also sufficient to provide a one-dimensional cylindrical sheath that avoided end effects [67].

Probe measurements can be affected by contamination which either changes the work function of the probe surface or creates a resistive layer on the surface of the probe. Both of these contamination effects can lead to inaccurate estimates of plasma parameters, and thus probes are often “cleaned” by holding the probe potential at either a very large negative or positive value, drawing relatively large currents to the probe [68]. Since C<sub>60</sub> will condense on cool surfaces it was necessary to take precautions to avoid probe contamination. The probes were not inserted to C<sub>60</sub> discharges until measurements were to be taken, and then they were held at potentials tens of volts above the plasma potential to draw large electron currents between measurements. The large electron currents heated the probe surface to drive off any carbon deposits. The probe data were found to be very reproducible over the ~ten minutes of an experiment, indicating that the cleaning method prevented a steady buildup of residue on the probe surface during an experiment.

In addition to probe contamination and changes in work function, the data analysis method and general uncertainties in plasma property measurements can lead to errors in the probe results. The errors in plasma potential and electron population parameters, shown in Table A1, are estimated from the analysis of hundreds of probe traces and through other work [4]. Also shown in the table are estimates of errors in calculation of the positive ion density. Part of the estimated error for the OML method (RF C<sub>60</sub>

plasmas) comes from the curve-fitting procedure. Further discussion of errors in the OML method may be found in Refs. 61 and 69. The error in the ion-saturation-current method (DC plasmas) was estimated from comparisons between ion and electron density in argon plasmas. Godyak *et al.* [69] discuss various methods of measuring plasma properties in non-Maxwellian plasmas and the errors associated with them.

Table A1. Uncertainties in Plasma Parameters.

$\phi_{plasma}$	$\pm 1$ V
$n_e$	$\pm 20\%$
$T_e$	$\pm 15\%$
$n_p$	$\pm 20\%$
$\varepsilon_p$	$\pm 20\%$
$n_+$ (OML)	$\pm 20\%$
$n_+$ (Ion sat. curr.)	$\pm 30\%$

## APPENDIX B

### NOMENCLATURE

$A_{fil}$	Surface area of tantalum filament ( $m^2$ )
$A_g$	Open area of screen grid ( $m^2$ )
$A_p$	Surface area of cylindrical Langmuir probe ( $m^2$ )
$A_s$	Area of sheath surrounding spherical Langmuir probe ( $m^2$ )
$A_w$	Surface area of discharge chamber walls ( $m^2$ )
$B_f$	Arrhenius pre-exponential factor for reactions: $C_{60}^+ \rightarrow C_{58}^+ + C_2$ and $C_{58}^+ \rightarrow C_{56}^+ + C_2$ ( $sec^{-1}$ )
$D(\epsilon_p, \epsilon_{ex})$	Energy deposition function for ionizing electrons ( $eV^{-1}$ )
$e$	Electronic charge ( $1.6 \times 10^{-19}$ coul.)
$E_f$	Arrhenius activation energy for reaction $C_{60}^+ \rightarrow C_{58}^+ + C_2$ (eV)
$I_+$	Positive ion saturation current collected by Langmuir probe (A)
$I_{OML}$	Orbital-motion-limited positive ion current collected by Langmuir probe (A)
$I_p$	Net current collected by Langmuir probe at plasma potential (A)
$J_B$	Beam current (A)
$k_B$	Boltzmann's constant ( $1.38 \times 10^{-23}$ J/K)
$k_{colls}$	Reaction rate for positive ion collisions with neutral molecules ( $sec^{-1}$ )
$k_{frag}$	Reaction rate for positive ion fragmentation ( $sec^{-1}$ )
$k_{rad}$	Reaction rate for positive ion radiation ( $sec^{-1}$ )
$k_{rec}$	Reaction rate for recombination of positive and negative ions ( $sec^{-1}$ )
$m_+$	Ion mass (kg)
$m_e$	Electron mass (kg)
$n_{+s}$	Positive ion density at sheath edge ( $m^{-3}$ )
$n_{+o}$	Positive ion density in bulk plasma ( $m^{-3}$ )
$n_{-s}$	Negative ion density at sheath edge ( $m^{-3}$ )
$n_{-o}$	Negative ion density in bulk plasma ( $m^{-3}$ )
$n_{es}$	Maxwellian electron density at sheath edge ( $m^{-3}$ )
$n_{eo}$	Maxwellian electron density in bulk plasma ( $m^{-3}$ )
$n_{ps}$	Primary electron density at sheath edge ( $m^{-3}$ )
$n_{po}$	Primary electron density in bulk plasma ( $m^{-3}$ )
$n_n$	Neutral molecule density ( $m^{-3}$ )
$T_+$	Positive ion temperature (K)
$T_-$	Negative ion temperature (K)
$T_e$	Maxwellian electron temperature (K or eV)
$T_v$	Molecular vibrational temperature (K)

$T_w$	Discharge chamber wall temperature (K)
$v_+$	Positive ion velocity (m/s)
$v_{+s}$	Positive ion velocity at sheath edge (m/s)
$v_n$	Neutral molecule mean thermal velocity (m/s)
$v_p$	Primary electron velocity (m/s)
$v_{ps}$	Primary electron velocity at sheath edge (m/s)
$V$	Volume of discharge chamber (m <sup>3</sup> )
$x$	Position variable (m)
$\frac{dn_+}{d\varepsilon_v}$	Distribution function for vibrationally-excited positive ions (m <sup>-3</sup> eV <sup>-1</sup> )

### Greek Letters

$\alpha_s$	Negative ion concentration at sheath edge (defined by Eq. A19)
$\alpha_o$	Negative ion concentration in bulk plasma
$\beta_s$	Primary electron concentration at sheath edge (Eq. A19)
$\beta_o$	Primary electron concentration in bulk plasma
$\gamma$	Ratio of electron to negative-ion temperature (Eq. A19)
$\gamma_p$	Ratio of Maxwellian-electron temperature to primary-electron energy (Eq. A19)
$\varepsilon_+$	Ion kinetic energy (J)
$\varepsilon_B$	Energy cost of a beam ion (eV/ion)
$\varepsilon_{ex}$	Excitation energy added to molecule by ionizing electron (eV)
$\varepsilon_{IP}$	Ionization potential of C <sub>60</sub> (eV)
$\varepsilon_p$	Primary electron energy (eV or J)
$\varepsilon_{th}$	Molecular thermal energy stored in vibration (eV)
$\varepsilon_v$	Molecular vibrational energy (eV)
$\varepsilon_o$	Permittivity of free space (8.854×10 <sup>-12</sup> F/m)
$\eta_s$	Non-dimensionalized sheath potential (defined by Eq. A21)
$\sigma_+$	Cross section for positive ionization of C <sub>60</sub> (m <sup>2</sup> )
$\phi$	Electrical potential (V)
$\phi_s$	Electrical potential at sheath edge (V)